A MONTE CARLO APPROACH TO ^{7}BE SOLAR NEUTRINO ANALYSIS WITH KAMLAND

by

CHRISTOPHER PETER GRANT

ANDREAS PIEPKE, COMMITTEE CHAIR

JEROME BUSENITZ
ION STANCU
NOBUCHIKA OKADA
MARTIN BAKKER

A DISSERTATION

Submitted in partial fullfillment of the requirements
for the degree of Doctor of Philosophy
in the Department of Physics
in the Graduate School of
The University of Alabama

TUSCALOOSA, ALABAMA

2012

Abstract

Terrestrial measurements of neutrinos produced by the Sun have been of great interest for over half a century because of their ability to test the accuracy of solar models. The first solar neutrinos detected with KamLAND provided a measurement of the ^{8}B solar neutrino interaction rate above an analysis threshold of 5.5 MeV. This work describes efforts to extend KamLAND's detection sensitivity to solar neutrinos below 1 MeV, more specifically, those produced with an energy of 0.862 MeV from the ^{7}Be electron-capture decay.

Many of the difficulties in measuring solar neutrinos below 1 MeV arise from backgrounds caused abundantly by both naturally occuring, and man-made, radioactive nuclides. The primary nuclides of concern were ^{210}Bi, ^{85}Kr, and ^{39}Ar. Since May of 2007, the KamLAND experiment has undergone two separate purification campaigns. During both campaigns a total of 5.4 ktons (about 6440 m^3) of scintillator was circulated through a purification system, which utilized fractional distillation and nitrogen purging. After the purification campaign, reduction factors of 1.5×10^3 for ^{210}Bi and 6.5×10^4 for ^{85}Kr were observed.

The reduction of the backgrounds provided a unique opportunity to observe the ^{7}Be solar neutrino rate in KamLAND. An observation required detailed knowledge of the detector response at low energies, and to accomplish this, a full detector Monte Carlo simulation, called KLG4sim, was utilized. The optical model of the simulation was tuned to match the detector response observed in data after purification, and the

software was optimized for the simulation of internal backgrounds used in the ^{7}Be solar neutrino analysis. The results of this tuning and estimates from simulations of the internal backgrounds and external backgrounds caused by radioactivity on the detector components are presented.

The first KamLAND analysis based on Monte Carlo simulations in the energy region below 2 MeV is shown here. The comparison of the $\Delta\chi^2$ between the null hypothesis and the existence of the ^{7}Be solar neutrino signal in the data shows a change of 27.9 units, providing evidence that the signal is statistically favored. This analysis reports a measured interaction rate from ^{7}Be solar neutrinos of $R = 343.3 \pm 65.0(\text{stat}) \pm 99.2(\text{syst})$ events/(kton·day), which corresponds to a total flux of $\Phi = (3.41 \pm 1.18) \times 10^{9}$ cm^{-2}s^{-1}. The ^{7}Be solar neutrino flux reported in this work is only the second measurement made of this quantity worldwide. It provides an important cross-check of the Borexino experiment. The flux measurement reported here agrees within 1σ with the standard solar model predictions thus validating our basic understanding of solar fusion reaction processes.

Acknowledgments

First and foremost, I would like to thank my family for all of their love and support over the years. My father, Charles Grant, and my mother, Dorothy Grant, have always been there for me no matter the circumstances. They continue to motivate me to do my best and stay the course whenever a challenge presents itself. Kevin Grant, has been the best brother a guy like me could ask for. I've enjoyed the memorable experiences growing up together and am inspired by his new role as a husband and family man.

I'm forever in debt to my advisor, Prof. Andreas Piepke. With an enormous amount of patience and dedication, he was able to mould a physicist out of a lost and confused graduate student. He has always provided a clear focal point for my learning, all the while reminding me of the incredible joy of working relentlessly to achieve scientific discovery. I imagine that it will be difficult to leave out a "thus" in any publications or proposals I write in the future.

I would also like to thank Prof. Kunio Inoue for inviting me to work with RCNS throughout the purification campaigns and post-purification analysis. I am grateful for all of his encouragement, advice and friendship. Doing physics in Kamioka wouldn't have been possible without the help of all my collaborators at RCNS and I owe many thanks to Prof. Masayuki Koga and Dr. Kengo Nakamura for their continued onsite support. I want to thank Prof. Yasuhiro Kishimoto, Prof. Sei Yoshida, Prof. Tadao Mitsui, Dr. Yoshihito Gando and Dr. Haruo Ikeda for all of their work

on the purification system and for allowing me to work with them on such a difficult task.

I owe a great deal of gratitude to Dr. Itaru Shimizu for all of his advice concerning my data analysis, and to Dr. Kyohei Nakajima for revealing the inner workings of the RCNS data analysis software. Thanks also goes to Prof. Stuart Freedman, Prof. Patrick Decowski, Dr. Jason Detwiler, Dr. Tom Banks, Dr. Ke Han and Prof. Yuri Efremenkov for their helpful discussions involving the data analysis. I would also like to show appreciation to Prof. Glenn Horton-Smith and Dr. Lauren Hsu for their attempts to guide me through the constructs of KLG4sim. Special thanks goes out to Dr. Brian Fujikawa (a.k.a. Sweetie!!!), Dr. Tommy O'Donnell, Dr. Chao Zhang, Dr. Sanshiro Enomoto, Prof. Junpei Shirai and Prof. Bruce Berger for making life in Osawano and Mozumi tolerable. I will have many fond memories of all the fun times we had with little or nothing to do except for rock-climbing, singing and drinking.

My tenure as a graduate student wouldn't be complete without mention of my UA colleagues and friends, Dr. Gregory Keefer (a.k.a. Greggy), Dr. Timothy Classen (a.k.a. Duuuuude), Dr. Denis Perevalov and Dr. Igor Ostrovskiy. I wouldn't have discovered my love for neutrinos without Greg, and he was the perfect role model as a graduate student as he helped pave the way for a ^{7}Be solar neutrino measurement with KamLAND. Tim was a great drinking buddy and was always giving me useful advice on KamLAND and life in general - his pessimistic response is one-of-a-kind but most humorous. Denis' overall enthusiasm for life, desire to hug everyone after a few too many drinks, and love for Alabama football will always bring a smile to my face. Igor's passion for competition and challenging discussions were always entertaining, and he's the only person I know who uses sushi as a form of monetary exchange.

Last, but not least, I would also like to thank my long-time friends. Shane Sprague and Abbey Wolfe have been more like family than anything else, and they have always

expressed their love and support ever since I've met them. Tom Kilps has been a best friend since middle school, and I always enjoy our adventures together, even as we grow older. I would also like to give a shout-out to all my Brothers of Delta Sigma Phi - Epsilon Iota. I've always received so much encouragement from all of you and I'm thankful for the bond we all share - YITBOS.

List of Abbreviations

A	Ampere
atm	atmosphere unit of pressure
ATLES	Attenuation Length Emission Spectrometer
ATWD	Analog Transient Waveform Digitizer
BO	Buffer oil
CC	Charged-Current
DAQ	Data Acquistion
ES	Elastic Scattering
FEE	Front End Electronics
FPGA	Field Programmable Gate Array
GALLEX	GALLium EXperiment
GEANT	GEometry ANd Tracking toolkit
GLG4sim	Generic-LAND GEANT4 simulation
GNO	Gallium Neutrino Observatory
GPS	Global Positioning System
ID	Inner Detector
KamLAND	Kamioka Liquid scintillator Anti-Neutrino Detector
KLG4sim	KamLAND GEANT4 simulation
LS	Liquid Scintillator
LMA-I	Large Mixing Angle (region I)

MC	Monte Carlo
MESCO	Mitsui Engineering & Shipbuilding Company, LTD.
MSW	Mikheyv-Smirnov-Wolfenstein
NC	Neutral-Current
OD	Outer Detector
PC	1,2,4-Trimethylbenzene (Pseudocumene)
PPO	2,5-Dyphenyloxazole
PMT	Photomultiplier Tube
QCD	Quantum Chromodynamics
QED	Quantum Electrodynamics
ROOT	Object-Oriented Toolkit for data analysis developed by CERN
SAGE	Soviet-American Gallium Experiment
SK	Super-Kamiokande
SNO	Sudbury Neutrino Observatory
SNP	Solar Neutrino Problem
SNU	Solar Neutrino Unit (one interaction per 10^{36} target atoms per second)
SSM	Standard Solar Model
ZAMS	Zero Age Main Sequence
mG	milli-Gauss
mV	milli-Volt
p.e.	photo-electron

Contents

List of Tables

List of Figures

Chapter 1

A Concise History of the Neutrino

The description of weak interactions in physics spans over a century and was prompted when Henri Becquerel accidentally discovered radioactivity in Uranium [1]. The classification of the radioactive by-products, α, β, and γ particles, followed shortly thereafter. The continuous energy spectrum of β-decay was demonstrated in 1914 by James Chadwick [2]. This surprising result at the time seemed to indicate a violation of the fundamental laws of conservation of energy, momentum and angular momentum. In 1930, Wolfgang Pauli tried to rectify the problem by proposing the existence of a neutral weakly interacting particle emitted during β-decay. Initially, he called this particle a *neutron*, but Enrico Fermi later renamed the particle a *neutrino* after Chadwick discovered the modern-day neutron in 1932 [3].

The story of Fermi's neutrino is an interesting one. In 1933, Fermi had constructed a theory for beta decay, where a nucleus undergoes de-excitation by the emission of an electron: $n \rightarrow p + e^- + \overline{\nu}_e$. This was a necessary statement in order to explain electron emission spanning a continuum of energies. Fermi's theory allowed for the conservation of energy, where the neutrino carried off any remaining energy that did not go to the emitted electron. The idea was so profound that when Fermi tried to publish his paper in *Nature*, he was turned down by the editor. The reason for his

denial was that his paper contained, "abstract speculations too remote from physical reality" [4]. Instead, Fermi published his result in both Italian and German journals which made him one of the first physicists to lay the foundation for the theory of weak interactions. One of the most intriguing characteristics of Fermi's theory is that he did not try to build a very general and complex theory for weak interactions, but simply focused on strict fundamental hypotheses. This was probably his most well known trait as a physicist.

1.1 Experimental Milestones for Solar Neutrinos

The existence of the neutrino was not experimentally confirmed until the year 1960, when Fred Reines and Clyde Cowan measured electron anti-neutrinos at the Savannah River nuclear reactor [5]. The reactor provided them with an anti-neutrino flux of 1.2×10^{13} cm^{-2} s^{-1} at the location of the detector, giving them a much greater flux than any other man-made sources at the time. Their experiment was made up of two 200 liter water targets placed between large liquid scintillation detectors. The detection scheme used the inverse beta decay reaction, $\overline{\nu}_e + p \rightarrow n + e^+$. The emitted positron provided a prompt signal by creating a pair of 0.511 MeV annihilation gammas which were detected via the scintillation detectors. The neutron was captured by cadmium dissolved into the water with a characteristic time that depended on the cadmium concentration, and emitted neutron capture gammas giving a delayed signal. This characteristic delayed-coincidence signal was used to identify anti-neutrino events.

Not too long after the confirmation of the electron anti-neutrino, Ray Davis' Homestake experiment detected electron neutrinos coming from the Sun. The Homestake detector was located 4,850 feet underground and was made of a large tank

holding 520 tons of chlorine in the form of C_2Cl_4 that made use of the neutrino capture reaction, $^{37}\mathrm{Cl} + \nu_e \rightarrow {}^{37}\mathrm{Ar} + e^-$, with a detection threshold on the neutrino energy of 0.814 MeV. The ^{7}Be and ^{8}B solar neutrinos were the main contribution to the flux measured by this experiment. The resulting ^{37}Ar atoms produced in the neutrino reactions were counted with miniature proportional counters. The initial results of this experiment found a solar neutrino flux of 3 SNU, where SNU stands for solar neutrino unit (one interaction per 10^{36} target atoms per second) [6]. Later on, John Bahcall and Ray Davis published a paper showing that the measured solar neutrino flux from the Homestake experiment was about a factor of three lower than expected from theoretical calculations. This discrepancy between theoretical predictions of the solar neutrino flux and the results of the Homestake experiment led to what was known as the Solar Neutrino Problem (SNP) [7].

The discrepancy between Homestake and solar model calculations was later confirmed by the Kamiokande experiment. Kamiokande was a 2,142 metric ton, water Čerenkov detector, which was upgraded in 1986 to Kamiokande-II in order to improve sensitivity to ^{8}B solar neutrinos. The signal from solar neutrinos came from the elastic scattering of neutrinos (of flavor α) off of electrons, $\nu_\ell + e^- \rightarrow \nu_\ell + e^-$. This reaction differed from the Homestake experiment by being senstive to all flavors of neutrinos, however, the electron neutrino has a dominant cross-section. One unique advantage to using a water Čerenkov detector is that the directionality of the neutrino could be extracted due to a relatively small scattering angle. In 1990, Kamiokande-II released results showing a measured deficit of the solar neutrino flux of about one half when compared to the current calculations [8]. These results also showed, by means of the directionality of these neutrinos, that they were coming from the Sun. This in itself was a profound result that provided, for the first time, direct evidence that solar power is indeed due to nuclear fusion.

In 1996, the successor of Kamiokande, called Super Kamiokande (SK), made a precision measurement of the ^{8}B solar neutrino flux. SK was able to utilize its enormous fiducial mass of 22.5 kton to acquire very high statistics (the highest to date out of any solar neutrino experiment), and confirmed the Kamiokande solar neutrino deficit[9].

Shortly after Kamiokande-II, another series of radiochemical experiments were developed using Gallium as the target in the reaction, $\nu_e + ^{71}\text{Ga} \rightarrow ^{71}\text{Ge} + e^-$. This reaction has a very low neutrino energy threshold of 0.233 MeV, allowing detection of all sources of solar neutrinos. From 1991 to 2003, the GALLEX/GNO experiments, in Gran Sasso National Laboratory, measured a rate of about half the predicted solar neutrino flux [10]. From 1990 to 1997 the SAGE experiment, in the Baksan Neutrino Observatory, also measured a rate of about half the predicted solar neutrino flux and was in agreement with the GALLEX/GNO results [11].

The most elaborate measurement of the solar neutrino flux was made by the Sudbury Neutrino Observatory (SNO), located in Canada. The SNO detector was a one-kiloton, heavy water Čerenkov detector, and had the ability to detect solar neutrinos with a neutrino flavor dependent signature through the charged-current (CC), neutral-current (NC), and elastic scattering (ES) reactions:

$$\begin{aligned} \text{(CC)} \quad & \nu_e + d \rightarrow p + p + e^-, \\ \text{(NC)} \quad & \nu_\ell + d \rightarrow p + n + \nu_\ell, \\ \text{(ES)} \quad & \nu_\ell + e^- \rightarrow \nu_\ell + e^-, \end{aligned}$$

where α is equal to e, μ, or τ. The CC reaction on deuterium is useful as a cross-check of the ^{8}B neutrino flux deficit since the neutrino energy threshold for this reaction in the SNO detector was 6.9 MeV. The ES reaction is the same that was used in the Kamiokande and SK detectors and made it sensitive to ^{8}B neutrinos only. The NC

reaction on deuterium had the ability to measure all flavors of neutrinos with equal sensitivity, which provided a means for testing neutrino flavor conversion. This was the first time that physicists had a way of measuring the total ^{8}B solar neutrino flux, taking into account flavor conversion.

The SNO experiment was performed in three separate phases. The first phase, called the D_2O phase, confirmed the previous deficits seen in the electron flavor solar neutrino flux [12]. During this phase, the NC reaction revealed that 2/3 of the electron neutrinos change flavor to muon or tau neutrinos on their way from the Sun to the Earth. This provided the first evidence that flavor conversion is the cause of the SNP, a phenomenon that had eluded all previous experiments that were not equally sensitive to all flavors. The second phase, called the salt phase, was performed with about two tons of NaCl added into the heavy water. This improved the solar neutrino detection efficiency of the NC reaction, and provided a better separation of the NC and CC signals. During the second phase the previous results of the D_2O phase were confirmed with high precision [13]. The third phase of SNO employed a grid of ^{3}He proportional counter tubes to detect the resulting neutron indicative of a NC solar neutrino reaction. This phase began in 2005 and provided an independent measurement of the NC reaction [14].

1.2 Current Status and KamLAND Involvement

The three flavor measurement by SNO was a major milestone in solar neutrino experiments. This result confirmed estimates of the solar neutrino flux given by the SSM with reasonable accuracy, and provided direct evidence that flavor conversion did exist. Flavor conversion for solar neutrinos can be realized in two different ways: flavor conversion occurs as neutrinos travel through the vacuum between the Sun and the Earth, or it is caused by matter effects in the interior of the Sun. Flavor

oscillation was first discussed by Bruno Pontecorvo in 1967 [15], where the flavor eigenstates are written as linear combinations of the mass eigenstates. Later on, in 1978, Lincoln Wolfenstein developed the groundwork for flavor oscillations in matter [16]. This description was also accompanied by work performed by Stanislav Mikheyev and Alexei Smirnov in 1986 [17], which outlined matter enhanced flavor conversion inside the Sun. The mechanism enabling adiabatic matter enhanced flavor conversion is known as the (Mikheyv-Smirnov-Wolfenstein) MSW effect. The foundations of neutrino oscillations and matter effects are outlined in further detail in Chap. 3.

Early evidence of flavor disappearance from solar neutrino experiments prompted new experiments to seek out flavor oscillations. These experiments were built to search for vacuum oscillations of electron anti-neutrinos coming from nuclear reactors, because of the predictability of the total anti-neutrino flux at the reactor core. Many of the initial experiments were constructed within 10 m to 1 km of the reactors, and because of their close proximity, they saw no significant deficit of anti-neutrinos.

KamLAND was first proposed to measure a deficit of anti-neutrinos from reactors, and was placed in the Kamioka Underground Laboratory where its distance from Japan's 55 various reactors can be approximated as a single source at $\sim$180 km. This characteristic distance was crucial in KamLAND's high precision measurement of neutrino oscillation parameters, which at the time, were explained by several different allowed regions. KamLAND singled out the Large Mixing Angle (LMA-I) solution from other possibilites and showed the existence of neutrino oscillations [18] [19]. The detection mechanism utilizes a prompt and delay signal from inverse beta decay, just as previous reactor experiments had done. The detector volume utilizes one-kiloton of liquid scintillator, making it the largest reactor neutrino experiment in the world.

Along with a precision measurement of reactor neutrino oscillations, KamLAND was also able to utilize the same detection mechanism to make the first observation

of geologically produced anti-neutrinos from ^{238}U and ^{232}Th decays in the Earth's interior [20]. It was only because the reactor spectrum was very well known that KamLAND was able to observe evidence of geologically produced anti-neutrinos, since these neutrinos form a small part of the background for reactor anti-neutrinos.

With regard to solar neutrinos, the SNP is no longer a scientific issue and can be explained by the MSW effect. Instead, a new problem involving the solar heavy element abundance (heavier than boron) has come to light and now interests physicists who are working on simulations performed to precisely model the Sun. This uncertainty in the heavy element abundance affects the individual neutrino flux uncertainties in computer simulations of the Sun and will be covered in further detail in Chap. 2. The neutrino fluxes can be used to determine the fusion reaction rates for various isotopes inside the Sun's core, and serve as input into the simulations with hopes of reproducing other measureable characteristics. A real-time measurement of the ^{7}Be solar neutrino flux (a monoenergetic, 0.862 MeV neutrino) would provide physicists working on simulations of the Sun an important constraint on their inputs.

In 2005, the KamLAND collaboration decided to take advatage of this opportunity and try to observe ^{7}Be solar neutrinos. The collaboration began working on ways to reduce radioimpurities in the liquid scintillator to unprecedented levels. Achieving ultra-low background inside the KamLAND detector is the only way to detect solar neutrinos below 1 MeV, where natural, cosmogenic, and man-made radio-impurities originally dominated the signal. The detection mechanism uses neutrino-electron elastic scattering as done by Kamiokande, Super-Kamiokande, and SNO before, which can't be differentiated from backgrounds unlike the prompt and delayed signal of inverse beta decay.

Another experiment, called Borexino, similar in design to KamLAND was constructed to measure solar neutrinos. This experiment utilized a fiducial mass of

78.5 tons of liquid scintillator as the detector target. The most recent Borexino measurement of the ^{7}Be solar neutrino flux used 740.7 days of data in 2011 [21]. The measured interaction rate was $46.0 \pm 1.5(\text{stat})\pm^{+1.5}_{-1.6}(\text{syst})$ counts/(100 ton·day), which is equivalent to a total measured ^{7}Be solar neutrino flux of $(4.84 \pm 0.24) \times 10^9$ cm^{-2}s^{-1}. The measured flux was in very good agreement with the SSM prediction of $(4.64 \pm 0.06) \times 10^9$ cm^{-2}s^{-1}. A independent observation of this flux by KamLAND would provide a direct cross-check of solar models.

Chapter 2

The Standard Solar Model

Within close proximity to Earth, the Sun is a very powerful source of neutrinos providing us with unique insight into the energy production of similar main sequence stars. The underlying mechanism for this energy production is thermonuclear fusion. Our understanding is that the formation of a star comes from the gravitational collapse of a cloud of hydrogen gas. The gas is heated by the contraction until the temperature is sufficient to ignite thermonuclear reactions by the penetration of the Coulomb barrier between nulcei. These nuclear reactions produce neutrinos, many of which have a direct route from the core of the Sun to the surface. Neutrinos, unlike photons which undergo a random walk from their location of production to the surface lasting $\sim 10^4$ years, give physicists a direct probe into the deepest parts of the Sun. A simple diagram depicting the Sun is shown in Fig. 2.1. This chapter gives a brief overview of the modeling of stellar structure which is used to calculate solar neutrino fluxes.

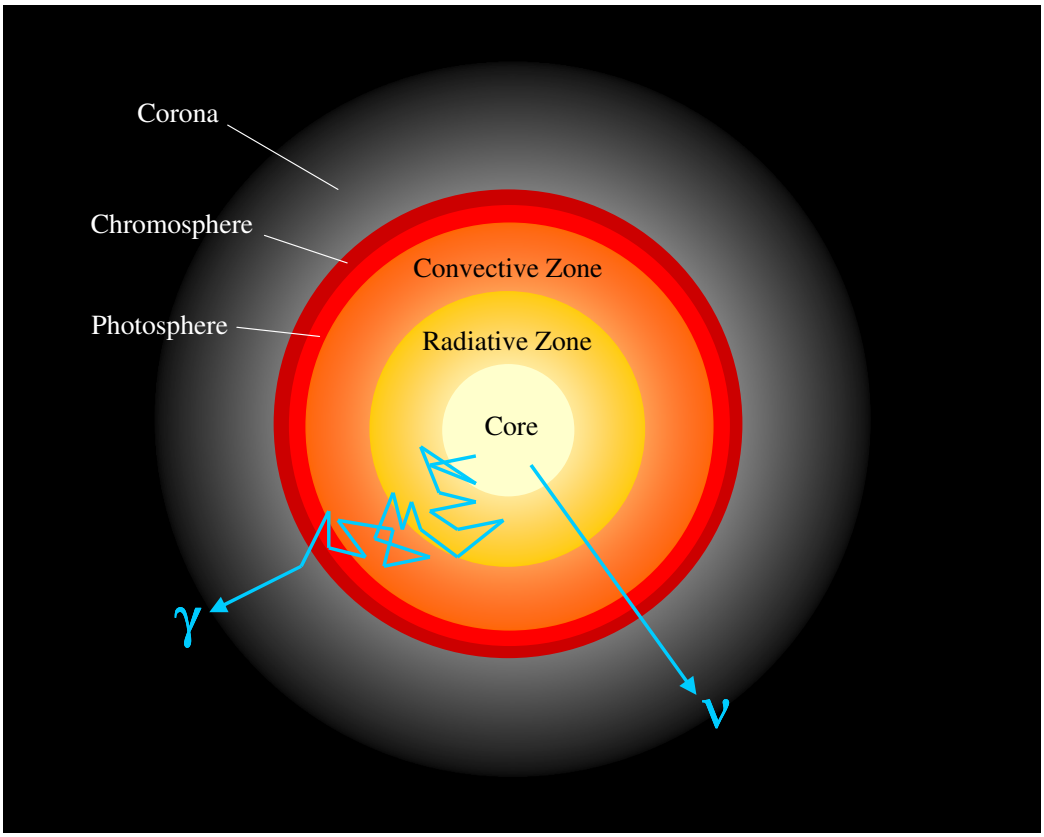

Figure 2.1: A simple diagram depicting the different regions of the Sun (not drawn to scale). A photon produced at the center takes a long random path before exiting the Sun. A neutrino, produced at the core, exits the Sun almost immediately giving physicists on Earth an opportunity to extract valuable information about the Sun's interior.

2.1 Fundamentals of Stellar Structure

The Sun is a long-lived, main sequence star which exists in its Hydrogen burning phase. This rather stable existence, compared to more exotic astronomical objects, makes the Sun among other obvious advantages an ideal candidate for the study of stellar evolution. The prescription of stellar evolution requires only basic physics equations. In order to reduce the complexity of the modelling of stellar evolution, the two assumptions made are: spherical shape and spherical symmetry. Phenomena

such as rotation, mass loss and magnetic fields are not considered. The notation used here is from Ref. [22]. Another detailed review of stellar structure and evolution can be found in Ref. [23].

The first of these equations describes the mass continuity governing the interior of the Sun and is given as:

$$\frac{dm}{dr} = 4\pi r^2 \rho(r), \tag{2.1}$$

where $\rho(r)$ is the density at a radius r, and m is the mass encompassed at a radius r. Multiplying both sides of Eq. 2.1 by dr and integrating over the entire solar radius will result in the total solar mass.

The next equation represents hydrostatic equilibrium, where radiation pressure balances the gravitational force. This condition is satisfied for long-lived stars such as our Sun and is given as:

$$\frac{dP}{dm} = -\frac{Gm}{4\pi r^4}, \tag{2.2}$$

where P is the pressure and G is the Gravitational constant. This is better understood by solving for dm in Eq. 2.1 substituting into Eq. 2.2.

The nuclear reactions in the core of the Sun result in an energy, l, to flow through a shell of radius r per unit time. The energy released by nuclear reactions is denoted as ϵ. Energy is also carried away by neutrinos exiting the Sun. This energy is denoted as ϵ_ν. These terms appear in an equation expressing conservation of energy:

$$\frac{dl}{dm} = \epsilon - \epsilon_\nu - C_P \frac{dT}{dt} + \frac{\delta}{\rho}\frac{dP}{dt}, \tag{2.3}$$

where C_P is the specific heat at constant pressure, T is the temperature, and t is the time. The variable δ comes from the equation of state and is defined as:

$$\delta = -\left(\frac{\partial \ln\rho}{\partial \ln T}\right)_{P,X_i}, \tag{2.4}$$

where the P and X_i subscripts denote constant pressure and chemical composition. The last two terms in Eq. 2.3, involving the specific heat and the equation of state variable, come from the gravitational release of energy or, for example, when internal energy changes due to work done in expansion. The derivation of these two terms uses the first law of thermodynamics. It is derived in detail in Refs. [24] and [25].

Another important aspect of solar modelling involves the description of energy transport inside the Sun due to a temperature gradient between the core and the outer layers. Taking into account Eq. 2.2, this equation can be written in the form:

$$\frac{dT}{dm} = -\frac{GmT}{4\pi r^4 P}\nabla, \tag{2.5}$$

where $\nabla = d\ \ln T/d\ \ln P$ is a dimensionless temperature gradient. This temperature gradient depends heavily on the position inside the Sun. In the radiative zones it is given by:

$$\nabla_{\rm rad} = -\frac{3}{64\pi\sigma G}\frac{\kappa l P}{m T^4}, \tag{2.6}$$

where σ is the Stefan-Boltzmann constant and κ is the total opacity. The total opacity is a combination of the radiative opacity and conductive opacity, which are measures

of the transparencies for photons and electrons, respectively. More complicated calculations are needed when energy is transported by convection, especially in the outer layers.

Eq. 2.7 describes the changing chemical composition of the Sun over time. This change in composition can be attributed to three different mechanisms: nuclear reactions, the changing boundaries of convection zones, and diffusion of Helium and heavier elements. For neutrino flux predictions the change in composition due to nuclear reactions is most important. Considering nuclear reactions, if X_i is the mass fraction of any isotope i, then the rate of change in X_i over time can be expressed as:

$$\frac{\partial X_i}{\partial t} = \frac{m_i}{\rho}\left[\sum_j r_{ji} - \sum_k r_{ik}\right], \tag{2.7}$$

where m_i is the mass of the nucleas of each isotope i, r_{ij} is the rate at which isotope i is formed from isotope j, and r_{ik} is the rate at which isotope i is lost as it turns into isotope k. The convection or diffusion of chemical abundances throughout the interior over time is also included in the model.

All of the equations listed above form the complete set of relations that govern stellar structure and evolution. These equations are solved for a given chemical abundance at a given time in an iterative process. The four boundary conditions that need to be satisfied for the model are the radius, luminosity, temperature and pressure. The initial conditions for the model depend on where the evolution is started for the star. The evolution can start when the gas is still collapsing (pre-main sequence), or it can start at the onset of nuclear fusion, also know as Zero Age Main Sequence (ZAMS).

Given this set of five equations with six unknowns (r, P, l, T, X_i, ρ), a relation is needed which connects the density, ρ, to the other five quantities. This relation is

given by an equation of state. Modern equations of state are given in a tabular form with interpolations done in order to obtain the quantities needed to solve the equations [22]. Other quantities needed are the opacity and the nuclear reaction rates. The opacity is usually given in a tabular form just like the equation of state, and among the most common are those given by the Opacity Project (OP) [26]. The nuclear reaction rates are necessary to calculate the energy generated, the neutrino flux, and the composition changes. The rates are obtained by extrapolation from laboratory measurements, or in some cases come from theoretical calculations. There are typically two adjustable parameters in the model, mainly, the initial helium and heavy element abundance and the convective mixing length parameter. Both of these parameters are determined in order to reproduce the solar radius and luminosity. Once these parameters are chosen, the solar model is allowed to evolve to the Sun's current age by solving the stellar equations. This model is formally known as the Standard Solar Model (SSM). The details of a recent standard solar model simulation can be found in Ref. [27].

Independent verification of the SSM can be made by helioseismology, which is the study of acoustic vibrations inside the convective zone of the Sun. The sound waves are trapped beneath the solar surface by reflections due to the density gradient, and trapped above the lower boundary of the convective zone due to refractions caused by the increasing sound speed. Solar models compare the calculated density and sound speed profiles with those measured by helioseismology to test for accuracy. Recent SSM calculations show that a large discrepancy exists between the models and helioseismology, as seen in Ref. [28]. The new SSM calculations use estimates of heavy element abundances obtained from meteorites, and are thought to be more precise than older SSM calculations. This suggests that revised opacities are needed to mend the problem.

Another way to test the SSM is to measure the neutrino fluxes on Earth, which is the main focus of this work. The SSM predicts the location and rate of the nuclear reactions in the Sun's interior, and allows for a calculation of the expected neutrino flux on Earth due to the different nuclear reactions.

2.2 Neutrino Production in the Sun

Thermonuclear fusion in stars was first outlined in the detailed work of Hans Bethe, where various reactions responsible for energy production were proposed [29], [30]. One of the main results from Bethe's work is that Helium is the heaviest element which can be built up to any large abundance, and that the heavier elements were assumed to be present before the Sun reached its current state of temperature and density. The creation of Helium comes from the fusion of four protons (forming an α-particle). This can be achieved through a variety of reactions, some of which will produce neutrinos. The first of these reactions is given as:

$$p + p \rightarrow {}^{2}\mathrm{H} + e^{+} + \nu_e + 0.420\,\mathrm{MeV}, \tag{2.8}$$

which is known as the *pp* reaction. This is the primary reaction responsible for the hydrogen burning phase of the Sun and produces a neutrino with a continuous energy spectrum (known as the *pp* neutrino). The reaction is very slow and is the determining factor in the Sun's lifetime, which is estimated to be $\sim 1.2 \times 10^{10}$ years [31]. There are two other reactions that can follow:

$${}^{2}\mathrm{H} + p \rightarrow {}^{3}\mathrm{H} + \gamma + 5.494\,\mathrm{MeV}, \tag{2.9}$$

$${}^{3}\mathrm{He} + {}^{3}\mathrm{He} \rightarrow {}^{4}\mathrm{He} + 2p + 12.860\,\mathrm{MeV}. \tag{2.10}$$

This series of reactions forms the main branch of what is called the *pp*-I chain of nuclear reactions, with the net result being the conversion of hydrogen into helium. There are two other neutrinos with continuous energy spectra produced in the *pp*-I chain, called the *pep* neutrino and the *hep* neutrino. After reaching the production of ^{7}Be, the *pp*-I chain splits into two separate chains: the *pp*-II chain and the *pp*-III chain. The *pp*-II chain involves the capture of an electron on ^{7}Be, producing ^{7}Li and a monoenergetic neutrino (referred to as the ^{7}Be neutrino). The *pp*-II chain terminates when ^{7}Li combines with a proton to produce two Helium nuclei. The *pp*-III chain involves ^{7}Be combining with a proton to produce ^{8}B. The ^{8}B decays via positron emission to ^{8}Be, producing a neutrino with a continuous energy spectrum (referred to as the ^{8}B neutrino). The *pp*-III chains terminates with ^{8}Be undergoing fission to produce two Helium nuclei.

There is another mechanism that produces Helium, where ^{12}C is used as a catalyst. In this mechanism, isotopes of C, N and O are fused with protons in a cyclic nature that reproduces ^{12}C. This cycle produces three different neutrinos of continuous energy from positron decay of ^{13}N, ^{15}O, and ^{17}F. The corresponding neutrinos are called the ^{13}N, ^{15}O, and ^{17}F neutrinos, and the sum of their energy spectra is commonly called the CNO neutrino spectrum. All of the thermonuclear reactions contained in the *pp* chain and the CNO cycle are shown in Fig. 2.2 and Fig. 2.3 respectively. Both of these groups of reactions make up roughly 99% of the energy production in the Sun, with the CNO cycle accounting for a couple of percent [31].

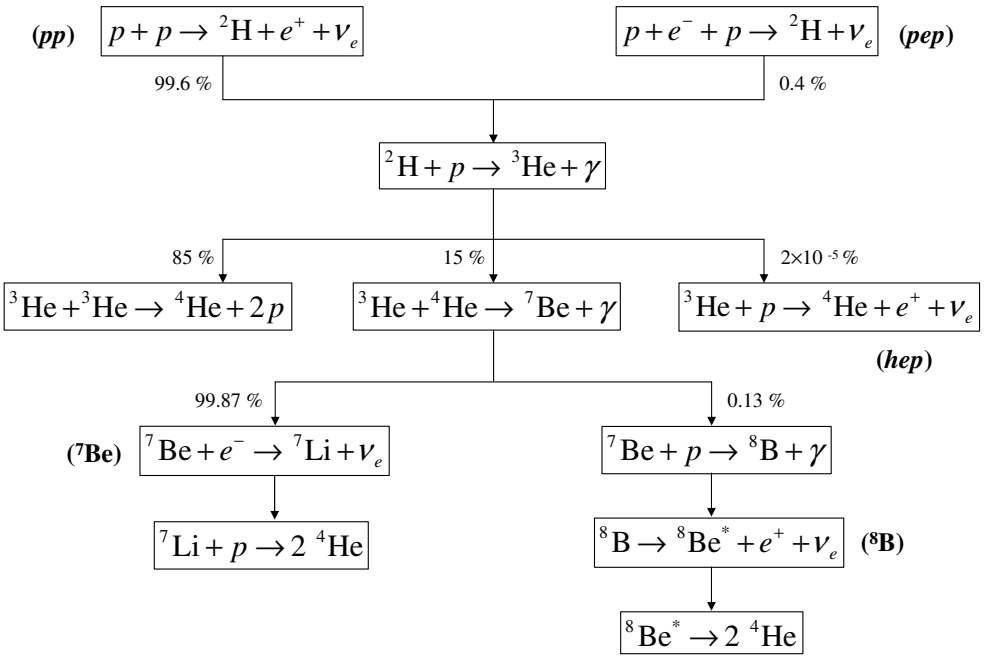

Figure 2.2: The *pp* chain reactions with the neutrino producing branches labeled in parentheses. The branching ratios for the reactions are taken from Ref. [32].

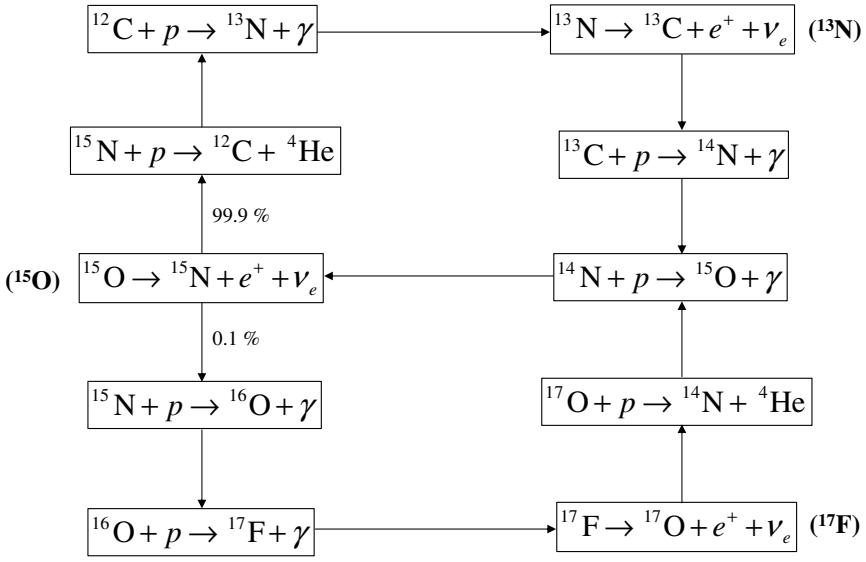

Figure 2.3: The CNO cycle reactions with the neutrino producing branches labeled in parentheses. The branching ratios for the reactions are taken from Ref. [32].

2.3 Standard Solar Model Predictions

The SSM is used to calculate the expected fluxes of solar neutrinos. The most recent SSM calculations, at the time this work was being performed, were made by A. Serenelli, et al. [28]. The calculations of the neutrino fluxes presented here are referenced from this work. The model, called AGSS09, uses the most recent heavy element abundance inputs that come from both meteoric and photospheric measurements. These newly determined heavy element abundances are significantly lower than what has been derived from older measurements used in the solar model by Grevesse and Sauval in 1998 (GS98) [33], and are slightly lower than an older solar model by Asplund, Grevesse and Sauval in 2005 (AGS05) [34]. Another model, called AGSS09ph, was made using only the photospherically determined abundances for a separate comparison.

Given this change of inputs compared to earlier models, the AGSS09 model shows large disagreements between the sound speed and density profiles, of 5σ and 11σ respectively, when compared to helioseismological data. Plots of the relative differences between the sound speed and density profile for SSMs and helioseismological results are shown in Fig. 2.4. The AGSS09ph model is seen to have slightly better agreement with helioseismological results, but the photospheric abundances have a slightly larger uncertainty than those determined from meteoritic analysis. The AGSS09 model is the prefered choice given that meteoritic abundances are more robust than photospheric abundances. Furthermore, the AGSS09 model was found to have better agreement with helioseismological data by making changes to the solar opacity. This is a question that requires more conclusive experimental evidence in order to be resolved.

The individual solar neutrino fluxes from the AGSS09 and AGSS09ph models (without oscillations) are shown in comparison with the older GS98 model in Table

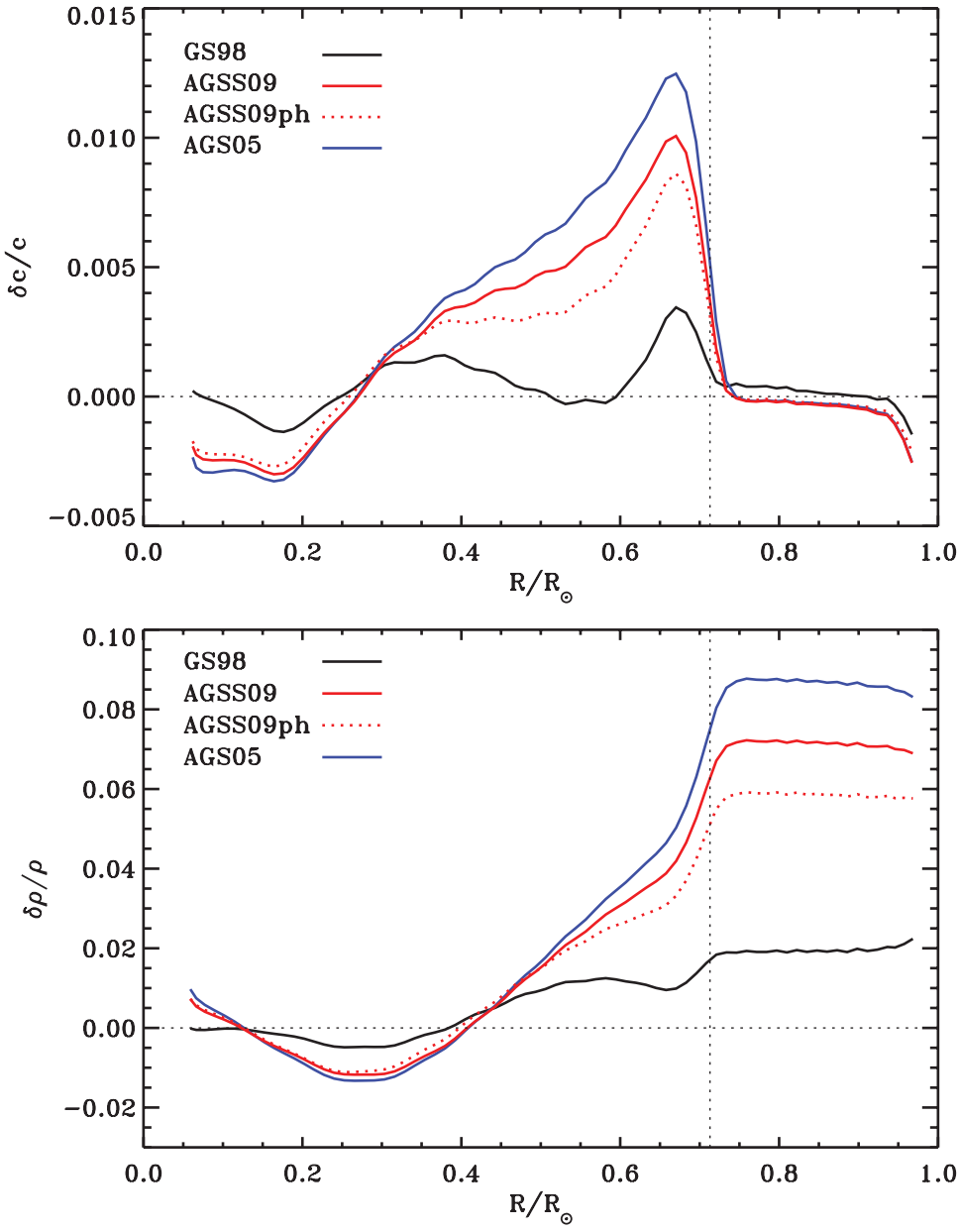

Figure 2.4: A comparison between different SSMs and helioseismological measurements as a function of solar radius. The top plot shows the relative sound speed comparison between different models. The bottom plot depicts the density comparison, where $\delta c/c$ and $\delta\rho/\rho$ are defined as (Helioseismology - SSM)/SSM. These plots are taken from Ref. [28].

Source	GS98	AGSS09	AGSS09ph	Units [cm^2s^{-1}]
pp	5.97 ± 0.006	6.03 ± 0.005	6.01 ± 0.005	10^{10}
pep	1.41 ± 0.011	1.44 ± 0.010	1.43 ± 0.010	10^8
hep	7.91 ± 0.15	8.18 ± 0.15	8.10 ± 0.15	10^3
^{7}Be	5.08 ± 0.06	4.64 ± 0.06	4.79 ± 0.06	10^9
^{8}B	5.88 ± 0.11	4.85 ± 0.12	5.22 ± 0.12	10^6
^{13}N	2.82 ± 0.14	$2.07^{+0.14}_{-0.13}$	$2.15^{+0.14}_{-0.13}$	10^8
^{15}O	$2.09^{+0.16}_{-0.15}$	$1.47^{+0.16}_{-0.15}$	$1.55^{+0.16}_{-0.15}$	10^8
^{17}F	$5.65^{+0.17}_{-0.16}$	$3.48^{+0.17}_{-0.16}$	$3.70^{+0.17}_{-0.16}$	10^6

Table 2.1: Calculated solar neutrino fluxes from three different SSMs. The differences between the GS98 and AGSS09 solar neutrino fluxes becomes largest for the ^{8}B, ^{13}N, ^{15}O and ^{17}F neutrinos where the differences are 18%, 27%, 30%, and 38%, respectively.

2.1. When comparing the solar neutrino fluxes in the GS98 model to the ones of the AGSS09 model, differences of 9% and 18% can be seen for ^{7}Be and ^{8}B neutrinos, respectively. For ^{13}N, ^{15}O and ^{17}F neutrinos the differences become 27%, 30% and 38%. These fluxes have a strong dependence on the heavy element abundance. The uncertainties in the abundance could be greatly reduced with a direct measurement of the CNO neutrino flux, which has the largest uncertainty in SSMs from its strong dependence on heavy element abundances. With knowledge of the CNO flux, physicists could constrain the abundances of heavy elements responsible for producing these neutrinos in SSMs. However, a real-time measurement of the CNO flux is a difficult undertaking due to backgrounds from ^{11}C, which is a byproduct of cosmic rays passing through detector materials. This problem with the disagreement between helioseismological data and solar models using newly determined heavy element abundances has been labeled "The Solar Composition Problem" and is the modern day puzzle facing astrophysicists.

The total solar neutrino fluxes calculated from AGSS09 are plotted in Fig. 2.5.

The energy distributions were originally determined from laboratory experiments, normalized to unity, and scaled to the total expected fluxes predicted by SSMs without the effect of oscillations [35]. The ^{8}B spectrum used in this work was taken from a measurement in Ref. [36]. Effects from possible electron-capture modes in the CNO neutrino spectra are not taken into account in these calculations. The ^{7}Be neutrino emission lines have an asymmetric broadening applied to them. This broadening of the shape comes from a combination of first-order Doppler effects and decay kinematics, which are a result of the high solar temperature in the core of the Sun. For a more detailed discussion on the exact shape of the ^{7}Be neutrino emission lines see Ref. [37]. The broadening is only an academic point to be made and cannot be observed given the resolution of large liquid scintillation detectors.

Along with the total solar neutrino fluxes, SSMs also give predictions of the production distribution of solar neutrinos in the Sun's interior. These distributions are useful when incorporating neutrino adiabatic flavor change from matter effects. To perform realistic calculations of the expected neutrino-electron elastic scattering signal in experiments like KamLAND, flavor transitions of neutrinos need to be taken into account. Details on these calculations are presented in Chap. 3. The normalized solar neutrino production distributions from AGSS09 are shown in Fig. 2.6, where the fractional production for each type of solar neutrino is plotted as a function of solar radius.

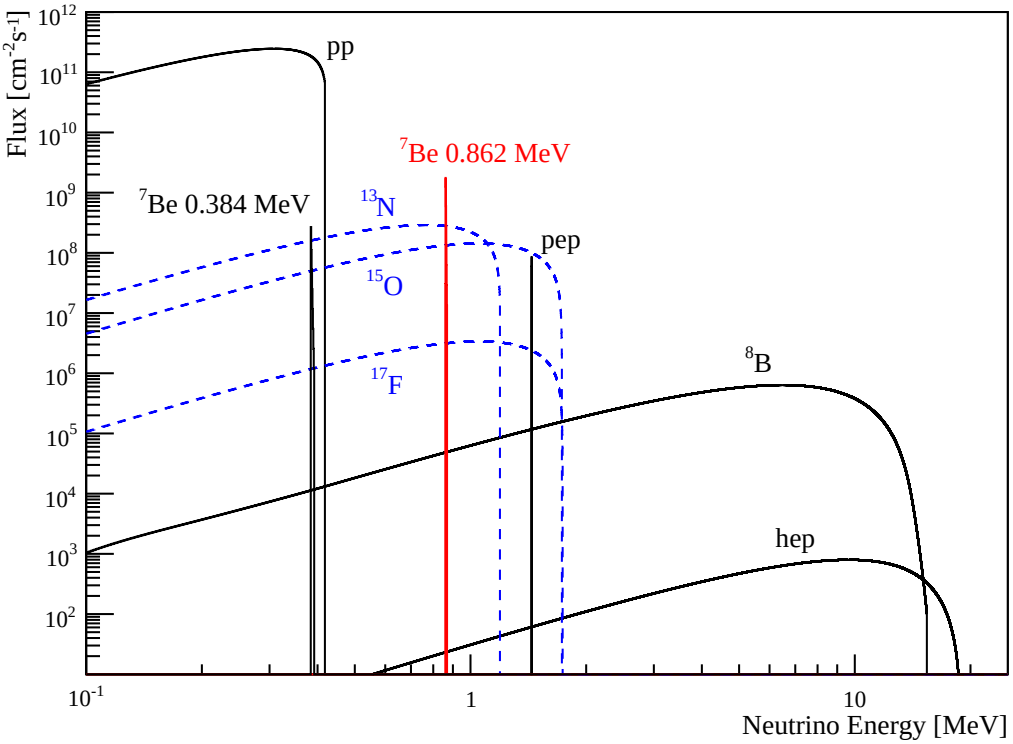

Figure 2.5: The solar neutrino energy distributions scaled to the predicted rates from AGSS09. The ^{8}B distribution was taken from Ref. [36], while the others were taken from Ref. [35]. Thermal broadening has been applied to the ^{7}Be lines as prescribed in Ref. [37].

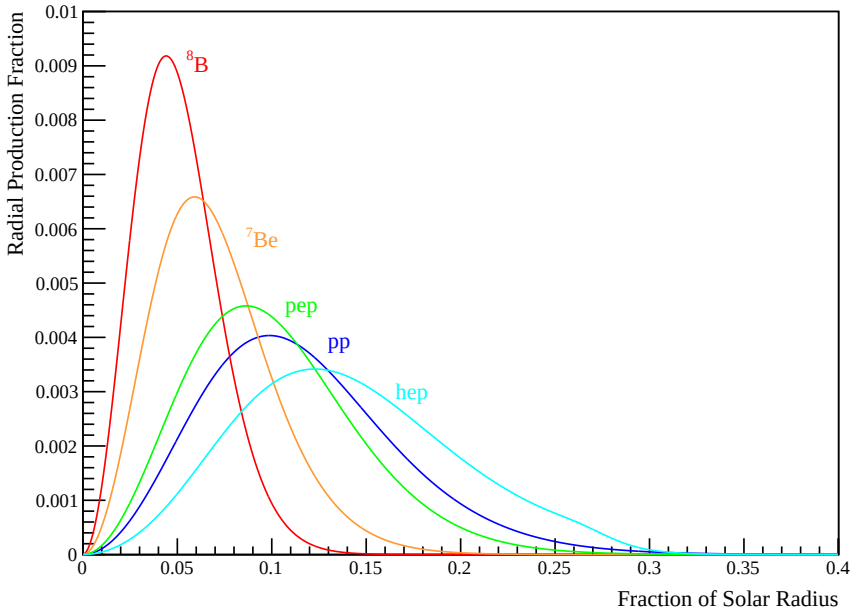

(a)

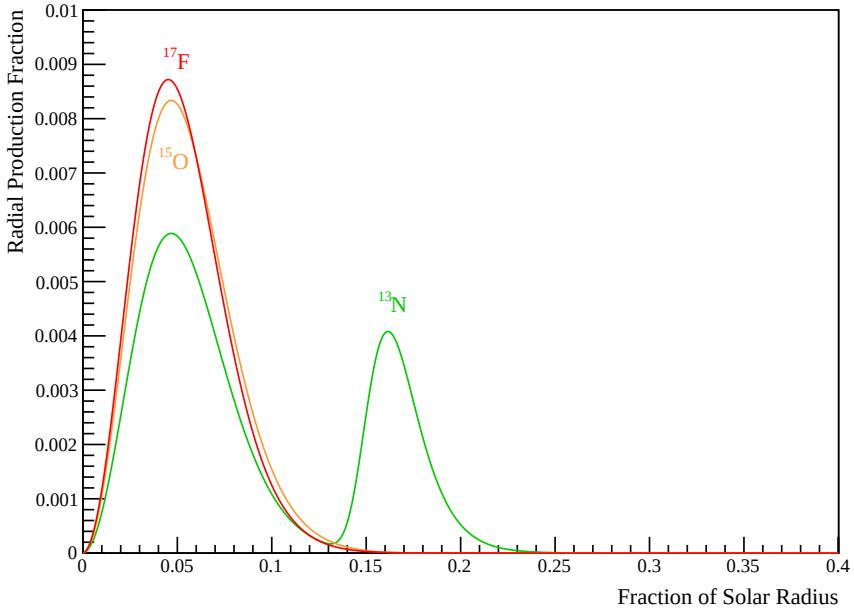

(b)

Figure 2.6: The fractional production of solar neutrinos as a function of solar radius. Plot (a) shows the distributions for the pp, pep, hep, ^{7}Be, and ^{8}B neutrinos and plot (b) shows the distributions of the ^{13}N, ^{15}O, and ^{17}F neutrinos.

Chapter 3

Neutrino Physics

Making measurements of solar neutrinos using terrestrial detectors makes an underlying assumption that particle physics works the same way in the core of the Sun as it does in laboratories on Earth. When the SNP came to light, many physicists questioned whether the Standard Model of elementary particles provided an accurate description of neutrinos. The solution to the SNP came not from an astrophysical modfication to SSMs, but from a new form of particle physics not incorporated into the Standard Model: neutrino oscillations.

An outline of the Standard Model will be given as it pertains to neutrinos. More specifically, the discussion will involve massive neutrinos, a condition which is necessary for flavor oscillations to exist. A derivation of neutrino oscillations in vacuum is provided, and the extension to adiabatic flavor change in matter is briefly summarized. The resulting cross-sections for neutrino-electron elastic scattering are calculated and used to predict the observable signal for ^{7}Be solar neutrinos in KamLAND.

3.1 Standard Model of Elementary Particles

The Standard Model (SM) was developed to describe all of the interactions of elementary particles. The model incorporates the weak, strong and electromagnetic forces while leaving out gravity. It was created with the help of Sheldon Glashow, Steven Weinberg, and Abdus Salam, who shared the 1979 Nobel Prize for their efforts. The SM is laid out in the framework of a gauge theory based on the local symmetry group $\mathrm{SU}(3)_C \otimes \mathrm{SU}(2)_L \otimes \mathrm{U}(1)_Y$, where C stands for color, L stands for left-handed chirality, and Y stands for weak hypercharge. In this gauge group, the number of vector gauge bosons correspond to the group generators, which are the eight massless gluons of $\mathrm{SU}(3)_C$, the massive $W^{\pm}$ and Z^0 of $\mathrm{SU}(2)_L$, and the massless photon of $\mathrm{U}(1)_Y$. These gauge bosons are responsible for the interactions between particles.

All matter in the SM is composed of six quarks (u, d, c, s, t, b) and six leptons $(e, \nu_e, \mu, \nu_\mu, \tau, \nu_\tau)$, each of these having an anti-particle for a total of 24 fermions (spin-1/2 particles). The masses of the fermions and of the $W^{\pm}$ and Z^0 arise through spontaneous symmetry breaking, which is described by the Higgs mechanism. The electroweak, $\mathrm{SU}(2)_L \otimes \mathrm{U}(1)_Y$, part of the SM determines the interactions of leptons and neutrinos. It is only necessary to discuss the electroweak interactions appropriate for neutrino detection, and they will be considered separately from the strong interactions determined by $\mathrm{SU}(3)_C$.

In the electroweak interactions, the left-handed chiral components (denoted with subscript L) of leptons are represented as weak isospin doublets:

$$L_e = \begin{pmatrix} \nu_{eL} \\ e_L \end{pmatrix} \qquad L_\mu = \begin{pmatrix} \nu_{\mu L} \\ \mu_L \end{pmatrix} \qquad L_\tau = \begin{pmatrix} \nu_{\tau L} \\ \tau_L \end{pmatrix} \tag{3.1}$$

where the left-handed states (denoted by subscript L) are given as:

$$\begin{aligned} \nu_{\ell L} &= \tfrac{1}{2}(1-\gamma^5)\nu_\ell \\ \ell_L &= \tfrac{1}{2}(1-\gamma^5))\ell \end{aligned} \qquad \ell = e, \mu, \text{or } \tau. \tag{3.2}$$

Here, $\gamma^5 = i\,\gamma^0\gamma^1\gamma^2\gamma^3$, is the chirality matrix which is a multiplicative combination of the Dirac matrices. In the SM, neutrinos are assumed to be massless, and consequently, do not have right-handed components. The assumption that neutrinos are massless is not necessarily correct, and the evidence for massive neutrinos will be presented in Sec. 3.2. The right-handed components of the other leptons (denoted by subscript R) are assumed to be singlets:

$$\ell_R = \frac{1}{2}(1+\gamma^5)\ell \qquad \ell = e, \mu, \text{or } \tau. \tag{3.3}$$

The charged-current (CC) and neutral-current (NC) Lagrangian terms can be constructed from a combination of components given in Eq. 3.2 and Eq. 3.3. Both of these are shown below:

$$\mathscr{L}_{(\text{CC})} = -\frac{g}{\sqrt{2}} \sum_{\ell=e,\mu,\tau} \overline{\nu_{\ell L}}\,\gamma^\mu\,\ell_L\,W_\mu + \text{h.c.} \tag{3.4}$$

$$\mathscr{L}_{(\text{NC})} = -\frac{g}{2\cos\theta_W} \sum_{\ell=e,\mu,\tau} \left(\overline{\nu_{\ell L}}\,\gamma^\mu\,\nu_{\ell L} + 2\,g_L^\ell\,\overline{\ell_L}\,\gamma^\mu\,\ell_L + 2\,g_R^\ell\,\overline{\ell_R}\,\gamma^\mu\,\ell_R\right) Z_\mu \tag{3.5}$$

Here, the index $\mu = 0, 1, 2,$ or 3 for the Dirac gamma matrices, γ^μ, and the same for the vector boson fields, W_μ and Z_μ. The coupling constant, denoted as g, appears in both the CC and NC Lagrangians and the Weinberg angle, θ_W, appears only in the NC Lagrangian. The NC Lagrangian also contains coupling coefficients $g_L^\ell = -\frac{1}{2} + \sin\theta_W$

and $g_R^\ell = \sin\theta_W$. These terms can be used to describe the simplest form of interaction between neutrinos and electrons, mainly, elastic scattering.

3.1.1 Elastic Scattering Cross Section

From the Lagrangians given by Eqs. 3.4 and 3.5, one can derive the differential cross sections for electron-neutrino elastic scattering off of electrons. The Feynman diagrams for the CC and NC elastic scattering interactions are shown in Fig. 3.1. The electron-neutrino scattering process is the primary interaction of interest in the case of solar neutrinos, hence it is necessary to calculate the probability of these events occuring inside the KamLAND detector.

To simplify the calculation, the effects of the W_μ and Z_μ fields (whose masses are of the order 100 GeV) can be neglected since we are dealing with low neutrino energies of the order 1 MeV. This means that the internal gauge boson lines in the Feynman diagrams can be contracted to a four-fermion vertex when computing the cross section. After employing the associated Feynman rules, the effective low-energy Lagrangian from the contribution of both the CC and NC processes is given by:

$$\begin{aligned}\mathscr{L}_{\text{eff}} = -\frac{G_{\text{F}}}{\sqrt{2}}\Big\{ &\left[\overline{\nu_e}\gamma^\mu(1-\gamma^5)e\right]\left[\overline{e}\gamma_\mu(1-\gamma^5)\nu_e\right] \\ &+ \left[\overline{\nu_e}\gamma^\mu(1-\gamma^5)\nu_e\right]\left[\overline{e}\gamma_\mu(g_V^\ell - g_A^\ell\gamma^5)e\right]\Big\}\end{aligned} \tag{3.6}$$

where the Fermi constant, G_{F}, is related to the W-boson mass (m_W) and the Z-boson mass (m_Z) through the fine structure constant, α, as follows:

$$\frac{G_{\text{F}}}{\sqrt{2}} = \frac{\pi\,\alpha}{2\sin^2\theta_W\, m_W^2} = \frac{\pi\,\alpha}{2\sin^2\theta_W\cos^2\theta_W\, m_Z^2} \tag{3.7}$$

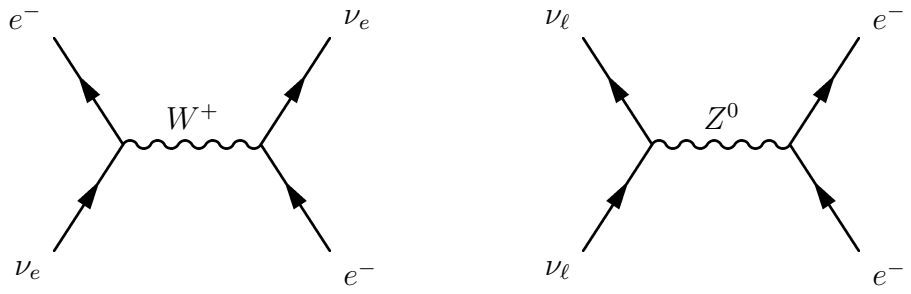

Figure 3.1: The Feynman tree-level diagrams for CC (on the left) and NC (on the right) neutrino-electron elastic scattering.

The last term in Eq. 3.6 is written with the vector and axial coupling coefficients, which are defined as $g_V^\ell = -\frac{1}{2} + 2\sin^2\theta_W$ and $g_A^\ell = -\frac{1}{2}$ in the case of the electron, muon, or tau (superscript $\ell = e, \mu, \text{or } \tau$).

The details of the cross section calculation can be found in texts such as Ref. [32] or Ref. [38]. In the laboratory frame, the neutrino electron scattering cross section can be written in terms of the electron recoil energy, T_e, as:

$$\frac{d\sigma}{dT_e} = \frac{2G_F^2 m_e}{\pi}\left[g_L^2 + g_R^2\left(1 - \frac{T_e}{E_\nu}\right) + g_L g_R \frac{m_e T_e}{E_\nu}\right] \tag{3.8}$$

where E_ν is the incident neutrino energy, $g_L = \pm 1/2 + \sin^2\theta_W$, and $g_R = \sin^2\theta_W$ ($+$ for ν_e and $-$ for $\nu_{\mu,\tau}$). The maximum kinetic energy of the recoil electron can be deduced from energy-momentum conservation to be:

$$T_e^{max}(E_\nu) = \frac{2E_\nu^2}{m_e + 2E_\nu}. \tag{3.9}$$

The neutrino electron scattering cross section is used in determining the interaction rate of neutrinos inside the KamLAND detector explained in Sec. 3.4.

3.1.2 Radiative Corrections and Magnetic Moment

There are small uncertainties associated with calculating the neutrino-electron scattering cross section due to higher-order contributions, which involve one-loop diagrams in addition to the tree-level diagrams shown in Fig. 3.1. Higher-order contributions to the cross-section are known as radiative corrections. The calculation of these corrections is quite involved and details can be found in the appendices of Ref.[39]. The uncertainty that arises in the spectral shape from these corrections is of the order of 4% for neutrinos at higher energies above 5 MeV. For ^{7}Be neutrinos the uncertainty in the overall spectral shape is about 1%. A precision measurement of solar neutrino rates should include these corrections in the calculation of the cross section. If the spectrum is measured accurately enough, the result could provide a direct test of standard electroweak theory that doesn't depend on solar models.

A minimal extension of the Standard Model (with massive neutrinos) yields a neutrino magnetic dipole moment through one-loop radiative corrections as discussed in Ref. [40] given as:

$$\mu_\nu = \frac{3eG_F m_\nu}{8\pi^2\sqrt{2}} = \frac{3G_F m_e m_\nu}{4\pi^2\sqrt{2}}\mu_B \sim 3\times 10^{-19}\mu_B\left[\frac{m_\nu}{1\text{ eV}}\right] \tag{3.10}$$

where μ_B is the Bohr magneton ($= e/2m_e$). This addition of a magnetic moment causes an extra term to be added to the cross section shown in Eq. 3.8. The extra contribution due to the magnetic moment term is given by:

$$\left(\frac{d\sigma}{dT_e}\right)_\mu = \frac{\pi\alpha^2\mu_\nu^2}{m_e^2}\left[\frac{1}{T_e} - \frac{1}{E_\nu}\right]. \tag{3.11}$$

This effect becomes larger for lower energy neutrinos and can only be directly tested

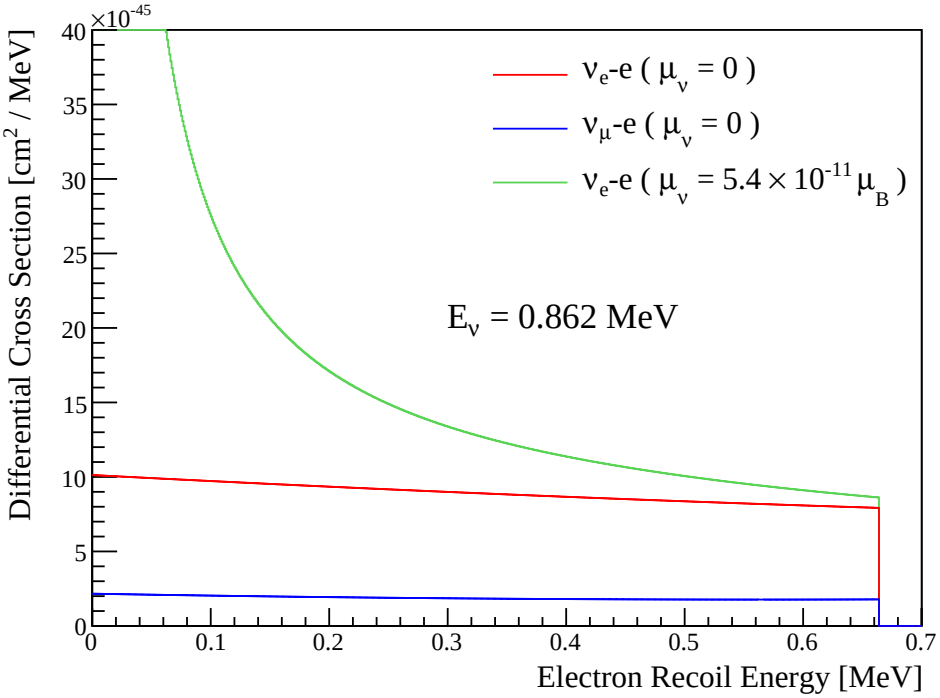

Figure 3.2: A comparison of the differential cross-section calculations for a neutrino energy of 0.862 MeV. The neutrino magnetic moment term can be seen to have clear $1/E_\nu$ dependence.

by elastic scattering experiments. Fig. 3.2 shows a comparison of differential cross sections calculated for a neutrino energy of 0.862 MeV. The $1/E_\nu$ dependence of the magnetic moment term is clearly visible and provides a key feature to use during spectral analysis. The newest limit on the neutrino magnetic moment was set by Borexino to be $\mu_\nu < 5.4 \times 10^{-11}\mu_B$ at a 90% C.L. [41]. There exist Grand Unified Theories which give rise to neutrino magnetic moments on the order of $10^{-15}\mu_B$ [42], and future measurements could test these models.

3.2 Neutrino Oscillations in Vacuum

Neutrino oscillations play an important role in understanding the predicted flux in any experiment detecting neutrinos with any degree of accuracy. This concept was first proposed by Bruno Pontecorvo in the late 1950s when looking for a lepton phenomenon analagous to $\bar{K} \rightarrow \bar{K}^0$ oscillations [43]. The first model to consider neutrino flavor oscillations was later postulated by Maki, Nakagawa, Sakata [44] and was used by Pontecorvo to predict the Solar Neutrino problem.

In the Standard Model neutrinos are produced and interact in definite flavor eigenstates. During this process the mass eigenstates are produced in superposition and don't necessarily correspond to the flavor eigenstates. As a consequence, the mass eigenstates are what propagate in time. In order to derive the oscillation probability, only "active" flavors of neutrinos are considered, however, neutrino flavors which do not participate in weak interactions ("sterile") can always be added to the basis state in an n-dimensional generalization.

A neutrino of flavor state ℓ ($= e,\ \mu,\ \tau$) can be described by a superposition of mass eigenstates in the following form:

$$|\nu_\ell\rangle = \sum_k U^*_{\ell k} |\nu_k\rangle \ \ (k = 1, 2, 3) \tag{3.12}$$

where the $U_{\ell k}$ is the unitary mixing matrix. For three-neutrino flavor oscillations this matrix is given by:

$$U_{\ell k} = \begin{pmatrix} \cos\theta_{12} & \sin\theta_{12} & 0 \\ -\sin\theta_{12} & \cos\theta_{12} & 0 \\ 0 & 0 & 1 \end{pmatrix} \begin{pmatrix} 1 & 0 & 0 \\ 0 & \cos\theta_{23} & \sin\theta_{23} \\ 0 & -\sin\theta_{23} & \cos\theta_{23} \end{pmatrix}$$
$$\times \begin{pmatrix} \cos\theta_{13} & 0 & \sin\theta_{13}e^{-i\delta} \\ 0 & 1 & 0 \\ -\sin\theta_{13}e^{-i\delta} & 0 & \cos\theta_{13} \end{pmatrix} \begin{pmatrix} e^{-i\xi_1} & 0 & 0 \\ 0 & e^{-i\xi_2} & 0 \\ 0 & 0 & 1 \end{pmatrix} \tag{3.13}$$

where the θ_{kj} are the mixing angles and δ is an arbitrary CP-violating phase. The last 3×3 matrix contains phases, ξ_1 and ξ_2, in the case where neutrinos are Majorana particles. The Majorana phase component drops out when performing the inner product, so it is not necessarily an important aspect of neutrino oscillation experiments.

The time dependence of neutrino oscillations can be modeled with the assumption that spin does not play a factor. Additionally, one can assume the massive neutrino states evolve in time as plane waves making them solutions of the Schrödinger equation:

$$|\nu_k(t)\rangle = \sum_k U^*_{\ell k} e^{-iE_k t}|\nu_k\rangle, \quad E_k = \sqrt{p_k^2 + m_k^2} \tag{3.14}$$

where E_k are the energy eigenvalues for neutrino momentum p_k and mass m_k. Since neutrinos are ultra-relativistic particles and the neutrino masses are much smaller than their momentum ($m_k \ll |\vec{p}\,|$), an approximation can be used for the energy-momentum relation:

$$E_k \simeq p_k + \frac{m_k^2}{2p_k} \approx E + \frac{m_k^2}{2E}. \tag{3.15}$$

The indice k disappears in this approximation since it is assumed that neutrinos with the same momentum propagate in the same direction ($p_k = p \approx E$). This relation is particularly useful when calculating the *transition probability* of a neutrino changing from flavor α to flavor β. The transition probability, $P(\alpha \to \beta)$, can be calculated using Eq. 3.14 like so:

$$P(\ell \to \ell') = |\langle \nu_{\ell'} | \nu_\ell \rangle|^2 = \sum_{k,j} U^*_{\ell k} U_{\ell' k} U_{\ell j} U^*_{\ell' j}\, e^{-i(E_k - E_j)t}. \tag{3.16}$$

For oscillation experiments like KamLAND the propagation time is not a measured quantity. Instead it is the distance, L, between the source and the detector that is known, and the ultra-relativistic approximation $t \simeq L$ can be used. The approximation in Eq. 3.15 can be used to rewrite the difference in the exponential as:

$$E_k - E_j = \frac{\Delta m^2_{kj}}{2E}, \qquad \text{where } \Delta m^2_{kj} \equiv m_k^2 - m_j^2. \tag{3.17}$$

The transition probability can be written in a form that is more illuminating when the terms in the sum are grouped as follows:

$$\begin{aligned} P(\ell \to \ell') &= \sum_k |U_{\ell k}|^2 |U_{\ell' k}|^2 + \\ &\quad \sum_{k>j} \left[U^*_{\ell k} U_{\ell' k} U_{\ell j} U^*_{\ell' j} e^{-i\Delta m^2_{kj} L/2E} + \left(U^*_{\ell k} U_{\ell' k} U_{\ell j} U^*_{\ell' j} e^{-i\Delta m^2_{kj} L/2E} \right)^* \right] \\ &= \sum_k |U_{\ell k}|^2 |U_{\ell' k}|^2 + 2 \sum_{k>j} \mathrm{Re} \left[U^*_{\ell k} U_{\ell' k} U_{\ell j} U^*_{\ell' j} e^{-i\Delta m^2_{kj} L/2E} \right]. \end{aligned} \tag{3.18}$$

This equation can be broken down further by using the complex relations: $\mathrm{Re}(A \cdot B)$ $= \mathrm{Re}(A) \cdot \mathrm{Re}(B) - \mathrm{Im}(A) \cdot \mathrm{Im}(B)$, $\mathrm{Re}(e^{i\theta}) = \cos\theta$, and $\mathrm{Im}(e^{i\theta}) = \sin\theta$. Using these relations and the trigonometric identity, $\cos 2\theta = 1 - 2\sin^2\theta$, the equation can be written as:

$$\begin{aligned} P(\ell \to \ell') = & \sum_k |U_{\ell k}|^2 |U_{\ell' k}|^2 + 2 \sum_{k>j} \mathrm{Re}\left[U^*_{\ell k} U_{\ell' k} U_{\ell j} U^*_{\ell j}\right] \\ & - 4 \sum_{k>j} \mathrm{Re}\left[U^*_{\ell k} U_{\ell' k} U_{\ell j} U^*_{\ell' j}\right] \sin^2 \frac{\Delta m^2_{kj} L}{4E} \\ & + 2 \sum_{k>j} \mathrm{Im}\left[U^*_{\ell k} U_{\ell' k} U_{\ell j} U^*_{\ell' j}\right] \sin \frac{\Delta m^2_{kj}}{2E}. \end{aligned} \tag{3.19}$$

The first two terms contain no oscillation phase and are equivalent to evaluating the transition probability at $L = 0$. Using this knowledge and the unitary condition for the mixing matrices, the following relation can be obtained:

$$\sum_k |U_{\ell k}|^2 |U_{\ell' k}|^2 = \delta_{\ell\ell'} - 2 \sum_{k>j} \mathrm{Re}\left[U^*_{\ell k} U_{\ell' k} U_{\ell j} U^*_{\ell' j}\right]. \tag{3.20}$$

The transition probability can now be written as:

$$\begin{aligned} P(\ell \to \ell') = & \delta_{\ell\ell'} - 4 \sum_{k>j} \mathrm{Re}\left[U^*_{\ell k} U_{\ell' k} U_{\ell j} U^*_{\ell' j}\right] \sin^2 \frac{\Delta m^2_{kj} L}{4E} \\ & + 2 \sum_{k>j} \mathrm{Im}\left[U^*_{\ell k} U_{\ell' k} U_{\ell j} U^*_{\ell' j}\right] \sin \frac{\Delta m^2_{kj} L}{2E}. \end{aligned} \tag{3.21}$$

The derivation of the transition probability is practically identical for anti-neutrinos and the result is the same with the exception of a change in sign for the imaginary

term.

In order to make this relevant for solar neutrino experiments, the quantity of concern is the transition probability for the electron neutrino. This probability is given approximately by:

$$P(e \to \ell') \simeq 1 - \sin^4\theta_{13} - \cos^4\theta_{13} \left[1 - \sin^2 2\theta_{12} \sin^2 \left(\frac{1.27\ \Delta m^2_{21}[\mathrm{eV}^2]\ \mathrm{L[m]}}{\mathrm{E[MeV]}}\right)\right] \quad (3.22)$$

where the factor of 1.27 in the oscillation phase comes from accounting for the specified dimensions. Other transition probability terms can be found in Ref. [45].

The transition probability in Eq. 3.22 can be simplified further since θ_{13} is small [19] [46]. This gives the expression:

$$P(e \to \ell') \simeq \sin^2 2\theta_{12} \sin^2 \left(\frac{1.27\ \Delta m^2_{21}[\mathrm{eV}^2]\ \mathrm{L[m]}}{\mathrm{E[MeV]}}\right). \quad (3.23)$$

This simplified version of the transition probability in a two-neutrino form can be used to calculate the *survival probability* of an electron neutrino staying in its flavor state:

$$P(e \to e) = 1 - P(e \to \ell') = 1 - \sin^2 2\theta_{12} \sin^2 \left(\frac{1.27\ \Delta m^2_{12}[\mathrm{eV}^2]\ \mathrm{L[m]}}{\mathrm{E[MeV]}}\right). \quad (3.24)$$

These probabilities can be used by experiments to measure the neutrino oscillation parameters. The survival probability is typically utilized in reactor experiments like KamLAND, which yielded $\Delta m^2_{21} = 7.59^{+0.21}_{-0.21} \times 10^{-5}$ eV^2 and $\tan^2\theta_{12} = 0.47^{+0.06}_{-0.05}$ from a combined analysis with data from solar neutrino experiments measuring the survival probability [18]. However, neutrinos coming from the Sun need to traverse a distance

of 1.5×10^8 km. When compared to the average distance between oscillation maxima of about 65 km for a 1 MeV neutrino, the oscillation phase is averaged out. This would give a reduction of about 1/2 in the number of electron neutrinos that survive the trip from the Sun to the Earth, but it doesn't explain the famous deficit of 2/3 seen by solar neutrino experiments. In order to calculate the expected number of neutrinos coming from the Sun, matter induced flavor change needs to be taken into account.

3.3 Neutrino Oscillations in Matter

The possibility of neutrino flavor change caused by matter interactions was proposed by Wolfenstein [16]. At low energies only coherent forward scattering is relevant. Since the electron neutrino is the only flavor that undergoes charged-current elastic scattering, it will feel a different potential than muon or tau neutrinos. An effective potential for this difference is usually written as:

$$V_{\text{eff}} = \sqrt{2} G_F n_e \tag{3.25}$$

where G_F is the Fermi coupling constant and n_e is the electron number density of the medium. This potential changes the Hamiltonian of the system, but the neutrino propagation still maintains an analagous form compared to the vacuum case. The propagation equation for a two-flavor mixing of neutrinos in matter can be written as:

$$-i\frac{d}{dt}\begin{pmatrix}\nu_e \\ \\ \nu_\mu\end{pmatrix} = \frac{M^2}{2E}\begin{pmatrix}\nu_e \\ \\ \nu_\mu\end{pmatrix}, \quad M^2 = \left[U \begin{pmatrix} m_1^2 & 0 \\ \\ 0 & m_2^2 \end{pmatrix} U^\dagger + \begin{pmatrix} A & 0 \\ \\ 0 & 0 \end{pmatrix}\right] \tag{3.26}$$

where U is the two-dimensional unitary mixing matrix and $A = 2\sqrt{2}G_F n_e E$. With some further algebra, the propagation can be written as:

$$-i\frac{d}{dt}\begin{pmatrix}\nu_e\\ \\ \nu_\mu\end{pmatrix} = \frac{1}{4E}\begin{pmatrix}A - \Delta m^2_{21}\cos 2\theta_{12} & \Delta m^2_{21}\sin 2\theta_{12}\\ \\ \Delta m^2_{21}\sin 2\theta_{12} & -A + \Delta m^2_{21}\cos 2\theta_{12}\end{pmatrix}\begin{pmatrix}\nu_e\\ \\ \nu_\mu\end{pmatrix} \tag{3.27}$$

Derivations of the solution to this equation can be found in the literature [32], [47]. Special cases for slowly varying density (adiabatic) and rapidly varying density are usually considered.

3.3.1 The MSW Effect

For the case of slowly varying density, the unitary mixing matrix takes on a very simple form. The mixing angles are defined differently from the vacuum case (with the subscript M) to denote the effect of the matter potential. This matrix can be written as:

$$U_M = \begin{pmatrix}\cos\theta_M & \sin\theta_M\\ \\ -\sin\theta_M & \cos\theta_M\end{pmatrix}. \tag{3.28}$$

This mixing matrix provides relations for the resulting mixing angle in matter given by:

$$\tan 2\theta_M = \frac{\tan 2\theta_{12}}{1 - \dfrac{A}{\Delta m^2_{21}\cos 2\theta_{12}}} \tag{3.29}$$

and the mass-squared difference in matter by:

$$\Delta m^2_M = \sqrt{(\Delta m^2_{21}\ \cos 2\theta_{12} - A)^2 + (\Delta m^2_{21}\ \sin 2\theta_{12})^2}. \tag{3.30}$$

An interesting phenomenon was discovered in these relations by Mikheev and Smirnov in 1985 [48]. When considering a matter potential of $A = \Delta m^2_{21}\ \cos 2\theta_{12}$, there is a resonance which causes the mixing angle to become maximal. Conversly, the mass splitting becomes minimal at the resonance. This is known as the *MSW effect*. Calculating this effect for neutrinos propagating through varying density profiles is a little more complicated, and approximations are sometimes used. It should be noted that Eqs. 3.29 and 3.30 only consider a two-flavor scenario. The three-flavor solutions are derived in [32], but can also be obtained by a simple substitution: $A \rightarrow A\ \cos\theta_{13}$. Given that $A \sim 10^{-5}$ eV^2 in the core for a neutrino energy of 0.862 MeV and assuming $\sin^2 2\theta_{13} = 0.086$ [46], an overall effect of less than 1% is expected for $\tan 2\theta_M$ in the three-flavor mixing case.

3.3.2 MSW Effect for Solar Neutrinos

Analytical calculations of matter effects for slowly varying densities in the Sun were presented by Parke in 1986 [49] [50]. These calculations uses the approximation that the density varies linearly in the region of the Sun where matter oscillations are important. The survival probability for an electron neutrino in a density region larger than the resonance density is given by:

$$P_{\mathrm{MSW}}(e \rightarrow e) = \frac{1}{2} + \left(\frac{1}{2} - P_{\mathrm{jump}}\right)\ \cos 2\theta_M\ \cos 2\theta_{12} \tag{3.31}$$

where P_{jump} is the probability of jumping from one adiabatic mass eigenstate to

another. This can be calculated by applying the result from Landau and Zener in 1932 [51], which describes the level crossing of a two-level quantum system given the departure from a smooth adiabatic evolution. The term P_{jump} is given by:

$$P_{\text{jump}} = \exp\left[\frac{-\pi\Delta m^2_{21}\,\sin^2 2\theta_{12}}{4E\,\cos 2\theta_{12}}\left(\frac{n_e}{|dn_e/dr|}\right)\right], \quad n_e > \frac{\Delta m^2_{21}\,\cos 2\theta_{12}}{2\sqrt{2}EG_F}. \tag{3.32}$$

This approximation is accurate given that the density varies linearly, the mixing angles are large and Δm^2_{21} is small. It should be noted, however, that the adiabatic approximation is a rather good assumption meaning that $P_{jump} \approx 0$ and could very well be neglected. The Parke formula is used to calculate the transition probability when predicting the solar neutrino spectra for KamLAND. A plot showing the transition probability obtained from the Parke formula for ^{7}Be, pep, and ^{8}B neutrinos is shown in Fig. 3.3. The pep neutrinos are ideal for an experimental determination of the MSW transition probability, since they have an energy which lies directly in the middle of the crossover region. Experiments which measure ^{8}B neutrinos see the largest flux deficit. A formulation of the expected solar neutrino spectra after accounting for matter oscillations is essential for spectroscopic measurements.

3.4 Calculation of Solar Neutrino Spectra

When it comes to experiments measuring solar neutrinos, it is necessary to accurately calculate neutrino propagation in the Sun taking into account the MSW effect presented in the previous section. These effects are taken into account when calculating the spectrum averaged differential cross-section, which is the most useful quantity for experiments. This differential cross-section can be calculated using Eq. 3.8 and is given by:

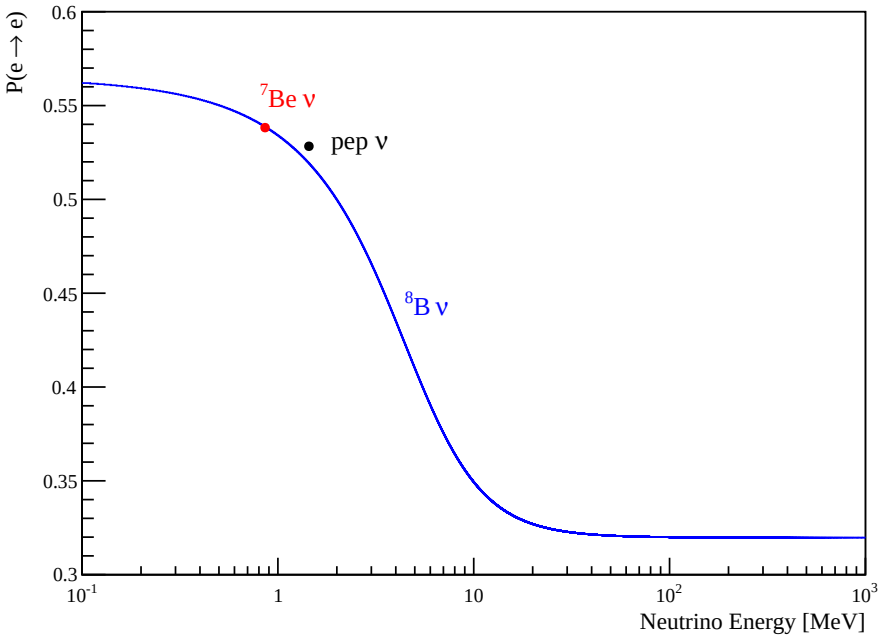

Figure 3.3: The survival probability as a function of solar neutrino energy for ^{7}Be, pep, and ^{8}B neutrino types. The MSW effect is very clear at neutrino energies greater than 5 MeV, where the transition occurs. These calculations were made using $\Delta m^2_{21} = 7.59 \times 10^{-5}$ eV^2 and $\tan^2\theta_{12} = 0.47$.

$$\left\langle \frac{d\sigma}{dT} \right\rangle = \int_{E_{min}}^{E_{max}} dE\ S(E)\ \frac{d\sigma}{dT} \tag{3.33}$$

Here, $S(E)$ is the neutrino energy spectrum shown in Fig. 2.5. The upper integration limit is the endpoint of the neutrino production energy. The lower integration limit, E_{min}, is the minimum energy at which an electron recoil is produced with energy T. This is given by:

$$E_{min} = \frac{T + \sqrt{T(T + 2m_e)}}{2}. \tag{3.34}$$

As described in the previous section, matter oscillations need to be included into this calculation of the cross section. In order to account for matter oscillations correctly,

the electron density as a function of solar radius taken from Bahcall [35] is combined with the neutrino production as a function of solar radius from Fig. 2.6. These two quantities are used to calculate the solar neutrino survival probability given by:

$$P(e \rightarrow e) = \int dr\ \Phi_\nu(r)\ \int dE \left\{ \frac{1}{2} + \left(\frac{1}{2} - P_{\text{jump}} \right) \cos 2\theta_M\ \cos 2\theta_{12} \right\} S(E) \quad (3.35)$$

where Φ_ν is the fraction of neutrino produced at solar radius r. In order to account for neutrinos that undergo a transition from electron flavor, the probability can be rewritten as $1 - P(e \rightarrow e)$. Both of these probabilities can be included into the differential cross-section as:

$$\left\langle \frac{d\sigma}{dT} \right\rangle = \int_{E_{min}}^{E_{max}} dE \left\{ P(e \rightarrow e) \left(\frac{d\sigma}{dT} \right)^{\text{CC}} + (1 - P(e \rightarrow e)) \left(\frac{d\sigma}{dT} \right)^{\text{NC}} \right\}. \quad (3.36)$$

where both the CC cross-section for electron neutrinos and the NC cross-section for muon and tau neutrinos are accounted for.

The diffferential cross-section in Eq. 3.36 is used to calculate the total interaction rate in KamLAND by multiplying by the number of target electrons in the detector. In this manner, the number of electron recoils per recoil energy are calculated in 1 keV bins as:

$$\frac{dN}{dT} = \left\langle \frac{d\sigma}{dT} \right\rangle N_e N_\nu \quad (3.37)$$

where N_e is the number of target electrons and N_ν is the total neutrino flux for a

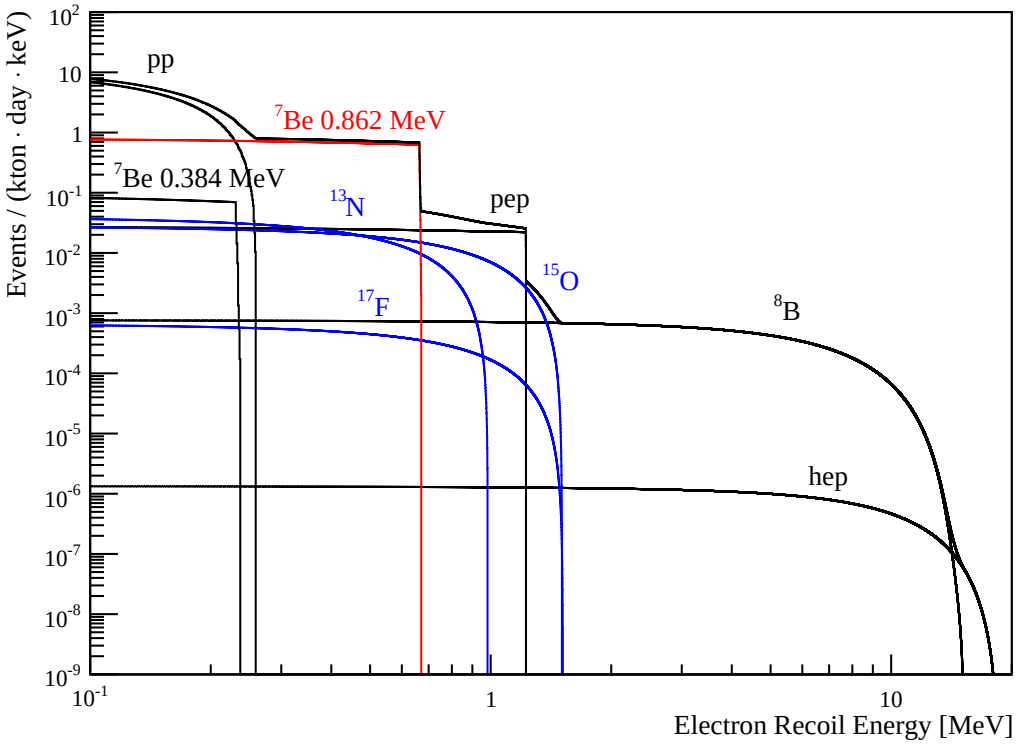

Figure 3.4: The neutrino-electron scattering recoil spectra in KamLAND with matter oscillations assuming $\Delta m^2_{21} = 7.59 \times 10^{-5}$ eV^2 and $\tan^2\theta_{12} = 0.47$. Energy resolution and quenching have not been included in the calculation.

certain branch given by the SSM. The number of recoils per energy bin is calculated up to the maximum kinetic energy given by Eq. 3.9. The output of this calculation is plotted for all neutrino branches in Fig. 3.4. This calculation doesn't account for detector effects such as energy resolution and quenching. The ^{7}Be solar neutrino spectrum obtained from this calculation is used to generate a spectral fitting function in order to extract the signal from the data.

A software package, called KNuSolar, was developed specifically for the purpose of calculating the solar neutrino spectra as described above. KNuSolar is a stand-alone software written in C++ and can be used for any future solar neutrino experiments designed for $\nu - e$ elastic scattering detection. The authors, Greg Keefer and Lindley Winslow, are credited for this work.

Chapter 4

An Overview of the Experiment

The KamLAND (**Kam**ioka **L**iquid scintillator **A**nti-**N**eutrino **D**etector) experiment is located inside of the Kamioka Mine beneath Mt. Ikenoyama (36.42°N, 137.31°E), in the Gifu Prefecture of Japan. It is housed inside the old cavity of the Kamiokande experiment with an overburden of about one kilometer of rock (equivalent to 2,700 of water). The overburden provides a natural shield for cosmic-ray muons, decreasing the muon rate by a factor of 10^5 (relative to a detector located on the surface) to about 0.3 Hz. The detection medium consists of one kiloton of liquid scintillator (LS), which fluoresces when particles interact with and, in the process, excite the molecules of the liquid. The light emitted due to particle interactions in the LS is collected by photomultiplier tubes (PMTs) allowing reconstruction of position, time and energy of physics events. A diagram of the experimental facility is shown in Fig. 4.1.

4.1 Detector Description

The detector can be divided into two major components: the Inner Detector (ID) and the Outer Detector (OD). The ID houses the most important part the of the detector, mainly, the LS and buffer oil (BO) regions. The one kiloton of LS is

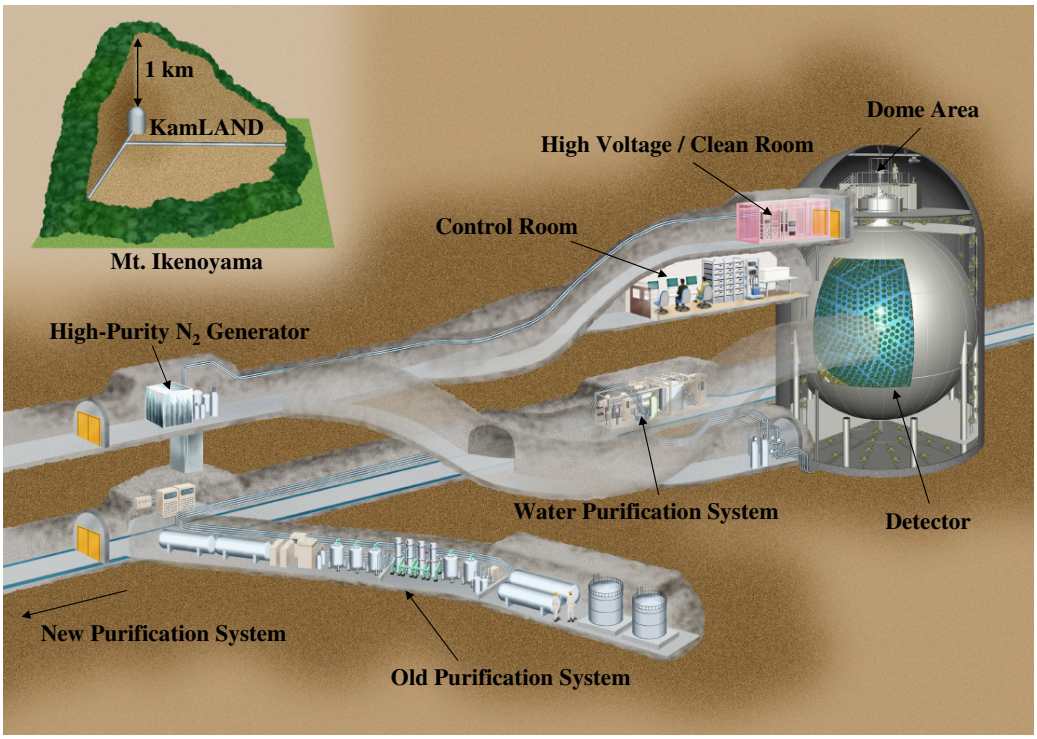

Figure 4.1: A diagram of the KamLAND experimental site.

contained inside a transparent balloon made out of a layered combination of nylon and Ethylene Vinyl Alcohol (EVOH). The balloon is 13 m in diameter and has a total thickness of 135 μm giving it good durability and high impermeability to ^{222}Rn. The balloon is supported by a series of vertical and horizontal Kevlar ropes woven together to help provide stability and keep the balloon's spherical shape. The tension of the vertical Kevlar ropes is constantly monitored for safety and also provides an estimate of the total weight of the LS inside the balloon via readout of load cells.

Surrounding the balloon is a 1.4 kton BO region, 2.3 m in thickness. The BO is a mix of 53% n-Dodecane and 47% iosparaffin. This region provides bouyancy for the balloon and helps to shield the LS volume from external gamma-rays coming from the outer regions and components of the detector. Surrounding the BO region

is an acrylic shell with a thickness of 3 mm. The acrylic has an index of refraction relatively close to the oil and further reduces the transport of ^{222}Rn into the LS by impeding liquid convection in the BO. The acrylic shell is 16.6 meters in diameter. The outermost boundary of the ID is an 18 m diameter, stainless steel sphere which acts as a containment vessel for the inner region of the detector. A total of $1,879$ PMTs are attached to the inside of the stainless steel sphere and are encompassed by the acrylic shell. The region between the acrylic shell and stainless steel sphere is also filled with buffer oil, optically coupling the PMTs to the acrylic and providing a heat sink for the PMTs.

The OD surrounds the stainless steel sphere of the ID, and is composed of 3.4 kton of purified water inside a cylindrical cavern. The OD has four separate regions, lined with tyvek, containing 225 PMTs that allow the OD to operate as a Čerenkov detector. The tyvek has high reflectivity and improves light collection in the OD regions. The OD is utilized for its ability to absorb and tag cosmic rays and other high energy events coming from the surrounding rock, which can be removed from the data later on during analysis. The OD is surrounded by a set of compensating coils which reduce the magnitude of the Earth's magnetic field to less than 50 mG. A reduced magnetic field helps to keep the electron trajectory inside the PMTs from being perturbed, and hence, improves PMT sensitivity. A labeled diagram of the detector can be seen in Fig. 4.2.

4.2 Liquid Scintillator

The LS is a mixture of organic liquids and acts as the target volume for neutrinos and anti-neutrinos. It is composed of 80.2% n-Dodecane, 19.8% 1,2,4-Trimethylbenzene (also called Pseudocumene or PC), and 1.36 g/l of 2,5-Diphenyloxazole (PPO). The chemical compositions of each component are shown in Fig. 4.3.

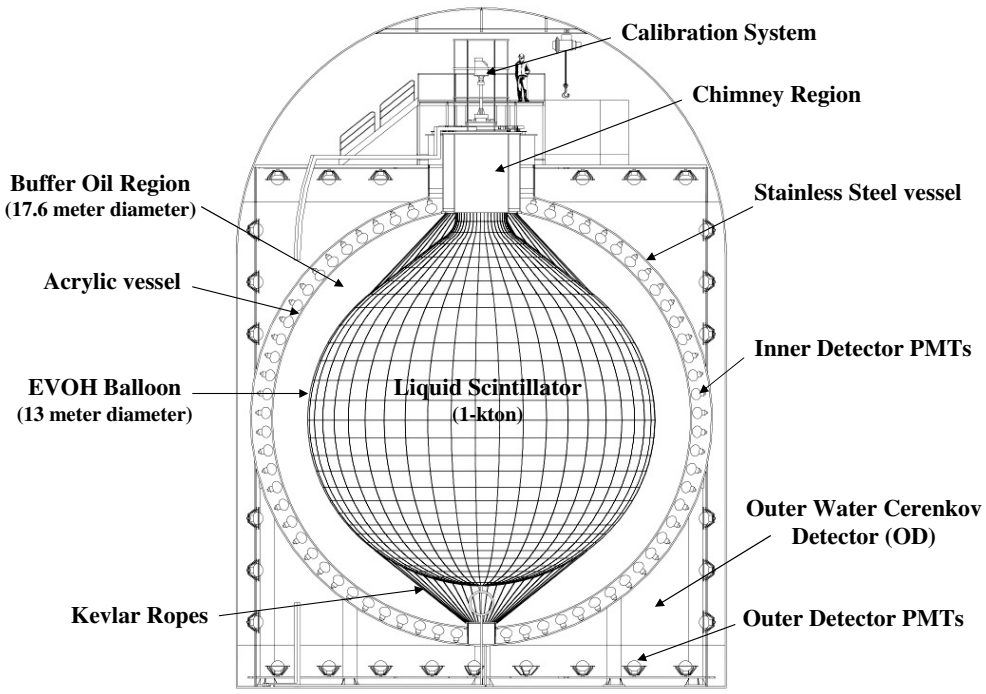

Figure 4.2: A diagram of the detector.

The PC is the primary scintillator and emits light through molecular excitation as propagating particles deposit their energy in the liquid. The light emitted by the PC, however, is not in an optimal wavelength range for detection by the PMTs. The PPO is a fluor which is dissolved into the PC in order to absorb the initial molecular excitation energy and re-emit it as light at longer wavelengths in the visible region. This key feature also makes the LS transparent to its own light. The concentration of the PPO is such that it provides sufficient light output while keeping the cost reasonable.

The Dodecane acts as a diluter for the LS. It was chosen to provide chemical stability, increase the light transparency and keep the flashpoint of the LS above 70°C. The chemical properties of the scintillator components are listed in Table 4.1.

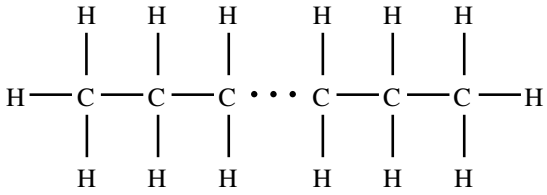

n-Dodecane – $C_{12}H_{26}$

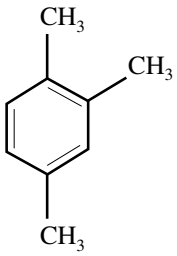

1,2,4 – Trimethylbenzene
(Pseudocumene) – C_9H_{12}

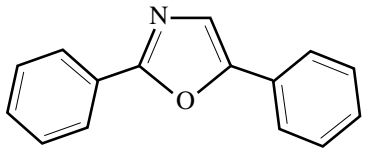

2,5 – Diphenyloxazole
(PPO) – $C_{15}H_{11}NO$

Figure 4.3: Chemical composition of individual LS components.

Property	n-Dodecane	Pseudocumene	PPO
Density [g/cm^3] @ 20°C	0.7495	0.8758	1.0940
Boiling Point [°C] @ 1 atm	216	169	360
Melting Point [°C] @ 1 atm	-9.6	-44	74
Flash Point [°C]	74	46	-

Table 4.1: Common chemical characteristics of the LS components. The densities, boiling points and melting points are referenced from [52]. The flash points are referenced from [53].

4.3 Photomultiplier Tubes

When considering a solar neutrino measurement, the relevant signals are in the sub MeV region. For the inner detector, a typical event of 1 MeV visible energy corresponds to about 200 photo-electrons (p.e.) when taking into account the quantum efficiency of the PMTs. This means that most PMTs will produce, at most, a single p.e. on the photocathode. The PMTs in KamLAND have very large photocathodes providing good sensitivity to single p.e. signals. When a p.e. is produced on the photocathode, it is focused using an electric field onto a system of dynodes. These dynodes amplify a signal produced by a single p.e. to a read-out pulse on the order of 1 mV. In addition to single p.e. sensitivity, the PMTs also have good timing resolution allowing separation of multiple signals which occur in time.

The ID is outfitted with two types of PMTs. There are 554 20-inch PMTs having Venitian blind type dynodes, which were salvaged from the original Kamiokande experiment. In addition to the 20-inch PMTs, there are also 1,325 17-inch PMTs. The 225 OD PMTs are the 20-inch model. The 17-inch PMTs have a physical diameter of 20 inches but are masked to 17-inches in diameter. They also have a linear-focused type dynode which improves timing resolution and provides faster response. The quantum efficiency in the dominant wavelength region of KamLAND LS emission is about 20%. A plot of the PMT quantum efficiency overlaid with the PPO emission probability can be seen in Fig. 4.4. The total photocathode coverage on the inner detector is about 22% for the 17-inch PMTs and about 34% when taking into account both 17-inch and 20-inch PMTs.

The chimney region of the detector has 6 5-inch PMTs mounted at the top of the neck, aiming down into the LS. There are also 16 8-inch PMTs distributed around the neck region. These PMTs help to improve the detection efficiency of muons passing through this region of the detector.

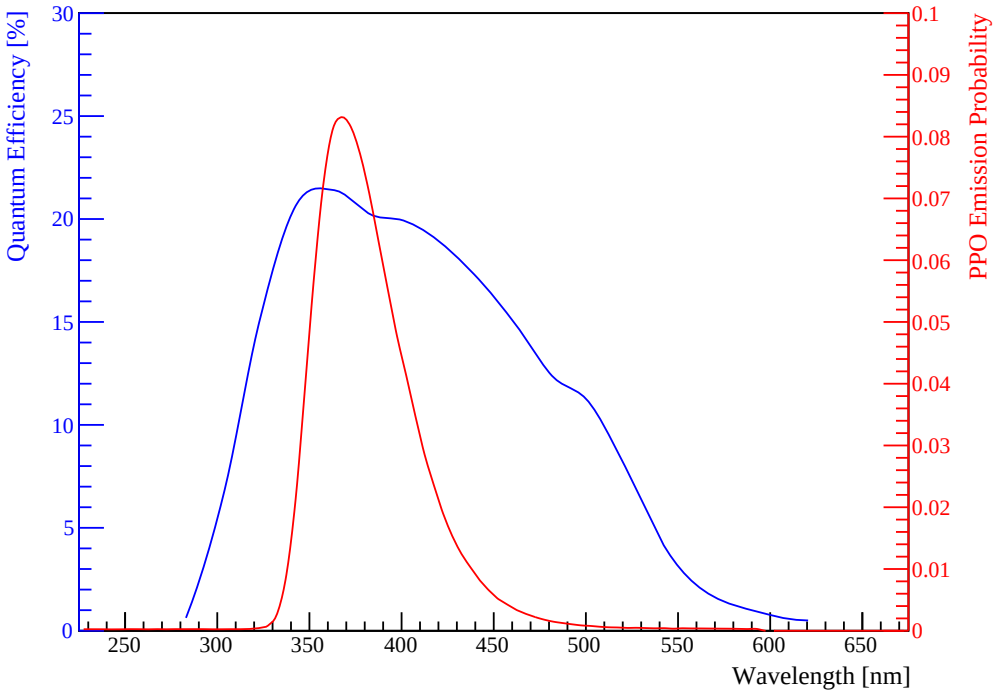

Figure 4.4: The 17-inch PMT quantum efficiency [54] (in blue) overlaid with the PPO emission probability [55] (in red).

4.4 Electronics and Data Acquisition

The charge pulses produced by the PMTs are sampled by a system called Front-End Electronics (FEE). A simple diagram of the FEE can be seen in Fig. 4.5. The system consists of a discriminator for each PMT set to a voltage threshold corresponding to a sensitivity of 0.15 p.e. If the pulse passes the discriminator, it is sent to a Field Programmable Gate Array (FPGA), where the hits from 12 PMTs are summed. The decision to digitize and capture the hits is made when the number of 17-inch PMTs over threshold (Nsum) exceeds a desired value within a 125 ns time window.

At the time the trigger decisions are being made, the pulse from each PMT is stored on a device called an Analog Transient Waveform Digitizer (ATWD). The

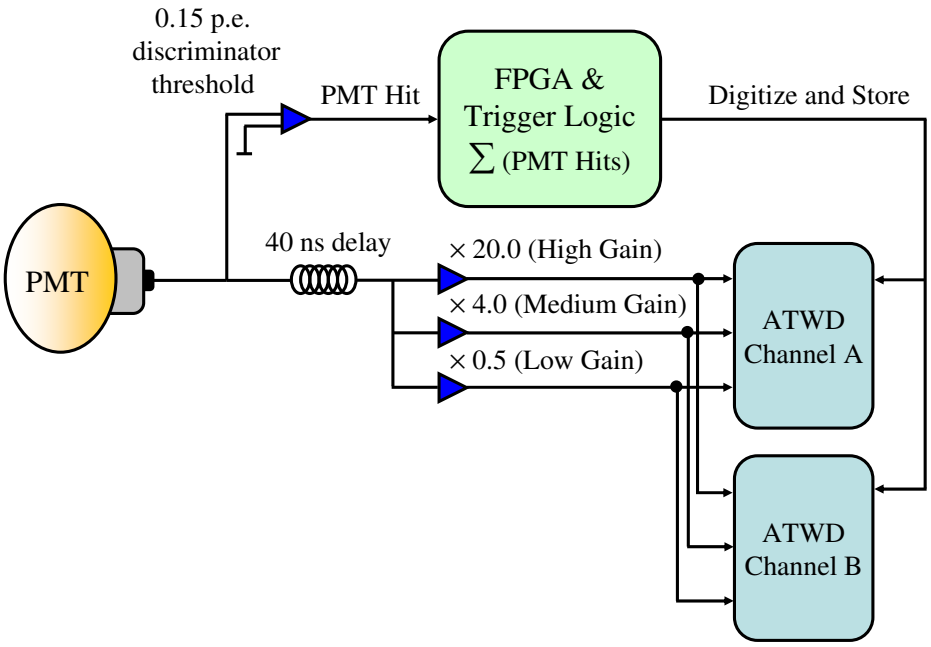

Figure 4.5: A simplified diagram of the KamLAND FEE.

ATWD acts as a tiny oscilloscope storing voltage information on an array of capacitors which digitize the waveforms on command. This waveform information is made up of 128, 10-bit samples having an interval rate of 1.6 ns per sample (for a total sampling time of about 200 ns). The sampling interval is calibrated using a 40 MHz clock signal which is connected to each ATWD. Each waveform takes almost 30 μs to digitize. In order to minimize the amount of dead time during the digitization of waveforms, each PMT channel is equipped with two identical ATWDs. Each channel also has three different gain settings connected in parallel: High gain ($\times$20), Medium gain ($\times$4), and Low gain ($\times$0.5). This allows for a high dynamic range during waveform collection, from very low energy events with about one p.e./PMT to very high energy cosmic rays producing thousands of p.e./PMT.

The FEE boards are contained inside of 10 W-Ie-Ne-R Series 6000 VME crates, each crate containing 20 data taking boards. The PMTs are connected to the boards

in a manner that allows each board to cover the full detector uniformly. All of the OD PMTs are housed in an independent VME crate. This designed mapping of PMT channels reduces any effects electronics problems might have on event reconstruction.

The software used for the handling of data acquistion is called KiNOKO, which was designed specifically for KamLAND. It is an object-oriented software package which has the responsibility of sending configuration scripts to the trigger and electronics, real-time monitoring of acquired data, and storing data in an efficient file format. KiNOKO provides a graphical user interface to allow the conditions of a data taking run to be changed, depending on the nature of the data taking (normal physics, background, calibrations, baseline, etc.).

4.5 Trigger System

The trigger system was developed as a decision engine that can send commands to initialize waveform acquisition. These decisions can be divided into two types of commands: global acquisition and forced acquisition. The global acquisition commands collect waveforms only from PMT channels which are above the discriminator threshold. The forced acquisition collects waveforms from all channels regardless of the whether or not the signal is above the discriminator threshold. A Global Positioning System (GPS) receiver sends the trigger system universal time information. The GPS receiver also synchronizes the 40 MHz clock and allows the trigger to provide timestamp information for each waveform. There are many different types of triggers that were developed for various circumstances during data taking. The most relevant triggers are listed below:

ID Triggers:

ID Singles Trigger - sends a global acquisition command when the ID Nsum

exceeds a user preset threshold.

ID Prompt Trigger - sends a global acquisition command when the ID Nsum exceeds a user preset threshold and additionally opens a 1 ms time window for an ID delayed trigger.

ID Delayed Trigger - sends a global acquisition command when the ID Nsum exceeds a user preset threshold within 1 ms of an ID prompt trigger.

ID Prescale Trigger - sends a global acquisition command when the ID Nsum exceeds a user preset threshold. The acquisition window is prescaled to a specified fraction of a second.

ID 5-inch PMT Trigger - sends a global acquisition command when the ID 5-inch PMT Nsum exceeds a user preset threshold.

ID History Trigger - sends a global acquisition command when the ID Nsum exceeds a user preset threshold, but only keeps track of the Nsum information inside of a 200 ns interval or until another global acquisition command is issued.

ID-to-OD Trigger - sends a global acquisition command to the OD FEE whenever any of the ID triggers are issued.

OD Triggers:

OD Top/Upper/Lower/Bottom Triggers - four different OD triggers, each sending a global acquisition command when the associated area of the OD exceeds a user preset threshold.

OD Top/Upper/Lower/Bottom History Triggers - four different OD history triggers, each sending a global acquisition command to track Nsum

information when the associated area of the OD exceeds a user preset threshold.

OD-to-ID Trigger - sends a global aqcuisition command to the ID FEE whenever any of the OD triggers are issued.

Other Triggers:

1PPS Trigger - sends a global acquisition command to the ID and OD FEE once every second and is synchronized with the GPS time.

GPS Trigger - issued at the beginning of each data taking run and every 32 seconds thereafter. It sends an interrupt command to the GPS VME module to capture the time.

Supernova Trigger - this trigger is issued when at least 8 events have an Nsum $\geq$ 1100 occur in 0.84 seconds, which are the estimated parameters for a supernova candidate. This trigger changes the entire detection mode to singles events only for 1 minute, and prevents anyone from changing the run conditions during this time. The users are notified of a possible supernove candidate.

In terms of a ^{7}Be solar neutrino measurement, the prompt, delay, and prescale triggers are most important. The prescale trigger was set to a threshold of 40 Nsum (with a time fraction of 0.01024) during solar data taking, which allows for the collection of events of energy 0.20 MeV with about 99% efficiency. The prompt and delay triggers provide significantly more detection live time than the prescale trigger, but they are both set to a higher threshold of Nsum 70 providing about 99% efficient collection of events with an energy of 0.35 MeV. The lower bound for the prompt

and delayed trigger thresholds are limited by the high event rates at low energies. The calculations of the trigger efficiencies are covered in greater detail in Chap. 5.7. The 1PPS trigger is also important when estimating the dark noise of the ID, as this trigger provides hit and waveform information that is completely uncorrelated with physics events.

4.6 Calibration Systems

To understand the detector response and data quality, several calibration systems have been utilized. The Z-Axis System was one of the earliest systems installed at the top of the detector in 2002. This system had the ability to lower calibration sources down the central axis of the detector to specified positions using a cable and pulley. The system was encompassed inside a glove box, which was purged with Nitrogen gas to prevent ^{222}Rn from leaking into the detector. The calibration sources consist of both lasers and sealed radioactive capsules which were attached to the end of the cable. The lasers were used to calibrate the PMT timing and understand light propagation in the detector. The sealed radioactive source capsules allow calibration of the energy scale and vertex reconstruction. The radioactive sources used in KamLAND are listed in Table 4.2.

A more complex system, called the 4π System, was installed in 2005 and 2011. This calibration system had the ability to position sources throughout the LS volume and provided a means to study the off-axis reconstruction of physics events in the detector. The system was composed of a pole suspended at the ends by two cables. By moving one of the two cables, the pole can be lowered and retracted, or can be extended to sweep through off-axis positions. This system was deployed just before the scintillator purification campaign began in 2006 to estimate the energy and vertex biases at off-axis points throughout the detector. A complete description

Isotope	Radiation	Energy
^{203}Hg*	γ	279 keV
^{7}Be*	γ	478 keV
^{85}Sr*	γ	514 keV
^{137}Cs*	γ	662 keV
^{68}Ge*	e^+	1,022 keV (annihilation γ's)
^{65}Zn	γ	1,115 keV
^{60}Co*	γ	2,502 keV
^{241}Am^{9}Be	n	4,439 keV (from excited ^{12}C γ)
^{210}Po^{13}C	n	6,130 keV (n capture γ)

Table 4.2: A list the radioactive calibration sources used in KamLAND. Sources marked with an asterisk (*) were used after the purification campaign.

of this system can be found in Ref. [56].

The most recent calibration system, installed in 2009, is called MiniCal. It was designed to be very compact and reduce as much as possible the exposure of the detector to ^{222}Rn. MiniCal works much like the Z-Axis System, lowering sources along the central axis via a cable and pulley system. All calibrations performed during the solar data taking were taken with the MiniCal system.

Chapter 5

Data Reconstruction

The KamLAND PMTs collect scintillation light from particle interactions in the form of charge pulses, also called waveforms. The waveforms are digitized and stored by the electronics for offline event reconstruction, and they provide both charge and arrival time information. This information is required to calculate the energy and position of the corresponding physics events inside the detector. An outline of the procedures and algorithms needed to classify events is given in this chapter, along with the necessary methods for calibrating event information. The reconstruction of physics events also requires certain quality checks in order to remove effects like electronic noise or disturbances caused by muons and other high energy cosmic-rays passing through the detector. Muon and cosmic-ray events have tracks of energy deposits in the detector unlike the point-like, low energy events which are the primary selection targets for solar neutrino analysis. The tagging and reconstruction of muon tracks is summarized, as the rejection of these events is essential for any low energy analysis. Two primary triggers, the prescale and prompt, are utilized in the data collection and a calculation of the event collection efficiency for these two triggers is presented.

5.1 Waveform Analysis

The reconstruction of data begins with waveform analysis, where the digitized waveforms for each PMT are converted to corresponding charge and time information. As mentioned in Sec. 4.4, the waveforms are sampled over an interval of approximately 200 ns. At the beginning of each run, 50 pedestal waveforms (corresponding to zero net charge), 50 test-pulser waveforms, and 50 clock waveforms are recorded and averaged. The average pedestal is subtracted from each waveform and any additional non-zero offset is subtracted so that the baseline is centered around zero. The time scale of the waveform is calibrated using the clock waveforms and the amplitude scale is calibrated with the test-pulsers.

The resulting waveforms are smoothed and an algorithm searches for the first photon peak by calculating the first and second derivatives. The leading edge of the first peak corresponds to the arrival time of the first photon. The waveform peaks are integrated and normalized by the mean charge of the 1 p.e. peak to calculate the total charge.

Extracted hit times are not always exactly equal to the pulse arrival times due to fluctuations in the PMT response and unequal cable lengths. Similarly, the extracted charge is not always equal to the number of p.e.'s due to fluctuations in the gains of the PMTs, FEE amplifiers, etc. Due to these variations, time and charge corrections are made on a channel-by-channel basis. Details on these corrections can be found in Ref. [57].

5.2 Bad Channel Selection

Not all of the waveform information collected by PMTs can be used in the reconstruction process, because a small number of the PMTs are unstable or noisy. In

order to avoid using these PMTs in the reconstruction, a list of selection criteria for bad PMT channels was made. The bad channels are flagged during every data taking run under the following conditions:

1. Less than 1,000 hits per 10^4 events.
2. More than 1,000 no-hits per 10^4 events.
3. Less than 80 hits per 100 high-charge muon events.
4. There is a hit-rate difference of more than 22% between the two ATWDs on a single channel per 10^5 events.
5. The number of ADC channels per 1 p.e. charge is not within 25% of the mean value for the 17-inch PMTs.
6. The charge deviation for high-charge muon events is greater than 400 p.e. between neighboring PMT channels.

These conditions are applied for the ID PMTs. When flagging bad channels for the OD, only the first condition is used.

5.3 Vertex Reconstruction

During propagation through the LS, particles deposit energy at some location emitting scintillation light isotropically. The isotropic distribution of photons will travel to the PMTs, with the closest PMT being hit first. A vertex for the interaction point can be reconstructed using the hit times of the first-arriving photons for every consecutive PMT relative to the first. There is also a small amount of Čerenkov light emitted at UV wavelength, but this is absorbed by the PPO and re-emitted

isotropically. Due to the lack of Čerenkov light, the directionality of particles cannot be determined.

The first step in determining the interaction vertex involves calculating a PMT hit time distribution, also called the *pulse shape*. The overall shape of the hit time distribution depends on many parameters, such as the PMT type (17-inch or 20-inch), vertex distance from the PMT, the light intensity of the interaction, the interacting particle type and the distance travelled through the LS. These parameters are tuned using radioactive source calibrations and are utilized by a vertex reconstruction algorithm called the V2 fitter. The V2 fitter has the benefit of using experimental pulse shapes taken from calibration sources to minimize biases and achieve superior vertex resolution.

The calculation of the vertex involves parameterizing pulse shapes by assuming an x, y, z and t, and then performing a maximum likelihood analysis to find the optimal timing distribution. The optimal time, τ_i, can be written as:

$$\tau_i = t_i - T' - T_i(x, y, z) \tag{5.1}$$

where t_i is the experimentally observed time of the i$^{\text{th}}$ PMT, T' is a global time offset for the arrival times, and $T_i(x, y, z)$ is the time-of-flight from the assumed vertex to the i$^{\text{th}}$ PMT. An accumulation of pulse shapes from a ^{60}Co calibration source depolyed at the center of the detector is shown in Fig. 5.1.

The likelihood and log-likelihood are joint probability functions that can be formed from the normalized pulse shape distributions, $\phi(\tau_i(x, y, z, t))$, as follows:

$$L = \prod_{i}^{N} \phi(\tau_i(x, y, z, t)) \tag{5.2}$$

$$\log(L) = \sum_{i}^{N} \phi(\tau_i(x, y, z, t)) \tag{5.3}$$

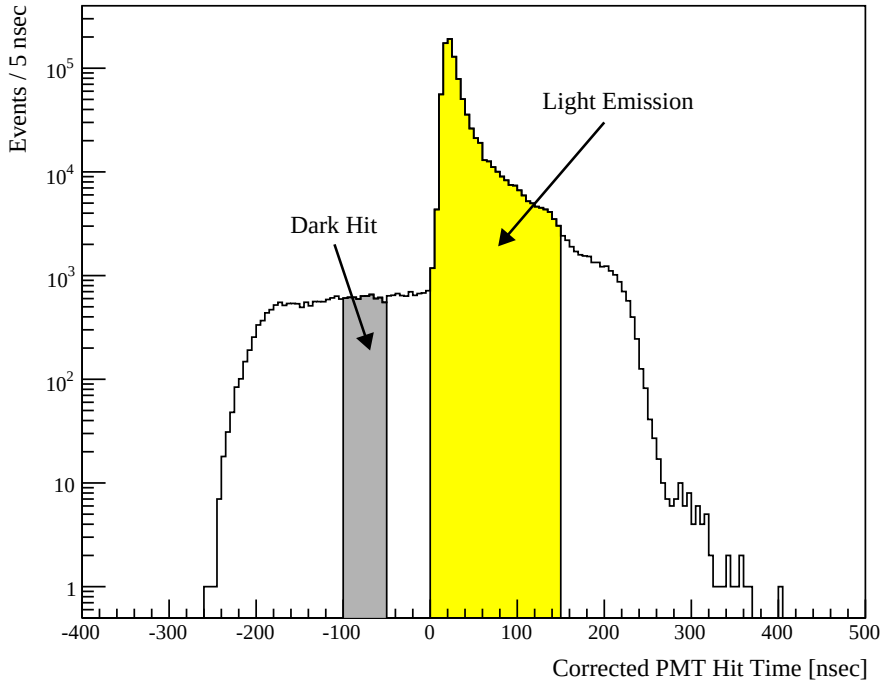

Figure 5.1: Accumulation of pulse shapes after the vertex correction for ^{60}Co calibration source events. The light emission peak region between 0 and 150 nsec is used to calculate the event charge. The gray area between -100 and -50 nsec is used to estimate the average dark hits and charge during each run.

where the product (sum) is over N, the number of PMTs with waveforms. The log-likelihood is more suitable for numerical analysis, since it involves sums instead of products. Varying x, y, z and t to find the maximum of $\log(L)$ gives the the most likely event vertex.

The procedure for finding the maximum of the log-likelihood is rather standard and involves minimzation/maximization routines. The algorithms were customized to reduce the amount of computation time and improve the speed of operation. Details of the methods used can be found in the appendix of Ref. [58]. After determining the optimal vertex the next step is to estimate the energy.

5.4 Energy Reconstruction

The visible energy of events can be estimated by calculating the total charge of all the PMTs with waveforms inside the hit window. The term visible energy implies the energy observed by the detector, which is not exactly equal to the energy deposited by the particle due to non-linear effects of quenching and Čerenkov emission.

The visible energy is defined as:

$$E_{vis} = E_0 \left(\frac{\sum_i^N Q_i^{obs} - Q^{dark}}{\sum_i^N Q_i^{exp}} \right) \tag{5.4}$$

where Q_i^{obs} is the observed charge for the i$^{\text{th}}$ PMT, Q_i^{exp} is the expected charge for the i$^{\text{th}}$ PMT, Q^{dark} is the estimated dark charge, and E_0 is a calibration constant chosen such that the visible energy of neutron capture events is equal to the real energy of 2.22 MeV.

The expected charge is expressed as:

$$Q_i^{exp} = \frac{e^{-L_i/\lambda}}{4\pi L_i^2} \, \eta_i \, \xi_i \cos\theta_i \tag{5.5}$$

where L_i is the distance of the vertex from the i$^{\text{th}}$ PMT, θ_i is the angle of incidence between the event vertex and the center of the PMT photocathode, λ is the Beer-Lambert light attenuation length and $4\pi L^2$ is a factor accounting for the solid angle subtended by the i$^{\text{th}}$ PMT. The correction factor for shadowing from the balloon and ropes is represented by η_i, and the correction for the 1 p.e. detection efficiency due to the FEE discriminator threshold is represented by ξ_i. The details of calculating the expected charge are based on Poisson statistics and can be found in Ref. [59].

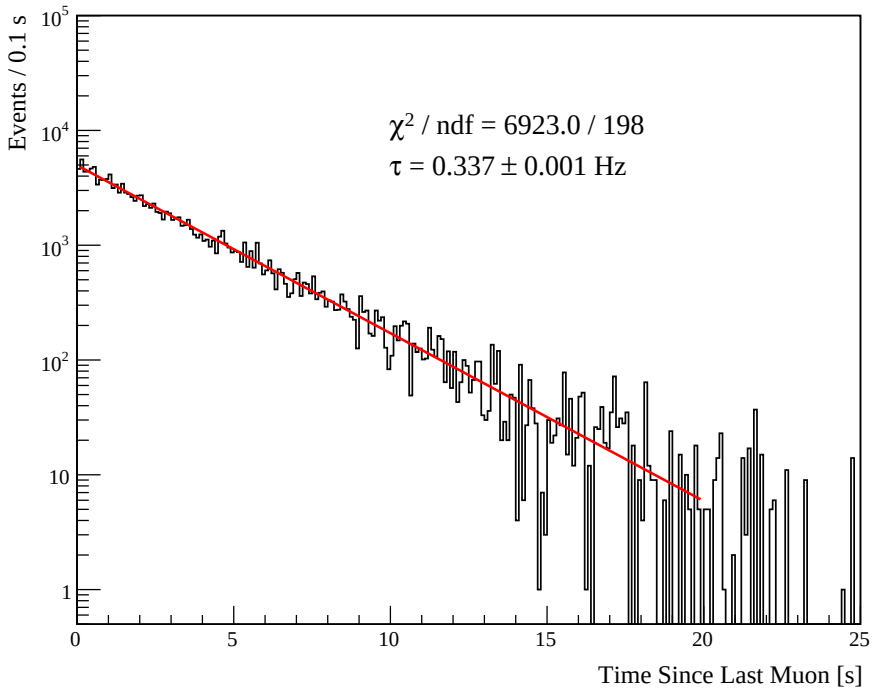

Figure 5.2: The relative time difference between muons fitted with an exponential decay function. From the fit, the muon rate is approximately 0.34 Hz.

5.5 Muon Tracking and Identification

KamLAND's senstivity to single p.e.'s allows detection of low energy physics events. When high-energy cosmic muons pass through the detector they deposit their energy at many steps during their propagation and cause an enormous amount of charge to be collected by the PMTs. The 2700 m.w.e. overburden helps to reduce the muon rate to about 0.34 Hz as seen from Fig. 5.2. Large signals from muons essentially blind the detector and produce radio-nuclides through nuclear spallation that contribute to the background for solar neutrino analysis. Therefore, accurate tagging and tracking of muons in the detector is essential.

5.5.1 Muon Selection Criteria

Muons that pass through the ID usually deposit charge in the OD as well, but sometimes this is not the case. In order for an event to be tagged as a muon, at least one of the following conditions must be satisfied:

- $Q_{17} \geq 10,000$ p.e.
- $Q_{17} \geq 500$ p.e. and $N_{OD} \geq 5$ hits

where Q_{17} is the total charge on the 17-inch PMTs and N_{OD} is the number of OD PMT hits. Most muon events satisfy the selection criteria and can be accurately reconstructed, but sometimes there are cases where muons do not satisfy the selection criteria. This can happen when a muon stops inside the detector depositing too little charge. Another case involves *showering muons*, where the charge deposited is too large to be due to a minimum ionizing particle and creates other high energy particles in the process. Miss-reconstructed muons and showering muons make up about 0.2% and 1.5% of all muons, respectively [60].

5.5.2 Track Reconstruction Algorithm

The track reconstruction for muons passing through the inner detector involves using the arrival time of Čerenkov photons emitted in the BO. Čerenkov photons are emitted at a characteristic opening angle from the muon track. The opening angle depends on the index of refraction of the liquid and the velocity of the muon. Using the parameterization in Fig. 5.3, the observed time of the earliest Čerenkov photons arriving at the PMTs, t, can be calculated as:

$$t = t_0 + \frac{l}{c} + \frac{n}{c} \cdot \frac{z - l}{\cos\theta} \tag{5.6}$$

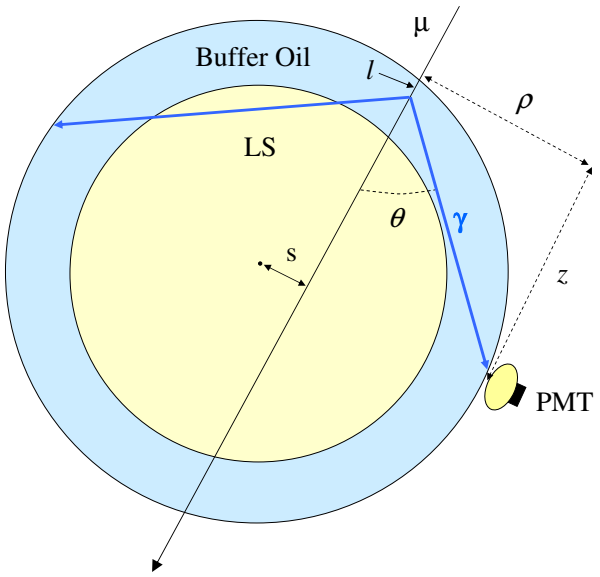

Figure 5.3: Diagram of a muon passing through the ID and emitting Čerenkov photons. The track is parameterized by the variables z, ρ, l, and θ. The variable s is the perpendicular distance of the reconstructed muon track to the center of the detector, also called the *impact parameter*.

where t_0 is the muon arrival time, l is the distance from the muon entrance to the Čerenkov emission vertex, n is the index of refraction, and c is the speed of light (used to approximate the muon's speed). Minimizing this equation gives the following conditions:

$$\frac{dt}{dl} = 0, \quad \cos\theta = \frac{1}{n} \tag{5.7}$$

which is the condition for the earliest photons arriving at the PMTs.

5.5.3 Muon Characterization

For muons which satisfy the selection criteria listed in Sec. 5.5.2 the track length in the inner detector and total charge are highly correlated. Muon tracks can be divided into two distinct groups. The tracks passing only through the BO are called *clipping muons*, where the charge comes from Čerenkov light produced in the BO.

Tracks passing through the BO and LS are called *through-going muons* and produce both scintillation and Čerenkov light. The charge per unit track-length for Čerenkov and scintillation light can be calculated as follows:

$$\left(\frac{dQ}{dx}\right)_{\check{C}er.} = \frac{Q_{17}}{L_{BO}} \tag{5.8}$$

$$\left(\frac{dQ}{dx}\right)_{Scint.} = \frac{Q_{17} - L_{BO}\left\langle\frac{dQ}{dx}\right\rangle_{\check{C}er.}}{L_{LS}} \tag{5.9}$$

where L_{BO} is the track length in both the LS and the BO, and L_{LS} is the track length in the LS. The charge/track-length correlations and the dQ/dx distributions can be seen in Fig. 5.4. The dQ/dx peaks are fit with a gaussian function to obtain the mean charge per unit track length resulting in the following:

$$\left\langle\frac{dQ}{dx}\right\rangle_{\check{C}er.} = 31.4 \text{ p.e./cm} \tag{5.10}$$

$$\left\langle\frac{dQ}{dx}\right\rangle_{Scint.} = 370.0 \text{ p.e./cm.} \tag{5.11}$$

The mean value of 370.0 p.e./cm for the scintillation charge per unit track is much lower than values of 629.4 p.e./cm calculated by a similar analysis using data accumulated before July 31, 2002 [60]. This large deviation comes from several different sources. Electronics upgrades and changes in thresholds accounts for roughly 7.5%, the long-term degradation of scintillator accounts for about 14.5%, and short-term degradation of the LS during distillation, discussed in Chap. 7, accounts for about 19.2%.

Another way to visualize the muon charge and track correlations is to use the impact parameter, which is the perpendicular distance between the muon track and the center of the detector. The correlation is shown in Fig. 5.5. A clear step can be

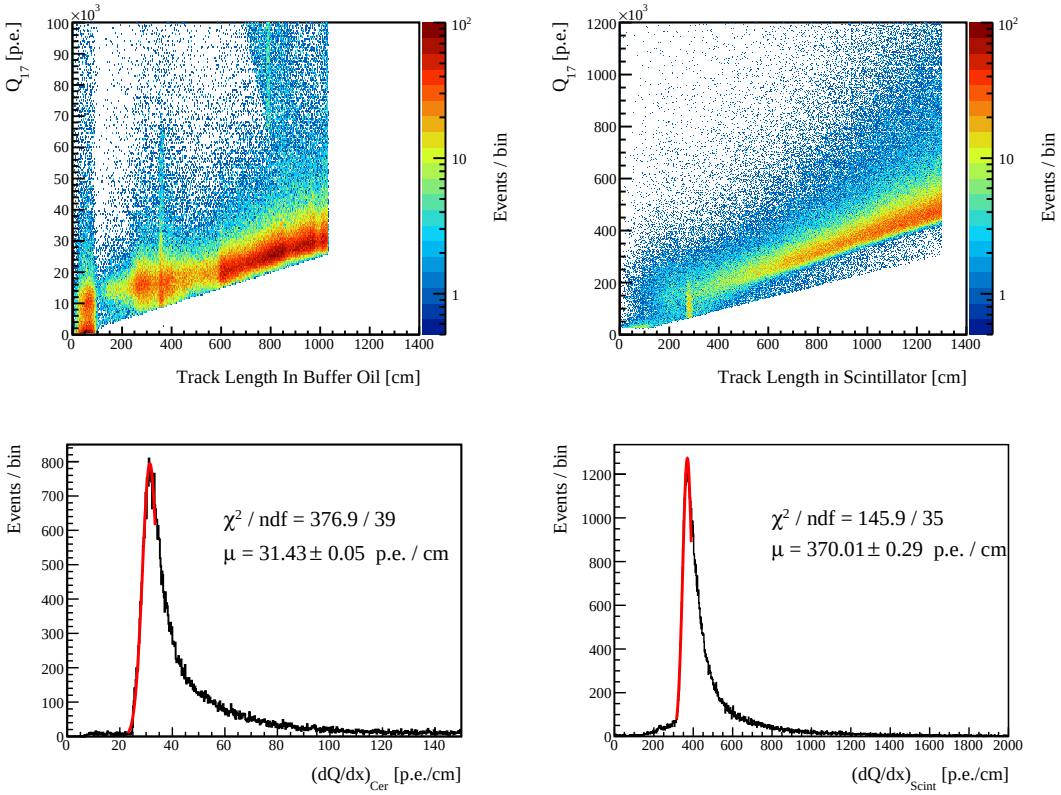

Figure 5.4: The top two plots show the correlation between charge and track length in the BO (upper left) and the LS (upper right). The bottom two plots show fits to the dQ/dx peaks for Čerenkov light (lower left figure) and scintillation light (lower right figure).

seen between the total charge for tracks passing through the LS and those passing only through the BO.

5.6 Reconstruction Biases and Performance

The overall accuracy and performance of the energy and vertex reconstruction algorithms is estimated by deploying calibration sources in the detector. The MiniCal system was used to deploy sources throughout the post-purification period when relevant ^{7}Be solar neutrino data was collected, so only this calibration data is considered in the following treatment.

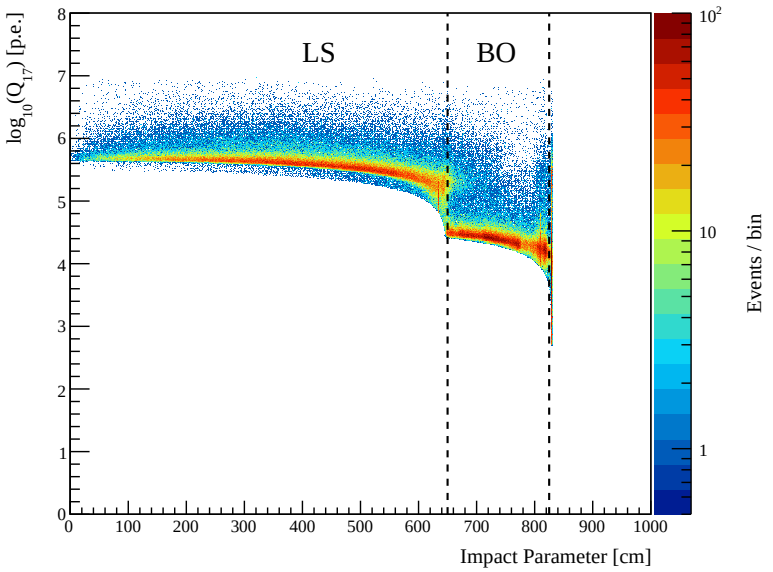

Figure 5.5: The correlation between muon charge and impact parameter.

The vertex reconstruction bias as a function of position along the vertical axis can be seen for the calibration sources in Fig. 5.6. The deviations are calculated from the difference between the known source position and fitted mean position returned from the vertex reconstruction. The maximum bias for sources within +4.5 m and -4.5 m is less than 4.4 cm. The vertex resolution was studied using the Monte Carlo method. A vertex resolution of 13.6 ± 1.8 cm / $\sqrt{\mathrm{E[MeV]}}$ was found to best reproduce the radial distribution of source events in the data [61].

The energy reconstruction also has a position dependent bias along the vertical axis which is shown in Fig. 5.7. The deviations are calculated relative to the reconstructed energy at the center of the detector. A maximum deviation of 3.6 % can be seen in the energy bias for positions within -4.5 m and +4.5 m. For positions inside -4.0m and +4.0 m, the maximum deviation is about 2.2 %. A fit to the energy resolution as a function of visible energy is estimated to be 7.80 ± 0.07 % and is shown in Fig. 5.8. The results from both the vertex bias and energy bias studies are summarized in Table 5.1.

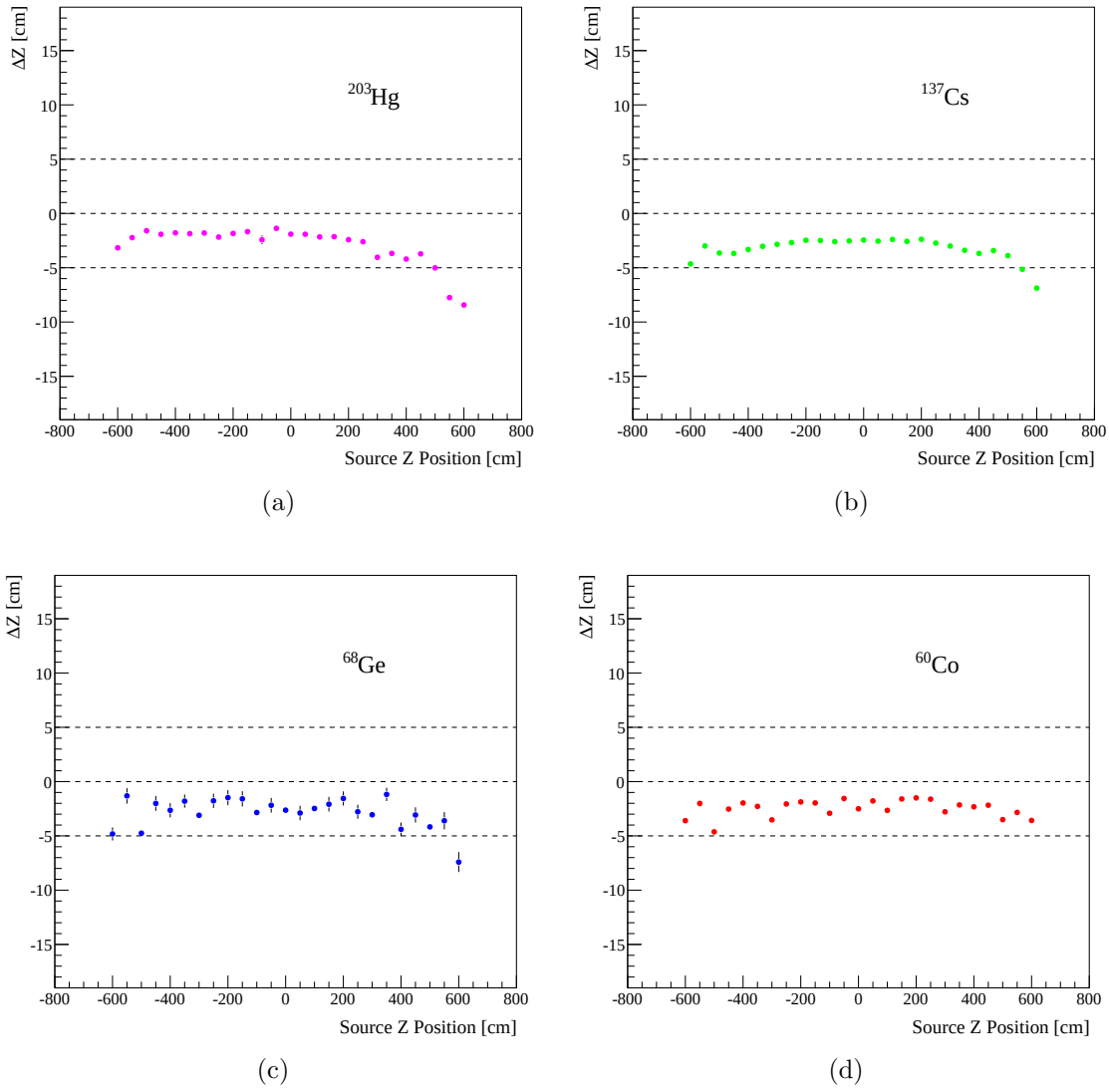

Figure 5.6: The vertex bias along the z-axis of the detector for different calibration sources taken after purification. The horizontal dotted lines at -5 cm, 0 cm, and +5 cm are shown for reference. The maximum vertex bias for all sources positioned within -4.5 m and +4.5 m is less than 4.4 cm. A summary of the maximum vertex bias for each source is shown in Table 5.1.

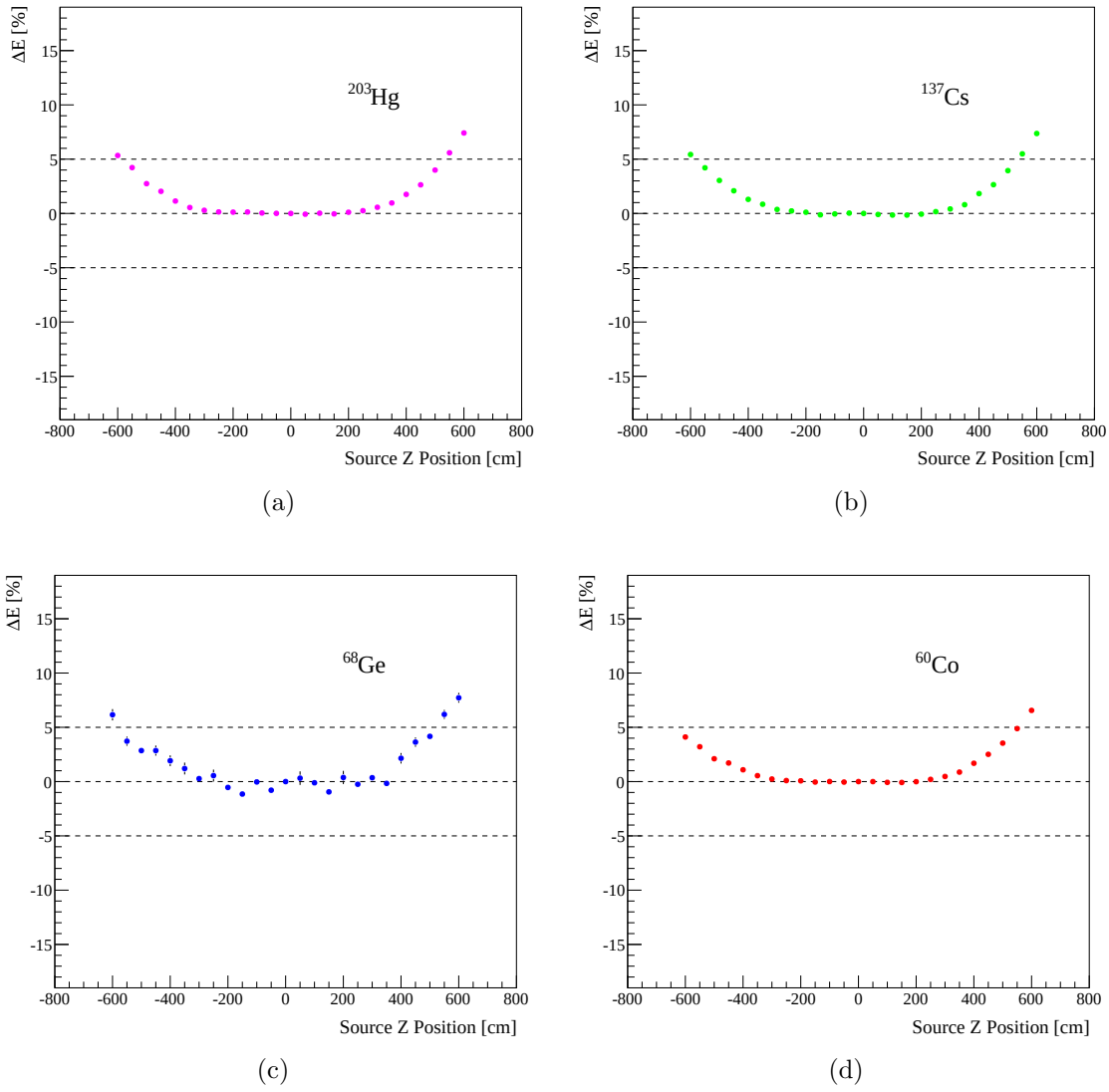

Figure 5.7: Visible energy bias along the z-axis of the detector for different calibration sources taken after scintillator purification. The horizontal dotted lines at -5%, 0%, and +5% are shown for reference. The maximum energy bias is less than 3.6% for all sources positioned within -4.5 m and +4.5 m, and less than 2.2% for all sources positioned within -4.0 m and +4.0 m. A summary of the maximum energy bias for each source is shown in Table 5.1.

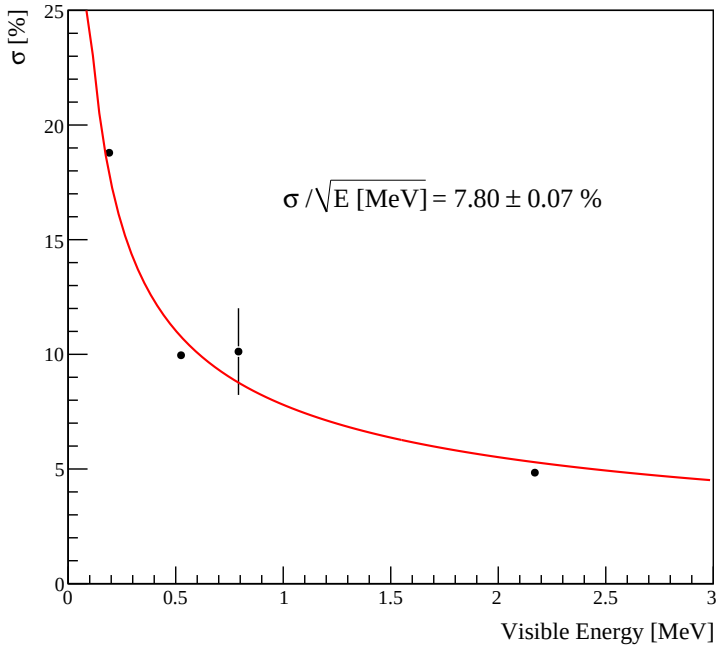

Figure 5.8: Resolution as a function of energy for various calibration sources. A fit to the data gives an energy resolution of 7.80 ± 0.07 % / $\sqrt{E[\mathrm{MeV}]}$.

Source	Maximum ΔZ	Maximum ΔE
^{203}Hg	4.2 cm	1.8 % (2.6 %)
^{137}Cs	3.7 cm	1.9 % (2.7 %)
^{68}Ge	4.4 cm	2.2 % (3.6 %)
^{60}Co	3.5 cm	1.7 % (2.5 %)

Table 5.1: Summary of the maximum deviations in the vertex and energy reconstruction for different sources. The deviations of ΔZ are the same for both 4.0 m and 4.5 m fiducial volumes. The deviations of ΔE are reported for a 4.0 m fiducial volume with the deviations for a 4.5 m fiducial volume reported in parentheses.

5.7 Trigger Threshold Correction

As mentioned in Chap. 4.5, the prompt, delayed and prescale triggers are used to acquire low energy data efficiently. Due to the implementation of different trigger thresholds during the time over which the data have been accumulated, corrections have to be made in order to combine the data. Fig. 5.9 shows an overlay of livetime-corrected solar data collected from the prescale trigger and prompt/delay triggers. A downturn caused by the prompt trigger threshold can be seen in the prompt data below 0.35 MeV.

To calculate the threshold for a trigger it is helpful to consider the case of all events having equal Nsum. The visible energy of these events will not be a delta function, but instead, a Gaussian peak with a characteristic width. For Nsum values that approach the trigger threshold only the amplitude of the Gaussian peak varies (to first order). Therefore, the visible energy is the sum of Gaussian distributions

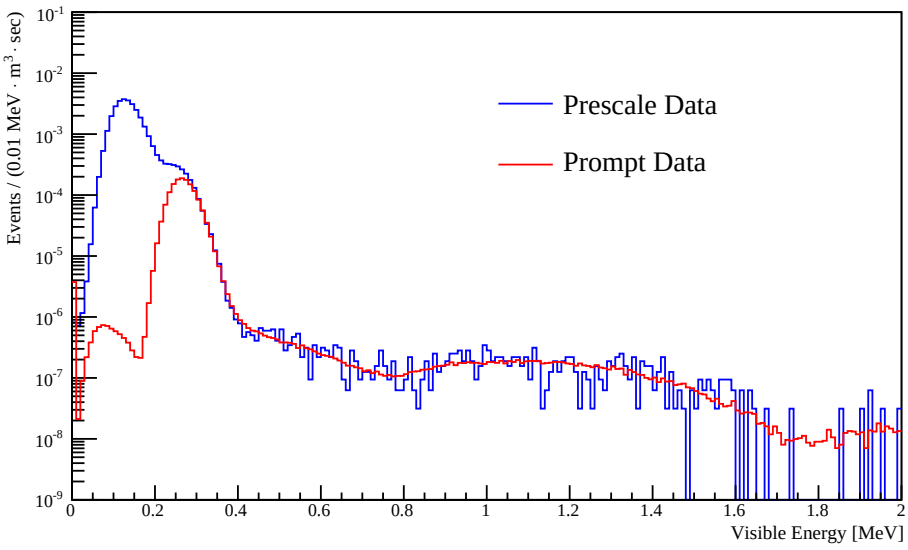

Figure 5.9: Overlay of the prescale trigger and prompt trigger data sets scaled by their corresponding live times and fiducial volumes.

from Nsum and the trigger efficiency is approximated by an error function given by:

$$\epsilon\left(E_{vis},\mu,\sigma\right)=\frac{1}{2}\left\{1+\mathrm{Erf}\left(\frac{E_{vis}-\mu}{\sigma\sqrt{2}}\right)\right\}. \tag{5.12}$$

The calculation of trigger efficiencies involves using a single data set with two different threshold cuts applied. For the prompt trigger, the first cut is a software threshold greater than the prompt trigger threshold of 70 Nsum, and the second is a hardware threshold set by the prescale trigger of greater than 40 Nsum. To calculate the prompt trigger efficiency, a ratio is formed from the data after the cuts are applied in the following manner:

$$\epsilon(prescale)=\frac{\mathrm{Nsum}>70}{\mathrm{Nsum}>40}. \tag{5.13}$$

The prescale trigger efficiency is calculated in a similar fashion using a special data set where the prescale hardware threshold was lowered to greater than 30 Nsum, and calculating a similar ratio using a software threshold greater than 40 Nsum as:

$$\epsilon(prompt)=\frac{\mathrm{Nsum}>40}{\mathrm{Nsum}>30}. \tag{5.14}$$

The resulting ratios are fit with the error function to obtain efficiency correction functions for the prompt and prescale triggers, which are shown in Fig. 5.10. The prompt data is corrected with the fitted efficiency down to a cutoff of 0.35 MeV, where it is combined with the prescale data corrected down to 0.7 MeV. The combined solar data set after the trigger efficiency corrections is shown in Fig. 5.11, where a smooth transition can be seen between the transition between prescale and prompt data.

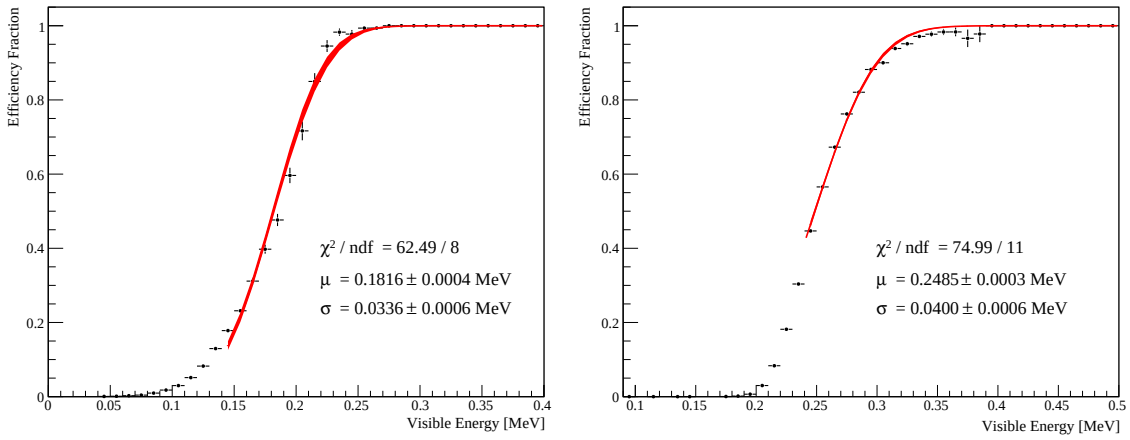

(a) (b)

Figure 5.10: Error function fits to the prescale efficiency and prompt efficiency as a function of visible energy are shown in (a) and (b) respectively. Both fits are drawn with a red band showing the 1σ error region.

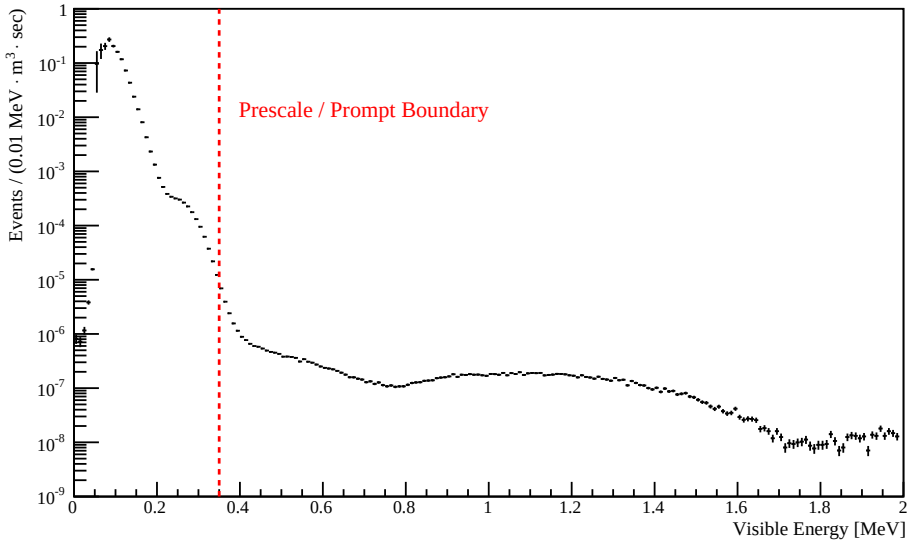

Figure 5.11: Visible energy spectrum after the trigger corrections have been applied. The dashed red line marks the boundary between the prescale and prompt data.

Chapter 6

Solar Neutrino Backgrounds

An observation of the signal from ^{7}Be solar neutrinos in the KamLAND detector require knowledge of the shape of the energy distribution produced by $e - \nu$ scattering. The calculated shape of the signal is combined with the shapes of all relevant backgrounds in a fit to the visible energy spectrum in order to extract a measurement of the flux. As seen in Chap. 3, the ^{7}Be solar neutrino signal appears below 1 MeV where the dominant backgrounds are produced by radio-impurities. The decay products (α's, β's, and γ's) of radio-impurities have energies which are of the same order as the signal, essentially erasing the sensitivity required for a flux measurment. A successful observation of the signal meant that the backgrounds needed to be identified, quantified, and sufficiently reduced.

A discussion of the radio-impurities is presented here, along with estimates of their abundances in the KamLAND detector before May 2007. A more detailed analysis of backgrounds in KamLAND can be found in Ref. [62]. A calculation of the signal to background ratio is provided at the end of this chapter and shows how detrimental the backgrounds are to a flux measurment. Efforts to reduce the backgrounds involved a major purification campaign which is covered in more detail in Chap. 7.

6.1 Internal Backgrounds

The backgrounds can be divided into two major categories: internal and external. The internal backgrounds are caused by radio-impurities inherent in the liquid scintillator and come from man-made and naturally occuring sources. The oil-based components of the scintillator were extracted from the Earth, a process which exposes them to the metallic radio-nuclides: ^{232}Th, ^{238}U, and ^{40}K. Due to the carbon-based nature of the components, contamination from ^{14}C is also inevitable. During the manufacturing and transportation of the components to the detector there was exposure to the atmosphere, containing gaseous radio-nuclides ^{222}Rn, ^{85}Kr, and ^{39}Ar. Another source of background comes from spallation by-products induced by cosmic rays passing through the scintillator, and include ^{7}Be, ^{11}C, and ^{10}C. A brief description of relevant radio-nuclides and their estimated abundances in the scintillator is provided in this section.

With the majority of backgrounds existing in the form of internal radio-nuclides, it is necessary to calculate the expected shape of these decays in order to accurately determine their abundances. A detailed explanation of the physics of radioactivity and the calculation of shapes of beta spectra can be found in Ref. [63]. In this work, the calculations of beta spectrum shapes have been made using a software package called KBeta, which was developed by Andreas Piepke, Greg Keefer and Lindley Winslow. An explanation of the software and a verification of its accuracy can be found in Ref. [62].

6.1.1 ^{232}Th

Thorium is an element naturally found in the Earth, it is almost exclusively composed of ^{232}Th and has a half-life of 14.05 billion years. The daughters of ^{232}Th undergo α and β decay of which the energies span the entire ^{7}Be solar neutrino

window. The decay series for ^{232}Th is shown in Fig. A.1.

Estimating the abundance is best done utilizing the sequential ^{212}Bi-Po decays having a short correlation time of 0.299 μs. This allows the tagging of ^{212}Bi-Po $\alpha - \beta$ events in the data which coincide in space and time. There are, of course, other long-lived daughters in the ^{232}Th that if introduced independently into the detector, could contribute to the number of observed ^{212}Bi-Po events. Therefore, it is the assumption that the long-lived nuclei are in secular equilibrium when using ^{212}Bi-Po events to estimate the ^{232}Th concentration. A short data period containing information from tagged ^{212}Bi-Po events is shown in Fig. 6.1. The signal to background ratio obtained from the time correlation is 88:1, which is superb given the ^{232}Th concentrations in the scintillator are on the order of 10^{-17} g/g.

After the number of ^{212}Bi-Po events are calculated, the efficiencies from the data cuts on the spatial correlation, time correlation and energy distributions are determined. These efficiencies, assumed to be uncorrelated, can be multiplicatively combined into one overall cut efficiency, denoted as ϵ_c. This efficiency is used to calculate an activity per unit volume at a mean time, t, in the following way:

$$A(t) = \frac{\int N(t)\, dt}{\epsilon_c\, \epsilon_b\, T\, V} \tag{6.1}$$

where ϵ_b is the branching ratio, T is the total live-time, and V is the fiducial volume. The activity per unit volume is expressed as an activity concentration in Bq per gram after dividing by the scintillator density in units of grams per cubic meter. The concentration is expressed in units of grams Th per grams scintillator after multiplying the activity by the ^{232}Th molar mass and life-time, and then dividing by Avagadro's constant. It's also beneficial to report the concentrations in units of events/(kton·day), which provides a direct comparison with the expected event rate from solar neutrinos.

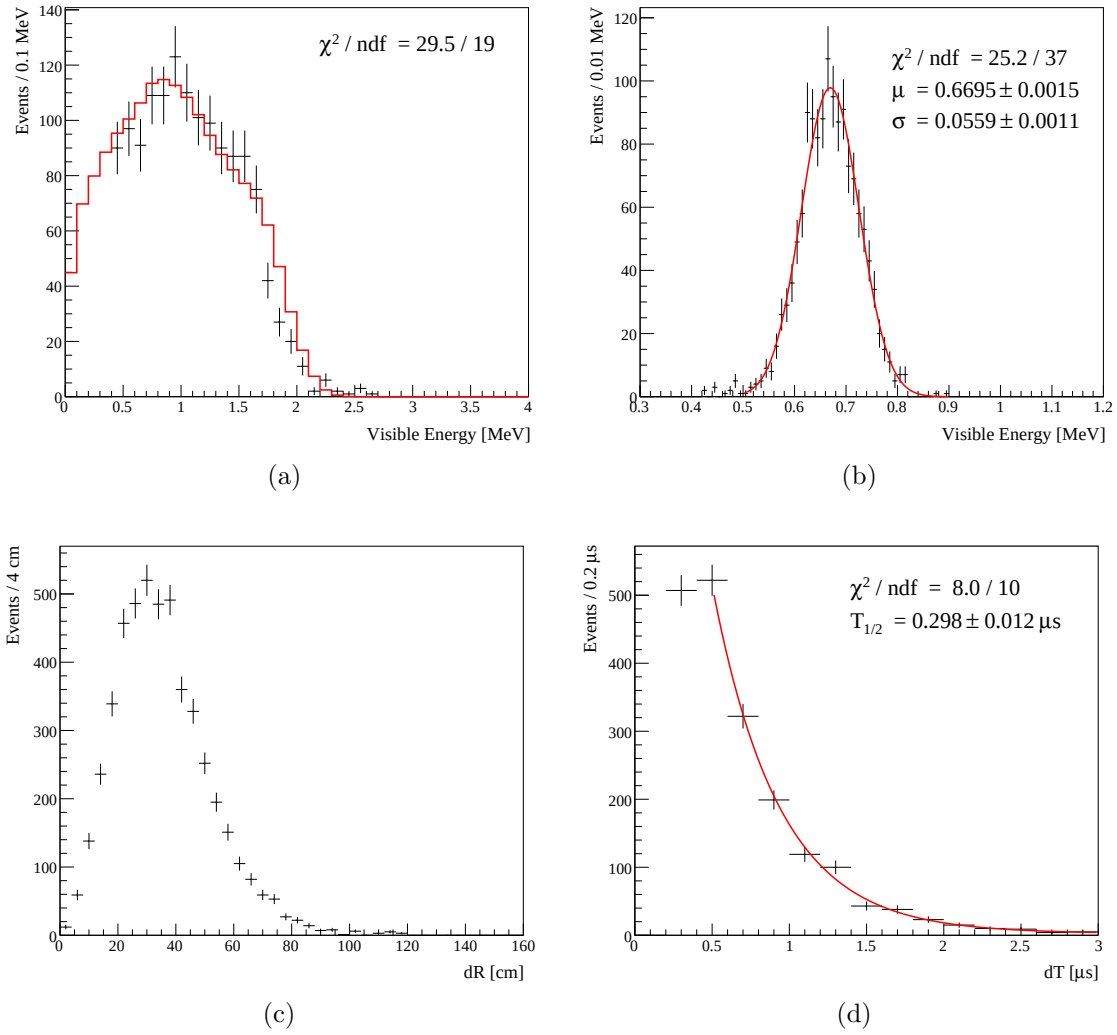

Figure 6.1: Data period containing ^{212}Bi-Po tagged events. The tagged ^{212}Bi beta events (in black) with a MC fit (in red) are shown in (a), and a Gaussian fit to the ^{212}Po alpha events is shown in (b). The spatial correlation and fitted time correlation between coincidence events are shown in (c) and (d), respectively. The half-life from the exponential fit to the time correlation comes in good agreement with 0.299 μs half-life of ^{212}Po. The signal to background ratio obtained from the time correlation plot is 88:1.

Two different analyses have been made of the ^{232}Th concentration in the detector before May 2007. The first was made for the initial reactor anti-neutrino analysis using 145.1 days of live time in 2003, yielding a concentration of $(5.2\pm0.8)\times10^{-17}$ g/g [64]. A second determination was made using almost all of the data available before the purification campaign began constisting of five years of live time. This analysis determined a concentration of $(8.24\pm0.49)\times10^{-17}$ g/g or 28.9 ± 1.7 events/(kton·day) [62]. In terms of making a ^{7}Be solar neutrino flux measurement, both of the reported concentrations of ^{232}Th in the detector were at a satisfactory level of $< 10^{-16}$ g/g.

6.1.2 ^{238}U

Uranium is another element found in the Earth, of which the most common isotope is ^{238}U making up 99.2745% of the natural abundance. The half-life of ^{238}U is 4.468 billion years. The ^{238}U series is shown in Fig. A.2. The daughters emit α's, β's and γ's forming a continuous energy spectrum that overlaps the ^{7}Be solar neutrino window.

Estimating the concentration of ^{238}U also involves utilizing a fast decay sequence, this time ^{214}Bi-Po space and time correlated events. The tagging is analagous to what was done for the ^{212}Bi-Po events, with a somewhat longer half-life of ^{214}Po of 164.3 μs, which undergoes α-decay. Various event distributions resulting from ^{2124}Bi-Po tagging can be seen in Fig. 6.2. It should be noted that the radio-nuclides ^{222}Rn and ^{226}Ra both contribute to the ^{214}Bi-Po decay rate in the scintillator. It is assumed that these are in equilibrium with ^{238}U. It should also be noted that the signal to background ratio obtained from the time correlation plot is 404:1, meaning that this determination of the ^{238}U concentration on the order of 10^{-18} g/g is essentially background-free!

There have been periods where ^{222}Rn concentrations increased during calibration source deployments and distillation of the scintillator. Fortunately, ^{222}Rn has a 3.82

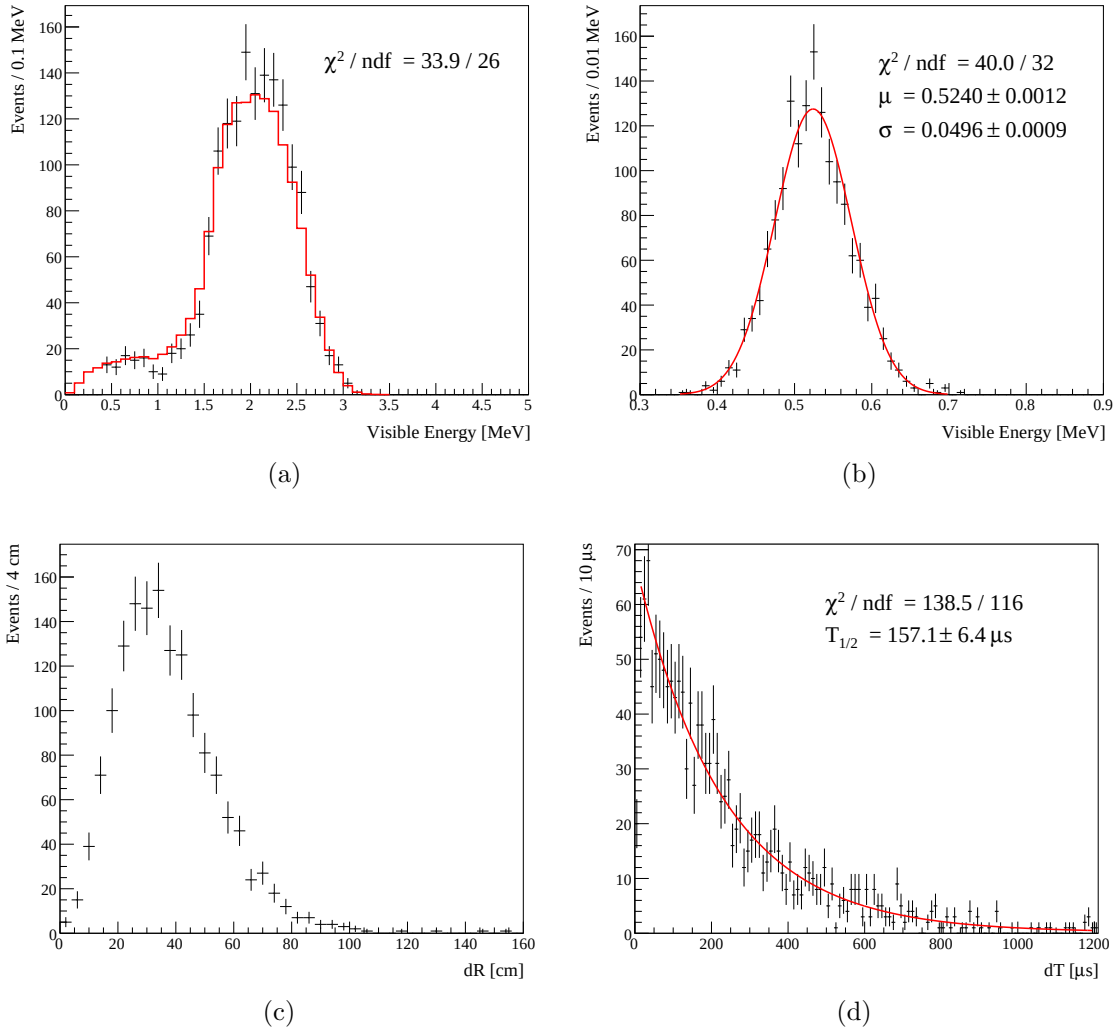

Figure 6.2: Data period containing ^{214}Bi-Po tagged events. The tagged ^{214}Bi beta events (in black) with a MC fit (in red) are shown in (a), and a Gaussian fit to the ^{214}Po alpha events is shown in (b). The spatial correlation and fitted time correlation between coincidence events are shown in (c) and (d), respectively. The half-life from the exponential fit to the time correlation comes in good agreement with 164.3 μs half-life of ^{214}Po. The signal to background ratio obtained from the time correlation plot is 404:1.

day half-life making it possible to observe the decay of ^{222}Rn into equilibrium via ^{214}Bi-Po coincidence event tagging and also estimate concentrations of ^{222}Rn introduced into the detector. Calculations of the ^{238}U concentration use data excluding periods with broken equilibrium.

Previous calculations of the ^{238}U concentration were made using the earlier data before purification as described in 6.1.1. The calculation from the first reactor analysis reported a value of $(3.5 \pm 0.5) \times 10^{-18}$ g/g [64]. The second, more thorough, calculation with five years of live time gave a concentration of $(1.87 \pm 0.10) \times 10^{-18}$ g/g or 2.0 ± 0.1 events/(kton·day) [62]. Both of the reported concentrations of ^{238}U were at a satisfactory level of $< 10^{-17}$ g/g.

6.1.3 ^{40}K

A measurement of the ^{40}K concentration has been performed by spectroscopic analysis [62]. This approach required the use of KBeta to calculate the shape of the ^{40}K decay spectrum, which has two modes of decay: beta and electron capture (EC). The beta decay occurs with a branching ratio of 89.28% resulting in a continuous energy spectrum which has an endpoint energy of 1.311 MeV. If the concentration of ^{40}K is too high, the beta spectrum will be a background for the solar neutrino signal. The EC mode has a branching ratio of 10.72% and produces a single 1.461 MeV gamma-ray. This mono-energetic gamma provides a distinct feature in the data when making a measurement of the ^{40}K concentration, but the analysis must be conducted with a carefully chosen fiducial volume cut (here a radius of 3.0 meters) to reject contributions of ^{40}K gammas coming from the ropes and balloon. The estimated concentration before May of 2007 is $(1.30 \pm 0.11) \times 10^{-16}$ g/g or $(2.98 \pm 0.25) \times 10^{3}$ events/(kton·day). A satisfactory concentration of ^{40}K for a solar neutrino measurement would be less than 10^{-18} g/g.

6.1.4 ^{14}C, ^{85}Kr, ^{39}Ar, ^{210}Po, and ^{210}Bi

The most important backgrounds for the solar neutrino analysis give energy deposits mostly below 2 MeV, defining its unique shape. Before the purification campaign the largest background came from ^{85}Kr, which is a gaseous element that can be found in the atmosphere with concentrations that vary somewhat depending on geographical sampling location. The half-life of ^{85}Kr is 10.756 years, and it dominantly β-decays to the ground state of ^{85}Rb. There is a sub-dominant excited state transition with a branching ratio of 0.43%. This state is included in the consideration of the spectral shape since the 1.015 μs half-life of the excited state allows for the detection of the β and γ particles as separate events. The β-ray from the excited state decay is neglected since its endpoint energy of 0.173 MeV is below the trigger detection threshold.

Another gaseous nuclide which is present in the atmosphere in trace amounts is ^{39}Ar. The concentration of ^{39}Ar in the scintillator was sub-dominant compared to ^{85}Kr but still needed consideration. It has a half-life of 269 years and undergoes β-decay to the ground state with an endpoint energy of 0.565 MeV.

As mentioned previously, the liquid scintillator was exposed to both ^{222}Rn and ^{238}U throughout its existence. Both of these radio-nuclides eventually decay into ^{210}Pb, which has a very long half-life of 22.3 years. ^{210}Pb continuously feeds both ^{210}Bi and ^{210}Po. The β-spectrum of ^{210}Bi has an endpoint energy of 1.163 MeV and ^{210}Po has a single α-decay which forms a peak near 0.250 MeV in visible energy.

To determine the abundances of the dominant radio-impurities at low energies, a spectral fit is performed. This approach uses a probability density function, B, which is the sum of all the background spectra, b_i given as:

$$B(E, a, \epsilon_\beta) = \sum_{i}^{backgrounds} a_i \cdot b_i(E(\epsilon_\beta)) \tag{6.2}$$

where the amplitudes of the spectra, a_i, and an energy scale shift, ϵ_β, are free floating parameters. The term ϵ_β allows for freedom in the energy scale due to systematic uncertainty and relates the expected visible energy to the binned energy as:

$$E_{bin} = (1 + \epsilon_\beta)E_{vis} \tag{6.3}$$

The best-fit of the composite spectrum to the data is found using tools from a software package, MINUIT [65], which accompanies the ROOT software libraries [66]. MINUIT's libraries are used to minimize the Pearson's chi-square:

$$\chi^2 = \sum_j^N \frac{(B(E, a_i, \epsilon_\beta) - x_j)^2}{(\Delta x_j)^2} \tag{6.4}$$

where N is the number of bins, x_j is the observed counts for the j^{th} bin, and Δx_j is the standard deviation of the counts in the j^{th} bin.

A composite fit of the background data before purification can be seen in Fig. 6.3. The data analysis uses a 4.0 meter radius fiducial volume and consists of 3.247 days of live time. This energy spectrum is produced after a 2.0 ms muon cut, and only includes well-reconstructed physics events as returned by the energy and vertex fitters. The fit region is from 0.13 to 1.9 MeV and includes the ^{40}K spectrum and the spallation isotopes ^{11}C and ^{10}C at higher energies. The total expected signal from all branches of solar neutrinos is overlaid in gray, where the ^{7}Be solar neutrino signal dominates from 0.25 to 0.80 MeV. The ^{14}C spectrum can be seen at very low energies, but the endpoint falls short of the window for ^{7}Be solar neutrino analysis.

Table 6.1 summarizes the values obtained for the backgrounds in the fit. The fit value for ^{40}K in Fig. 6.3 is about a factor of two higher than the value quoted in Sec. 6.1.3 where a 3.5 meter radius fiducial volume cut was used to avoid contributions from ^{40}K gammas emitted by the outer detector components. The background event

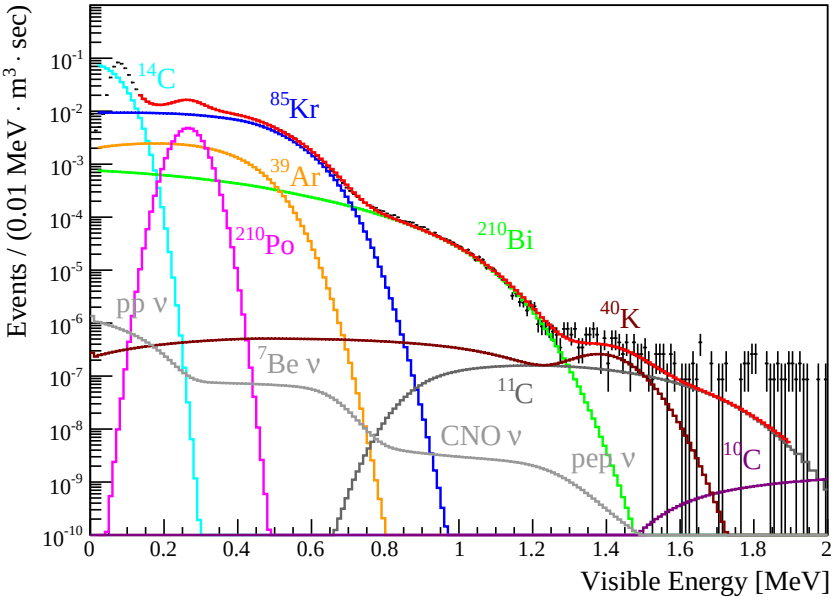

Figure 6.3: Composite fit to the low energy data before purification. The data set consists of 3.247 days of live time using a 4.0 meter fiducial radius. The sum of all the individual fitted spectra is shown in red and the black points with errors bars are the data.

Isotope	Fit Value [events/(kton·day)]
^{14}C	$(7.14 \pm 0.35) \times 10^7$
^{210}Po	$(5.01 \pm 0.03) \times 10^6$
^{210}Bi	$(4.00 \pm 0.02) \times 10^6$
^{85}Kr	$(4.91 \pm 0.09) \times 10^7$
^{39}Ar	$(1.08 \pm 0.10) \times 10^7$
^{40}K	5487.0 ± 1107.6
^{11}C	1151.5 ± 176.5
^{10}C	21.1 ± 1.8
χ^2/ndf	1152.7/166
ϵ_β	-0.536 ± 0.001 %

Table 6.1: A summary of the fit results from Fig. 6.3. The event rates reported here are obtained from integrating over the entire energy range.

rate inside the 0.25 - 0.85 MeV region is 3.3×10^7 events/(kton·day) compared to a ^{7}Be solar neutrino rate of 305 events/(kton·day). The event rate from the other solar neutrino branches inside this region is 75.0 events/(kton·day).

In order to make a ^{7}Be solar neutrino measurement, the backgrounds needed to be reduced dramatically. To put this into perspective, a Monte Carlo calculation of an ideal background reduction scenario can be seen in Fig. 6.4. The inputs for the calculation and the desired reduction factors are reported in Table 6.2. Included in the calculation are the ^{232}Th and ^{238}U spectra with the concentrations reported in Sec. 6.1.1 and 6.1.2, respectively. These two backgrounds have very little contribution to the event rate in the 0.25 - 0.85 MeV region with only 2.7 events/(kton·day) from ^{238}U and 19.9 events/(kton·day) from ^{232}Th.

The gamma peak near 0.4 MeV from the ^{7}Be electron capture decay needs to be incorporated into the calculation. Since this is a spallation background it is irreducible and contributes 59.6 events/(kton·day) inside the 0.25 - 0.85 MeV region. The input value in the MC calculation was obtained from the spectral analysis discussed in Chap. 9. Estimates of the ^{7}Be event rates have been made in Refs. [67] and [68] from independent studies of muon-induced spallation products in KamLAND. However, it should be noted that the many values reported in these two texts are in large dissagreement with one another. Due to this uncertainty, the ^{7}Be gamma event rates quoted in these texts of $\sim$14 events/(kton·day) are rather uncertain.

It is clear that the highest background rates came from ^{85}Kr, ^{39}Ar, ^{210}Bi and ^{210}Po. The MC calculation assumed reduction factors of 10^6 for ^{85}Kr, ^{39}Ar and 10^5 for ^{210}Bi and ^{210}Po. The reduction factor for ^{40}K was assumed to be 10^2. Given this scenario, the total event rate due to backgrounds inside the 0.25 - 0.85 MeV region was estimated as 237.4 events/(kton·day) compared to 304.6 events/(kton·day) for ^{7}Be solar neutrinos setting the technical goals for the scintillator purification campaigns.

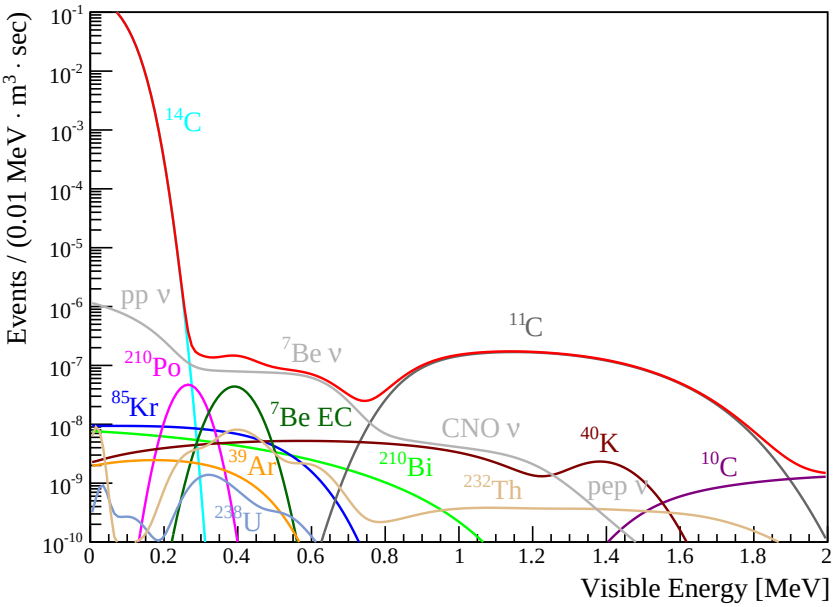

Figure 6.4: MC calculation of an ideal background reduction scenario for solar neutrino analysis. The spectra are quenched and folded with $7.8\%/\sqrt{\mathrm{E[MeV]}}$ to convert deposited into visible energy.

Isotope	MC Input [events/(kton·day)]	MC Reduction Factor
^{14}C	7.14×10^7	1.0
^{210}Po	50.1	10^5
^{210}Bi	40.0	10^5
^{85}Kr	49.1	10^6
^{39}Ar	10.8	10^6
^{40}K	54.9	10^2
^{11}C	1151.5	1.0
^{10}C	21.1	1.0
^{7}Be EC γ	59.2	1.0
^{238}U	2.0	1.0
^{232}Th	28.9	1.0

Table 6.2: Summary of the input values for each background from Fig. 6.4. The last column lists the assumed reduction factors in the MC calculation for each of the backgrounds from the ratio: (Before Purification Value)/(After Purification Value).

6.2 External Backgrounds

Until now, the backgrounds described have been inherent in the liquid scintillator. There also exist backgrounds from the detector material and components which encompass the scintillator and should be taken into account. Most of these backgrounds come from trace amounts of ^{40}K, ^{238}U, ^{232}Th and ^{222}Rn in the balloon, ropes, buffer-oil region, PMTs, etc. There also exists the possibility of trace amounts of ^{60}Co in materials made out of stainless steel. All of these radio-nuclides emit a variety of gamma's in their decays. If the rates are high enough, a small fraction of these gammas could deposit enough energy to fall inside the 0.25 - 0.85 MeV region and contribute to the background of a solar neutrino measurement.

The external gamma-ray backgrounds are what makes a radial fiducial volume cut necessary. Such a cut reduces the contribution from external gammas, but also reduces the solar target, and thus, the ^{7}Be solar neutrino event rate. A plot of the visible energy for several fiducial volumes of different radii is shown in Fig. 6.5. When no fiducial cut is made, two peaks can be seen from ^{208}Tl gammas near 2.615 MeV and ^{40}K gammas near 1.461 MeV. The effect from external gammas is decreases exponentially with smaller fiducial radius where the contributions from ^{208}Tl and ^{40}K gammas become unrecognizeable when the fiducial radius is less than 4.0 meters. At a fiducial volume radius of less than 4.0 meters, the contribution of external gammas to the visible energy spectrum becomes masked by the interal backgrounds.

One technique that provides more accurate estimates of the external backgrounds involves the use of a full detector MC simulation. This simulation uses precise knowledge of the KamLAND detector materials and geometry to calculate the transport of external gammas produced at various points outside the detector. The MC simulation of external gammas is discussed in more detail in Chap. 8.6.

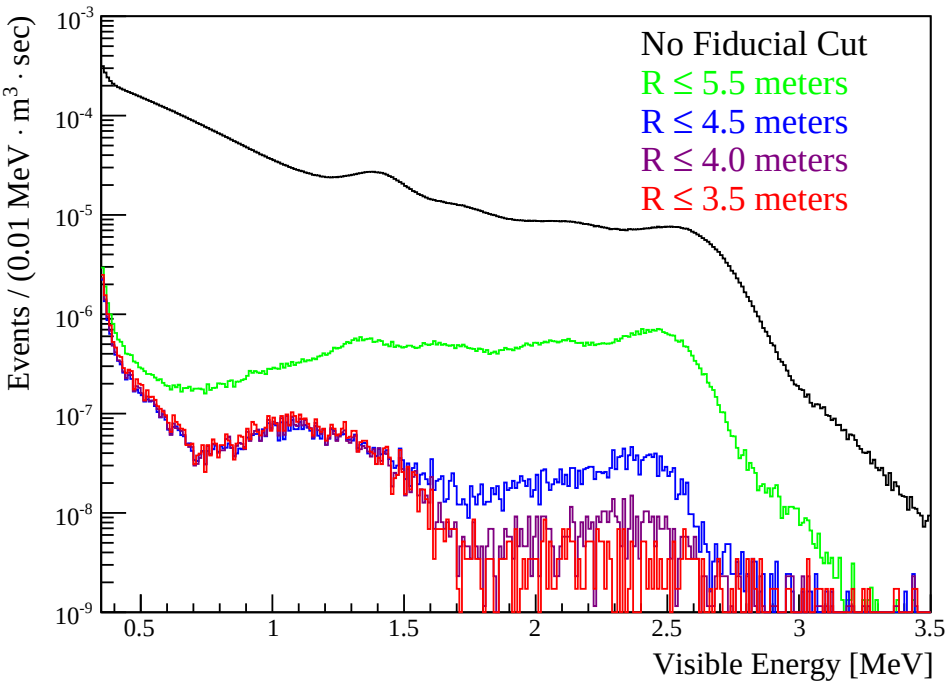

Figure 6.5: Comparison of the visible energy spectrum in KamLAND data for several fiducial volumes with different radii. When no fiducial cut is made, two peaks can be seen from ^{208}Tl gammas with 2.615 MeV and ^{40}K gammas with 1.461 MeV.

Chapter 7

KamLAND Purification

The backgrounds from the decays of ^{85}Kr, ^{39}Ar, ^{210}Bi, and ^{210}Po discussed in Chap. 6 are critical to a ^{7}Be solar neutrino measurement. This chapter describes the efforts to reduce these backgrounds during a massive purification campaign, which involved the construction of an enormous distillation and N_2 gas purging system capable of dealing with KamLAND's 1000 tons of scintillator within reasonable time. The system design relied heavily on laboratory studieds laying the foundation for the efficient removal of trace amounts of Pb and Rn daughters.

The purfication campaign was divided into two phases. The first phase ran from May 5, 2007 to August 1, 2007. During this time, approximately 1703 m^3 of scintillator was continuously circulated between a distillation and N_2 gas purging system and the KamLAND detector. Upgrades and modifications were made to the system to improve the operating efficiency and the second phase began in June 16, 2008. The second phase ended on February 6, 2009 after a total of 4736 m^3 of scintillator was purified. Throughout the two phases more than five full detector volumes had been purified, and left the levels of radio-impurities in KamLAND among the lowest of any experiment world wide.

7.1 Distillation System

The removal of trace amounts of ^{210}Pb daughters utilized fractionated distillation. During distillation, impurities are removed by utilizing different solubilities in the liquid and vapor phases. The separation of impurities from the LS arises from differences in boiling points with respect to the LS components. The impurities were left behind and LS components in the vapor phase were recombined in the proper proportions in the liquid phase. The Mitsui Engineering & Shipbuilding Company, LTD. (MESCO) was contracted to build the distillation system, a project which took approximately one year. During this time, the components of the system had to be cleaned regularly to maintain a high standard of cleanliness. The major components of the distillation system are outlined in Fig. 7.1.

The process began with LS being pumped from the KamLAND detector through a long series of pipes into a 0.5 m^3 buffer tank. At this point, new PC and Dodecane could be added to make up for loss during the distillation process and ensure proper density. This holding tank also had sampling lines to enable quality measurements of the scintillator composition, such as optical properties and radio-impurities.

The LS was sent from the buffer tank to a series of distillation towers. The PC has the lowest boiling point, followed by Dodecane, and PPO. After the PC was distilled, the denser leftover liquid was transferred to the Dodecane distillation tower where the separation of Dodecane and PPO occured. The separation of PPO from Dodecane required a secondary heating system, which circulated the PPO-Dodecane mixture through a closed system to concentrate the PPO. The leftover Dodecane distillate from the PPO concentrator was sent back to the Dodecane tower.

The distillation of PPO was the most difficult part of the purification process, because the operating conditions of the Dodecane and PPO distillation towers were vastly different. The small amount of Dodecane which remained in the PPO liquid

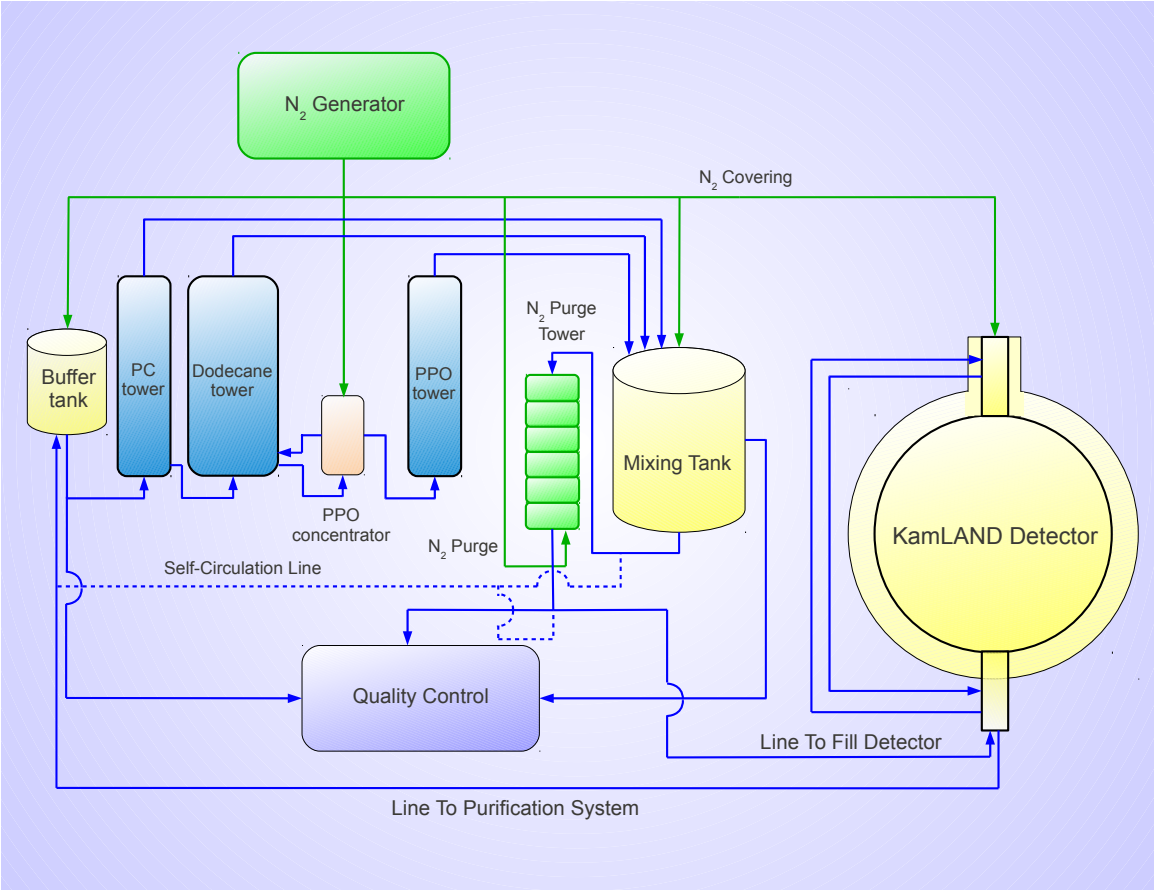

Figure 7.1: A simplified diagram of the distillation system with only the major components shown. The lines drawn in blue indicate the flow of liquid and the lines drawn in green indicate the flow of N_2 gas. The dashed lines were used when the distillation system was in self-circulation mode.

as it was sent to the PPO tower (about 5% per unit volume) would immediately vaporize. This caused large flucuations in the pressure, which forced PPO into the vacuum lines causing it to cool and solidify. The operations had to be halted for almost a month in order to clean all of the vacuum lines and pumps. In order to resolve this, the operating conditions for Dodecane and PPO distillation had to be optimized and the PPO had to be distilled in a batch mode. Approximately 25 kg of PPO needed to be kept in a reserve tank to maintain a continuous flow to and from KamLAND and great care had to be taken to ensure that there was no heat loss in

System Component	Pressure [kPa]	Temperature [°C]
PC Tower	2.0	62
Dodecane Tower	2.0	97
PPO Tower	0.6	175

Table 7.1: Operating parameters for each of the distillation towers. These parameters were controlled to within 1% variability.

any of the lines carrying PPO in order to maintain a liquid phase. Table 7.1 lists the operating conditions that were maintained for each of the distillation towers.

After the three LS components were distilled, they were sent to separate holding tanks and then recombined in the appropriate ratios in a 20 m^3 mixing tank. PPO had to be sent to the mixing tank at the same time with PC to help it dissolve into the scintillator. The quality control measurements of LS could be performed from a sampling port in the mixing tank. One important point to make is that the LS could not reside in the mixing tank for very long, and could only be filled to approximately 2 m^3. This was due to the effect of ^{222}Rn outgassing from the stainless steel components of the tank, which resulted in a build-up of ^{210}Pb over time. To avoid this accumulation of ^{210}Pb, the LS had to sent immediately to either the N_2 gas purging towers or back to the original buffer tank to begin self-circulation through the distillation system.

Upon entering the N_2 purge towers, the distilled LS was flushed with ultra-pure N_2 gas at a flow rate of 30 m^3/hr in order to remove gaseous radio-nuclides such as ^{222}Rn, ^{85}Kr and ^{39}Ar. A sampling port is also available to the LS line leaving the purge towers in order to allow for quality control measurements. After leaving the purge towers, the LS was sent through a series of pipes back to the KamLAND detector. At this point, the temperature of the LS was approximately 20°C and had to be cooled before filling it back into the detector. The cooling was necessary in

order to keep a clear separation between the purified LS and the unpurified LS in the detector. When the purified LS was being filled from the top of the detector, a temperature of 15°C was obtained by simply running mine water over the filling line. During filling from the bottom of the detector, a heat exchanger was used to assure a temperature of less than 10°C. Once these temperatures were reached, the detector was filled with purified LS at a flow rate of approximately 1 m^3/hr.

7.2 Ultra-High Purity Nitrogen Generator

Having a large supply of high purity N_2 gas on hand at all times was extremely important for the purification process. The N_2 gas was supplied to the holding tanks in the distillation system and to the neck region of the KamLAND detector in order to minimize air leaks. As mentioned previously, N_2 gas was used to in the purge towers to remove gaseous radio-impurities. Due to the large demand, Air Water Inc. of Osaka, Japan was contracted to design and build a high purity, high capacity N_2 generator in the Kamioka mine.

The nitrogen generator consumed a supply of outside air sent from the mine entrance at a rate of 200 m^3/hr and removed water and carbon dioxide through the use of an adsorbent. Air from outside the mine was used because the typical levels of Radon in the mine air is about two orders of magnitude higher than outside air. The air was compressed and cooled until condensation occured thereby producing liquid N_2. The liquid N_2 was continuously collected in a dewar and the boiled-off N_2 gas was sent to the distillation system and the KamLAND detector. A backup supply tank was also kept filled and could supply 5 m^3/hr to various system or detector components in the case of an emergency shutdown.

The high purity of the N_2 gas in terms of ^{222}Rn was extremely important. The concentration of ^{222}Rn in the N_2 supply was determined using an electrostatic collection

method to measure the alpha particles from ^{222}Rn daughters. These measurements determined a concentration of 12 ± 11 μBq/m^3 [69], which is about a factor 10^6 lower than air obtained outside the mine. The O_2 concentration was measured using monitors from the manufacturer and were determined to be about 1 ppm. Given that O_2 makes up about 20% of the atmosphere, the measured O_2 reduction in the N_2 gas is consistent with the measured ^{222}Rn reduction. The concentrations of natural Ar and Kr in the N_2 supply were measured by the manufacturer, and were determined to be 0.03 ppm and < 0.02 ppm, respectively [62].

7.3 Quality Control Measurements

Quality control measurements were essential to ensure that the purified LS was safe for filling into the KamLAND detector. The LS was sampled on regular intervals while the distillation system was running, sampling occured as well during crucial periods when the system had to be restarted after being shutdown for maintenance and cleaning. The quality control involved measuring the ^{222}Rn and ^{85}Kr concentrations, optical transparency, light yield, density, and PPO concentration. Most of these tasks were performed by auxiliary systems in a special clean room located within the purification area unless otherwise noted. Monitoring of the attenuation length and light yield was a responsibility of our group at the University of Alabama.

7.3.1 ^{85}Kr and ^{39}Ar Monitoring

Two of the largest backgrounds before purification came from ^{85}Kr and ^{39}Ar making them important backgrounds to monitor during the purification campaign. A dedicated detector, consisting of a residual gas analyzer (RGA) and cold trap, was designed by collaborators at Caltech with the goal of achieving a few μBq/m^3 sensitivity

for ^{85}Kr. The description of this system can be found in detail in Ref. [70]. Measurements made with this system relied on the assumption that the ratios, ^{85}Kr/^{nat}Kr and ^{39}Ar/^{nat}Ar are known. These calculated ratios are also explained in Ref. [70], where ^{85}Kr/^{nat}Kr and ^{39}Ar/^{nat}Ar were determined to be $(2.8 \pm 1.4) \times 10^{-11}$ and $(8.1 \pm 0.3) \times 10^{-16}$, respectively.

The operation required a 5 liter sample of LS to be fed into a bubbler directly from a line in the purification system. Upon entering the bubbler, the LS was sparged with Helium gas. The sparging was performed until saturation of the Kr and Ar was achieved within the Helium gas. The Helium gas was passed through a molecular sieve trap kept at 77 K in order to freeze out the Kr and Ar. The trap was later heated to release the Kr and Ar gasses into a vacuum line which was connected to an RGA. The vacuum line was kept below 10^{-7} Torr by continuous operation of a turbomolecular pump. When the gasses entered the vacuum line, the pressure increased which is directly proportional to the amount of gas released from the trap. The RGA measured these partial pressures of the gasses as a function of their mass.

The sensitivity of this system was later enhanced by the addition of an electron mulitplier, which allowed sensitivities to reach 10^{-12} Torr. This corresponded to an overall sensitivity of 30 μBq/m^3 for ^{85}Kr with 78% systematic uncertainty and 0.3 μBq/m^3 for Ar^{39} 10% systematic uncertainty. All measurements of purified LS performed with this system found no sign of Kr or Ar above these sensitivity levels.

7.3.2 ^{222}Rn Monitoring

The ^{222}Rn levels in the purified LS were monitored in order to identify possible air leaks in the system. A contamination with ^{222}Rn in the LS would have increased the concentration of ^{210}Pb in the detector and diminished the effectiveness of the distillation.

A detector, called MiniLAND, was designed by Tohoku University to measure the specific activity of ^{222}Rn in purified LS [71]. The MiniLAND detector was made up of 16 separate acrylic tanks that were 100 cm $\times$ 22 cm $\times$ 17 cm. Tyvek coating was used to increase the reflectivity and overall light yield. These tanks were stacked in a 4 $\times$ 4 array, which was surrounded by another acrylic layer and a 3 mm thick Cu shield. These inner layers were purged with N_2 gas to remove ^{222}Rn and surrounded by a 15 cm thick Pb shield to reduce external backgrounds. The MiniLAND system used coincidence tagging of the ^{214}Bi-Po daughters in LS samples to reach a sensitivity of about 10 mBq/m^3 for ^{222}Rn.

Since the MiniLAND detector was immobile, it could only sample LS from two feed lines from the distillation system. One of these lines came from the final mixing tank and the other attached to piping after the N_2 purge towers. Another more mobile device was set up, as mention in Chap. 7.2, which utilized an electrostatic collection of ^{222}Rn followed by counting of their decay alphas. This device was a gas phase detector that used N_2 as a carrier gas to collect ^{222}Rn on a cold trap, and could sample many different LS flow lines and perform leak tests. The detector required about 1 liter of LS and had a sensitivity of 10 mBq/m^3.

7.3.3 PPO Concentration and LS Density Monitoring

Measurements of the purified LS density were made routinely, especially after any distillation system downtime for maintenance. The density of the LS was monitored at 15°C using a commercial density meter having an accuracy of 0.008%. LS samples could be taken from any of the distillation system sampling ports and injected into the meter. The density measurements were used as a cross-check for purification system readings. In order to maintain proper LS composition and reduce costs, the PPO concentration had to be carefully monitored. This was done by a gas chromatograph

system located offsite at Tohoku University. The system utilized the ratio of the integrated mass peaks of the LS components compared to control samples made with known concentrations of each component. The system was able to determine the PPO concentration to within 1% accuracy.

7.3.4 Light Yield Monitoring

It is important that the LS emits light after going through the purification process. The light yield (quantified as the number of photons emitted per MeV energy deposit) can be affected by many different variables, such as oxidation during heating, change in PPO concentration, or impurities. The light yield of the purified LS was therefore monitored on a regular basis before filling back into KamLAND. This was another responsibility of our group.

During the first phase the light yield was measured using a rather simple detector, consisting of a single 2-inch PMT and a ^{60}Co disk source. The LS samples were filled into small 125 cm^3 counting bottles, which were coupled to the PMT. The ^{60}Co source was placed on top of the bottle and the average charge of the Compton edge was measured using a CAMAC Fan In/Out, discriminator, and charge sensitive ADC. Changes in the light yield could be obtained from variations in the Compton edge positions in the ADC channel spectrum. Samples of purified LS were compared to a control sample. The detector was capable of detecting changes in light yield of 3% magnitude.

A plot of the mean Compton edge charge, in units of ADC channels, for measurements performed through the first purification phase is shown in Fig. 7.2. The data are plotted relative to the control sample, represented by the horizontal dashed line with its 3σ error regions in green. The control sample was taken directly from KamLAND before purification. The error bars include the statistical and 3% systematic

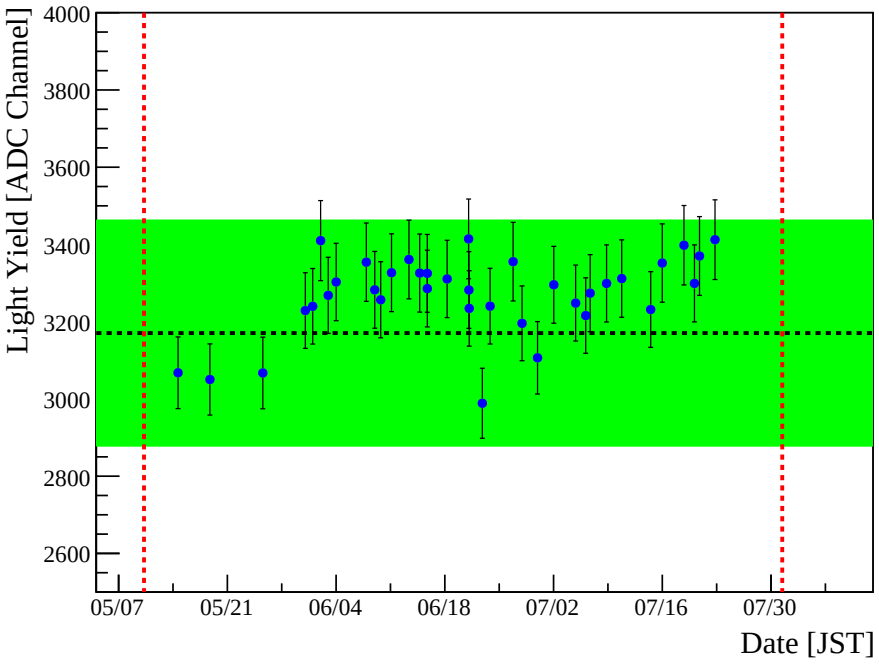

Figure 7.2: Compton edge measurements with a ^{60}Co source using samples of LS from the distillation system during the first phase of purification. The horizontal dashed line represents the control sample measurement and the green regions are the 3σ errors. The vertical red lines indicate the beginning and end of the first purification phase.

errors summed in quadrature. Using this setup we observed no quantifiable loss in light yield seen over time. This observation contradicted light yield determinations done using KamLAND data.

In response to this a new, more sensitive, light yield tester was designed in order to reduce the systematic uncertainty to less than 1%. This involved measuring the Compton peak from a ^{137}Cs source using the backscattering method. The setup utilized two 2-inch PMTs directly across from each other optically coupled to an acrylic cell containing the LS sample to be tested. A NaI detector, measuring the Compton scattered photons, was placed at a 90° angle from the PMTs and 14 cm from the center of the acrylic cell. The ^{137}Cs source was centered in the middle of the NaI detector and the acrylic cell. The CAMAC hardware identified coinciding signals

in both PMTs and the NaI detector, removing most unwanted non-scattering events. No decrease in the light yield was observed by this detector during the second phase of purification [72].

7.3.5 Light Attenuation Monitoring

The attenuation of light is another important scintillator property that had to remain intact during purification. The LS volume inside KamLAND is 13 meters in diameter with a 2.5 meter region of buffer oil. This means that the light from a physics event inside the LS has to travel 3 - 15.5 meters to reach the PMTs depending on the event location.

In order to monitor the light attenuation length, a device called the Attenuation Length Emission Spectrometer (ATLES) was set up and operated by the author and fellow UA graduate student, Greg Keefer. The operating principle of ATLES involves shining light of different wavelengths in the form of a narrow beam through different lengths of LS and measuring the change in beam intensity. The data was fit to the Beer-Lambert attenuation law to obtain a wavelength dependent attenuation length, $L(\lambda)$, as:

$$I = I_0 e^{-\ell/L(\lambda)} \tag{7.1}$$

where I_0 is the initial beam intensity, I is the final beam intensity and ℓ is the path length of the light through the scintillator. A 5 mm diameter light beam was formed using a fluorescent lamp focused with a lens through a collimator. This beam passed through a wheel containing narrow bandwidth wavelength filters (3 - 10 nm FWHM) allowing the user to select one of 11 different wavelengths of light ranging from 300 - 550 nm. The beam of light at a chosen wavelength was passed down the center of a steel column about 1.2 meters in length, which was filled to different heights with LS.

This column was lined on the inside with a black plastic coating to absorb stray light scattered off the beam. After passing through the LS column, the beam was passed through a light guide attached PMT which measured the beam intensity.

Changes in the intensity of the fluorescent lamp over the coarse of the measurement were monitored by reflecting the light through an optical fiber to the PMT. The light input intensity was measured to be stable to within 2%. The dark current from the PMT was determined by completely blocking the beam from passing down the column. The dark current was on the order of 10^{-12} A compared to a typical PMT currents of order 10^{-9} A produced by the same beam.

The measurement process was controlled through LabVIEW interaced with a micro-controller which was responsible for changing the bandwidth filters, raising or lowering the LS in the column, and reading the PMT current. The interface would cycle through 20 different LS liquid heights inside the column, with readings being taken at each height. A single exponential function was fit to the measured current plotted over distance in order to obtain the attenuation length. The attenuation lengths measured were reproduceable to within 1%. Since light attenuation is wavelength dependent, separate attenuations were determined for each bandwidth and an effective attenuation length was calculated from the ATLES data:

$$\langle L \rangle = \frac{\sum_\lambda L(\lambda)\ q(\lambda)\ E(\lambda)}{\sum_\lambda q(\lambda)\ E(\lambda)} \tag{7.2}$$

where λ is the wavelength, L is the attenuation length, q is the PMT quantum efficiency, and E is the PPO emission spectrum. This average relates more closely to the average event charges seen in KamLAND as the direct measured lengths.

The effective attenuation length over first phase of purification can be seen in Fig. 7.3. The horizontal line with a 3σ error region is the measured attenuation length for

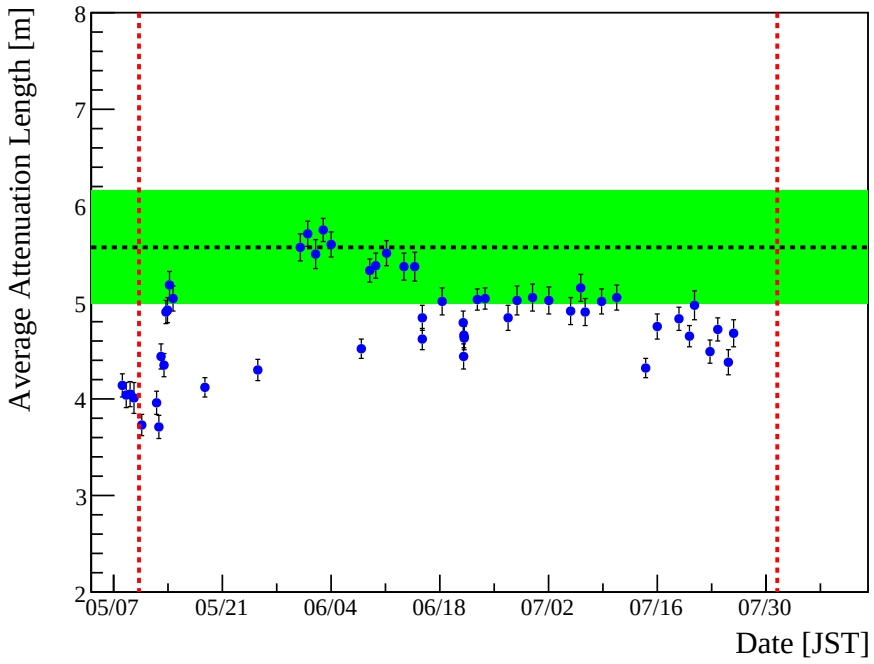

Figure 7.3: Measured attenuation lengths for purified LS during the first phase of purification. The horizontal dashed line with the green 3σ error region is a measurement of KamLAND LS before purification. The red lines indicate the beginning and end of the first purification phase.

a reference sample of LS taken from KamLAND before purification. The errors on the data include both statistical and systematic uncertainties summed in quadrature. The initial low points at the beginning of purification were taken after the distillation system was in self-circulation mode. It was suspected that the Dodecane loses transparency during this operating condition due to oxidation. After this observation had been made the operational procedures were changed such as to minimize the time the LS would spend in self circulation. This decrease was noticed in every measurement taken after a self-circulation period. Overall, no large decreases in the effective attenuation length were seen over both the first and second phases of purification [73].

7.4 Online Monitoring with KamLAND Data

One of the benefits of continuous data taking during the purification process was the ability to monitor the detector properties in real-time. After the first purification phase a slight loss in light yield was noticed in the data, and before beginning the second phase a series of online data monitors were constructed to help alert purification workers to any changes that occured in the detector. This section will outline the online monitor work and purification data analysis performed by the author.

7.4.1 Spallation Neutron Monitor

Monitoring changes in the light yield was done on several different levels. The benchtop measurements of LS coming from different ports in the distillation system were meant as an early warning system to contamination or degradation of the purified LS. Changes in the light yield were also measured using muon-induced spallation neutrons using the KamLAND data.

The principle for tagging spallation neutrons is straightforward. First, a muon passing through the detector is tagged using the criteria stated in Chap. 5.5.1. About 99% of the neutrons produced in the LS capture on H^1, which produce a single 2.22 MeV gamma-ray after a characteristic mean capture time of $\tau = 207.5 \pm 2.8$ μs. After a muon was tagged using the selection criteria from Chap. 5.5.1, all events with a time difference from the last muon of 150 μs $\leq \Delta T \leq$ 1,000 μs were selected in order to observe the neutron capture on H^1 peak.

The spallation neutron monitor would automatically analyze 24 hours worth of data and post updated plots along with any necessary warning messages to an internal website monitored by the purification workers. Both the Nsum and the visible energy of the neutron captures were monitored every day during the second purification phase. Of the two, the Nsum is a slightly more reliable variable for light yield

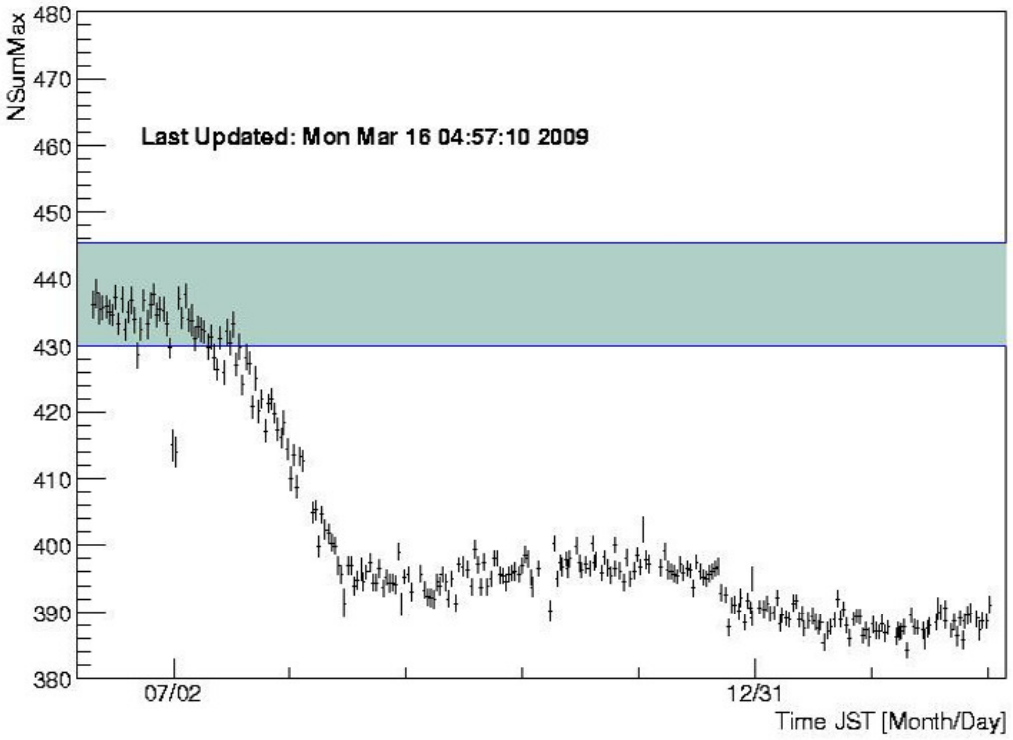

Figure 7.4: Mean neutron capture Nsum values over the course of the second purification phase. The horizontal band is the 2σ error region for the mean neutron capture Nsum before the beginning of the second phase.

monitoring, because the visible energy calculation relies on many parameters that are not always stable. A plot of the mean neutron capture peak Nsum value as a function of time during the second purification phase is shown in Fig. 7.4. The data were collected inside a 5.5 meter fiducial radius, and any changes in the Nsum from variations in the number of dark hits from noise were subtracted off.

A sharp decrease in the light yield was noticed at the beginning of the second purification phase, but this decrease stabilized over time. The exact cause for this decrease is not known, but as stated earlier, could stem from oxidation of the Dodecane during initial self-circulation. The overall decrease in the Nsum value during the first phase of purification was approximately 7% [74], and the decrease during the second phase was approximately 10% [75].

7.4.2 LS Stratification

A critical challenge through the purification process was to maintain stratification of purified and unpurified LS while filling into the detector. An ideal radio-nuclide reduction efficiency could have been achieved in one volume exchange, given that there was no mixing of the purified scintillator with unpurified scintillator. The exact temperature and density required to maintain a clear boundary between the purified LS and the old LS were not known, so the filling process was initially performed through trial and error. With the assumption that the purified LS would have a lower concentration of ^{85}Kr and ^{210}Bi, the boundary between new and old LS was monitored by plotting the vertex distributions of these events in the detector during filling.

The easiest way to observe ^{85}Kr and ^{210}Bi turned out to be using KamLAND data by applying an energy cut, selecting events such that $0.5 \leq E_{vis} \leq 0.9$ MeV. The vast majority of the events in this energy region were ^{85}Kr and ^{210}Bi related and only a small fraction came from other sources. During the second purification campaign, vertex distributions were updated every eight hours and the corresponding plots were posted on webpages that allowed purification workers to monitor the filling process.

The filling of new purified LS into the top of the detector can be seen in Fig. 7.5. In these plots, Z is the distance along the central axis and ρ^2 is the cylindrical radius. These distributions were accumulated in 10-day intervals. The concentration of events increases dramatically near the balloon boundary, this was caused by radio-impurities attached to the balloon surface. The boundary between purified LS at the top and old LS at the bottom can be seen moving down through the detector. A small amount of mixing was observed during filling, where LS began to circulate near the balloon and move inward towards the central regions of the LS volume. This causes three separate layers of different concentrations to appear in the LS volume. During

the second purification phase it was found that filling the detector from the bottom with cooler and denser LS was the better method for obtaining stratification. The largest reduction in the backgrounds was seen during that time.

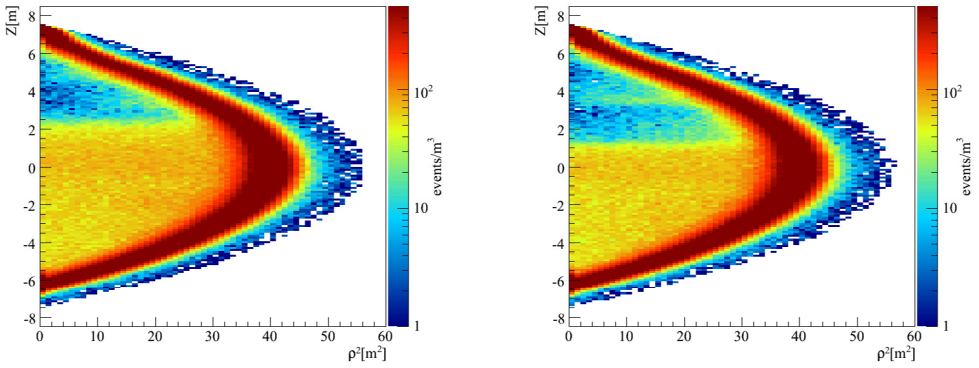

(a)

(b)

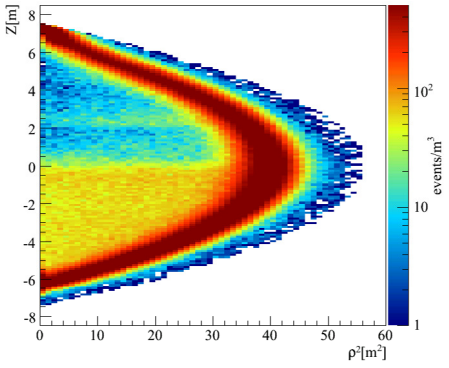

(c)

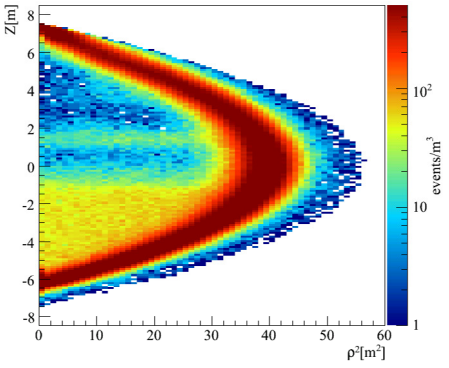

(d)

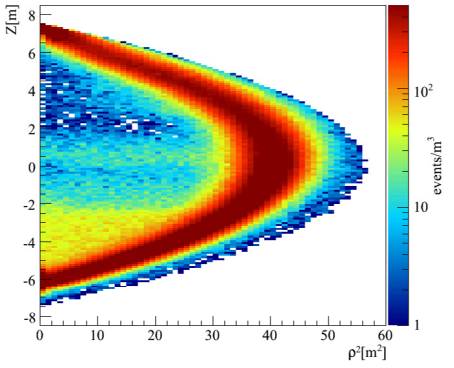

(e)

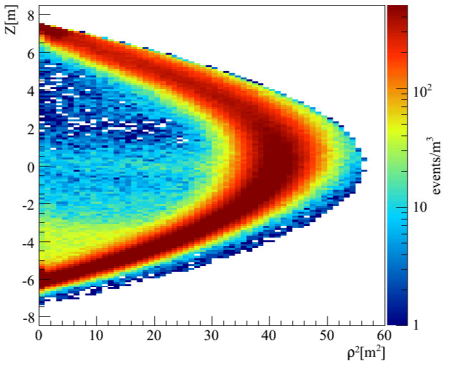

(f)

Figure 7.5: Vertex distributions of ^{85}Kr and ^{210}Bi events inside the KamLAND detector during the beginning of the second phase of purification. The distributions were accumulated in 10-day intervals where the purified LS can be seen moving down the detector.

Chapter 8

A Monte Carlo Simulation of the Backgrounds

After purification, the radioactivity induced backgrounds had decreased substantially inside the fiducial region of the balloon. Following the end of the second purification campaign, a variety of calibration sources were deployed into the newly purified scintillator in order to determine the detector response. The dramatic reduction in the backgrounds provided a new look into the shapes of the spectra produced by gamma sources at low energies. Data from the ^{203}Hg and ^{137}Cs sources taken on March 11, 2010 and September 29, 2010, respectivley, are shown in Fig. 8.1. Careful observation of the shape of the gamma peaks reveals a non-Gaussian tail at higher energies. The tail effect seen in calibration data is a background concern considering that ^{210}Po, one of the largest backgrounds in the ^{7}Be solar neutrino energy window, was always assumed to have a Gaussian shape in previous spectral fits. It became clear that a proper spectral fit required an understanding of the non-Gaussian detector response and any possible variations it could have as a function of energy and position inside the detector. A detailed Monte Carlo simulation of the detector provides a tool for studying the detector response and any effects it may have on the solar analysis.

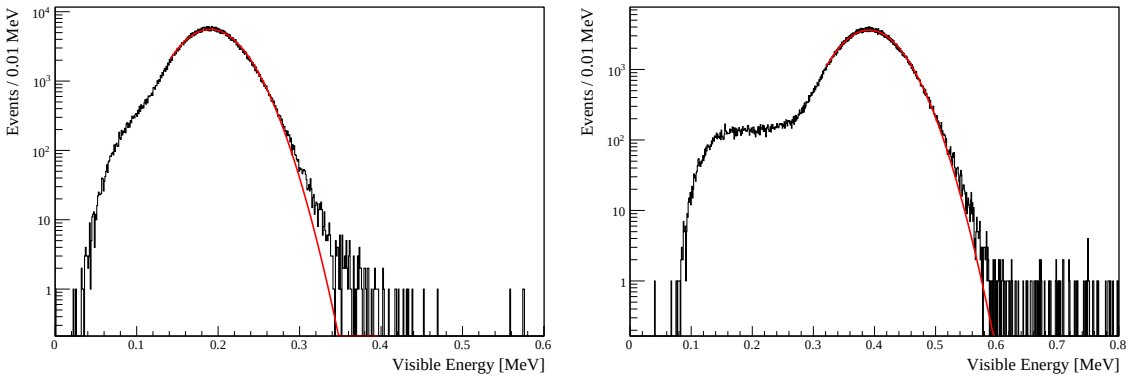

(a) (b)

Figure 8.1: Gauss fits of the ^{203}Hg gamma source (deployed on March 11, 2010) shown in (a) and for the ^{85}Sr gamma source (deployed on September 29, 2010) in (b). The Guass fit function begins to deviate from the source data at higher energies. This effect is noticeable at energies of less than 0.5 MeV where the solar data is dominated by the ^{210}Po background.

8.1 The GEANT Software Toolkit

GEANT is a software toolkit developed for the simulation of particles passing through matter and has been a vital resource for physicists in a wide range of fields, from nuclear and particle physics to medical and space sciences. The modern-day version of this toolkit is called GEANT4 and was designed to adapt object-oriented programming methodology via the C++ language. The design is driven by the needs of todays experiments for a simulating component in their software systems. The most important constituents in the toolkit are the following:

- materials and geometry
- particle interactions in matter
- tracking
- digitizing and hit management

- event and track management
- visualization
- user interfacing

Each of these consituents form a "class" category with separate responsibilities within the framework. The user can call these classes as needed or assign their own software components inside the framework.

The geometry classes give the user the capability of creating detector components of various materials and shapes. The materials can be chosen from a single element or mixture of elements. The elements are made from isotopes and their physical properties can be given directly or, in some cases, can be derived from the isotope composition. The detector components can have sensitive elements assigned to them that record hits and allow the digitisation of detector responses. The readout of hit information allows the handling of pile-up from simultaneous hits from events within a given time frame.

The particle generation within the simulation can be done internally or externally. The behavior of particles inside the simulation is governed by a comprehensive library of physics processes. There are different ways to implement physics processes or modify them as needed. The classes for tracks and steps for events inside a geometry are used by processes to make decisions on how to implement physical interactions.

The visualization classes allow the user to see in real-time the detector geometry, the particle trajectories, tracks and hits, and can provide valuable insight on how the simulation is prepared and executed. The visualization can take place through a variety of viewers, some which have user interfacing to allow manipulation.

An in-depth review of the architecture and implementation of the GEANT4 toolkit can be found in Ref. [76].

8.2 GLG4sim and KLG4sim

The KamLAND detector simulation was initially constructed in 1999 by Glenn Horton-Smith and Haruo Ikeda, and received notable contributions between 1999 and 2004 from Steven Dazely, Jason Detwiler, Lauren Hsu, Toshiyuki Iwamoto, Kevin McKinney, Diane Markoff, Dipanjan Ray, Ryan Rohm, Osamu Tajima, Brian Tipton and Yoshi Uchida. The external radioactive decay generators utilized by the simulation were developed by Andreas Piepke. The simulation was given the name KLG4sim, which stands for KamLAND GEANT4 simulation. It was designed specifically for the KamLAND experiment, but many of the classes were generic enough to be extended to simulate physics events in any liquid scintillator anti-neutrino detector of any geometry. This generic extension is called GLG4sim, or Generic-LAND GEANT4 simulation, and is currently being used by other experiments like the reactor neutrino experiment Double Chooz.

The geometry of the detector was designed to be as accurate as possible. The dimensions for the size and thicknesses of the balloon, ropes, acrylic sphere, PMTs, steel sphere and outer detector were made to be as accurate as possible. The calibration devices were made for accurate representation of calibration deployments in KLG4sim. Careful attention to detail was given building the curvature of the PMTs as specified by Hamamatsu. This was done using a class called GLG4TorusStack, where series of tori of different radii and thicknesses are stacked upon one another to form a smooth curved surface that is not exactly spherical. Various pictures of the detector (views from outside and inside) and its components are shown in Figs. 8.2, 8.3, and 8.4.

A detector like KamLAND requires an adequate model of scintillation light in the detection medium. KLG4sim (and GLG4sim) include such a model in a class called GLG4Scint. The GLG4Scint class gives the user control over how the emission

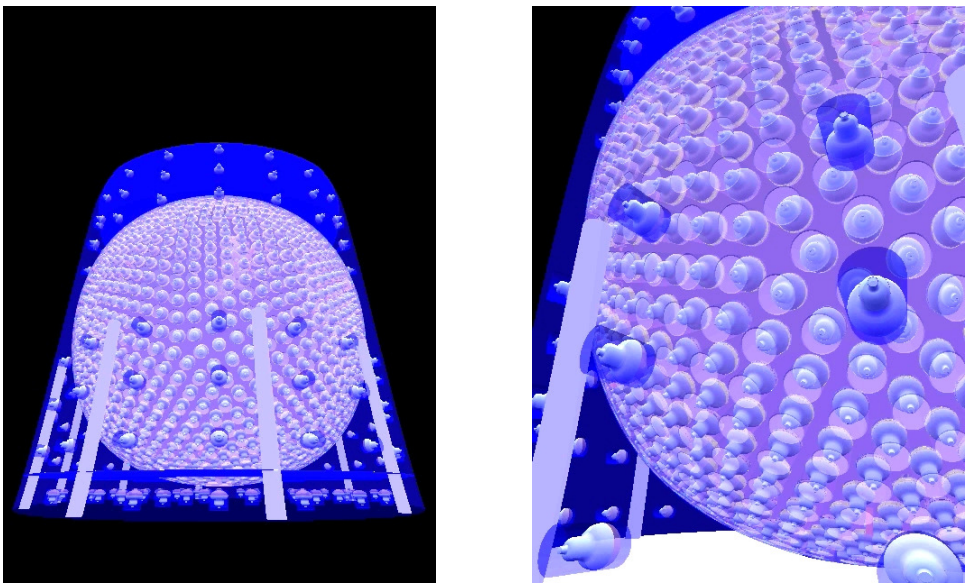

Figure 8.2: Two different views of the outer detector encompassing the inner detector in KLG4sim. The left figure offers a view looking upward at the outer detector and the right figure is a close-up view into the outer detector.

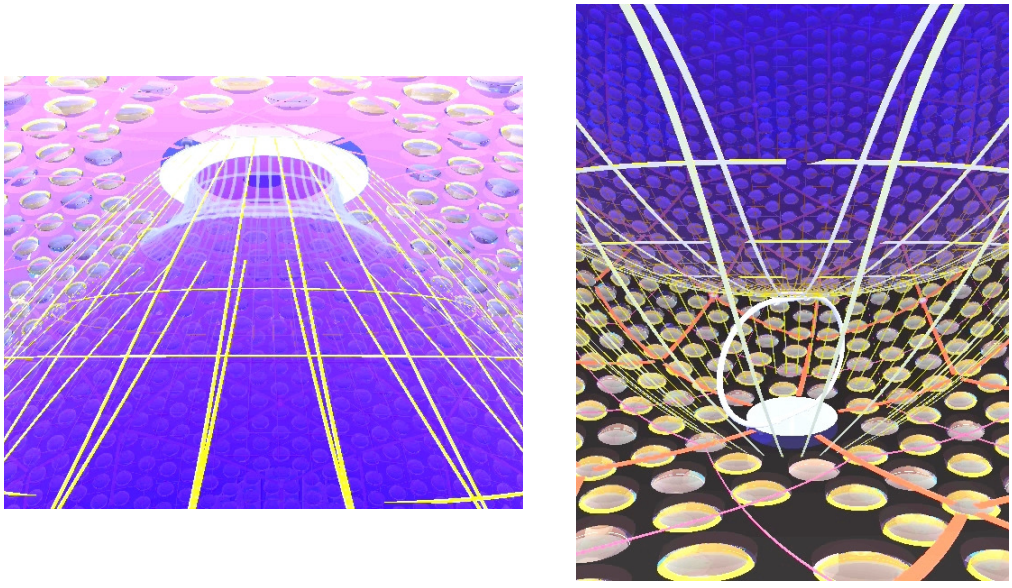

Figure 8.3: Views of the top of the balloon (left) and the bottom of the balloon (right) in KLG4sim. The ropes and support structure holding the balloon can be seen in both figures.

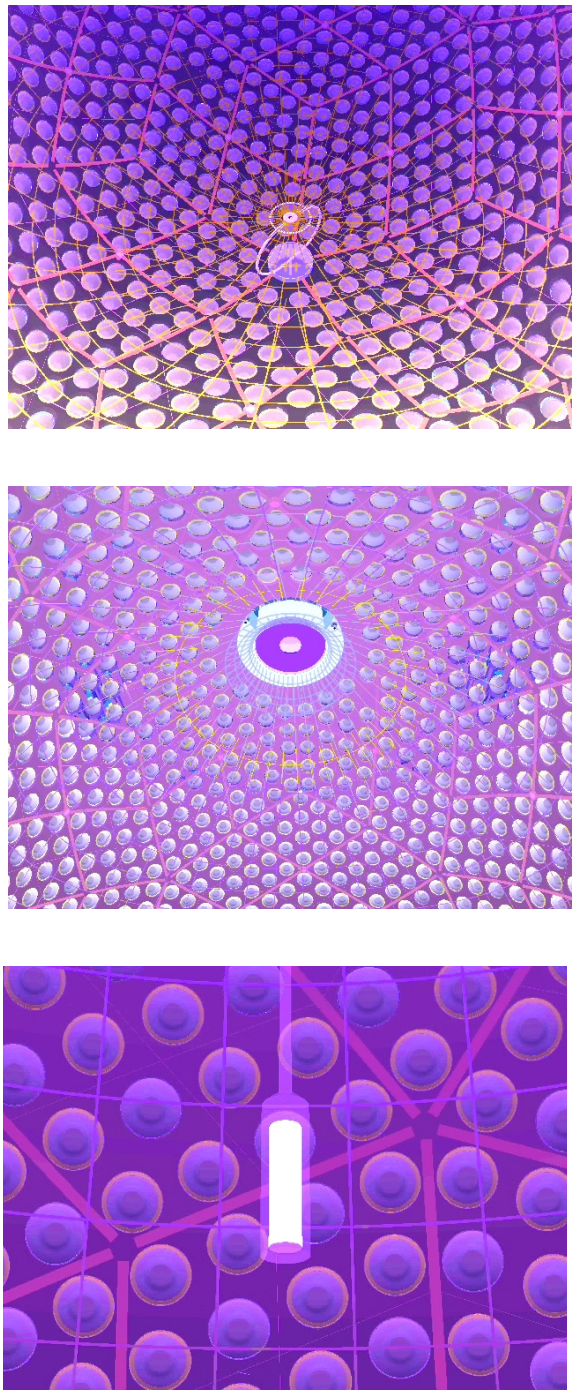

Figure 8.4: Views from inside the balloon looking at the bottom of the detector (top figure), the chimney of the detector (middle figure), and a close-up of a gamma calibration source (bottom figure) in KLG4sim.

of photons through scintillation is performed. The user is allowed to set options such as the maximum number of secondary tracks and the mean number of photons per secondary particle, which allow for faster simulation if the user doesn't require the tracking of every individual photon. The user can control the light yield of the scintillator through the use of an overall scaling factor and create random hits and charge on PMTs due to noise. The ability to turn on/off re-emission is also included. One common property of scintillators is that they have a non-linear response to the ionization density. This means the scintillation light is not proportional to the energy deposited per step, an effect known as "quenching". GLG4Scint calculates the quenched energy, E_Q, by using the first order semi-empirical equation formulated by John Birks:

$$dE_Q = \frac{dE}{1 + k_B \, dE/dx} \tag{8.1}$$

where k_B is known as Birks' constant. This constant must be determined for every individual scintillator [77]. The total quenched energy deposited in the scintillator is then calculated by integrating the individual energy deposits. There is a small amount of Čerenkov light produced in KamLAND scintillator. GEANT4 accomodates this in a separate process class called G4Cerenkov, where the average number of Čerenkov photons is calculated per unit energy interval for a given material using the following equation:

$$\frac{d^2N}{dE \, dx} = \frac{\alpha^2 q^2}{\hbar c^2} \left(1 - \frac{1}{\beta^2 n^2(E)}\right) \tag{8.2}$$

Here, α is the fine structure constant, q is the unit charge, β $(= v/c)$ is the particle speed relative to the speed of light, and $n(E)$ is the index of refraction as a function

of photon energy. The average number of Cerenkov photons per unit step is obtained from an integration per energy deposit interval:

$$\frac{dN}{dx} \approx 370z^2 \int_{E_{min}}^{E_{max}} dE \left(1 - \frac{1}{\beta^2 n^2(E)}\right) \mathrm{eV}^{-1}\mathrm{cm}^{-1} \tag{8.3}$$

The number of photons is then estimated from a Poisson distribution with a mean equal to the step length times the relation in Eq. 8.3.

The photons generated by both G4Cerenkov and GLG4Scint are propagated through the detector medium by both the KLOpAttenuation and G4OpAbsorption classes, which control the scattering and absorption of photons. The scattering of light is controlled by the KLOpAttenuation class and employs Rayleigh scattering. The G4OpAbsorption class allows the user to input the absorption length as a function of photon wavelength.

The PMTs in the simulation have detailed optical modelling to account for the partial reflection, transmission or absorption of the photons through the surface of the PMT glass and photocathode. After the absorption of a photon on the photocathode the quantum efficiency of the photocathode is used to determine if a p.e. is produced. The total number of p.e.'s produced by the PMTs is stored along with the number of PMTs hit and the hit times. All of this information is then stored in what are called RTQ files (in a format identical to real KamLAND data) and used in the reconstruction process.

The KLG4sim output goes through the exact same reconstruction process as the data. During the reconstruction of the KLG4sim output, both charge and time resolution is added based on the folding with a random Gaussian function. The effect on the overall resolution from these smearings is small but necessary for adequate simulation of the energy resolution observed in the data. The reconstructed output is

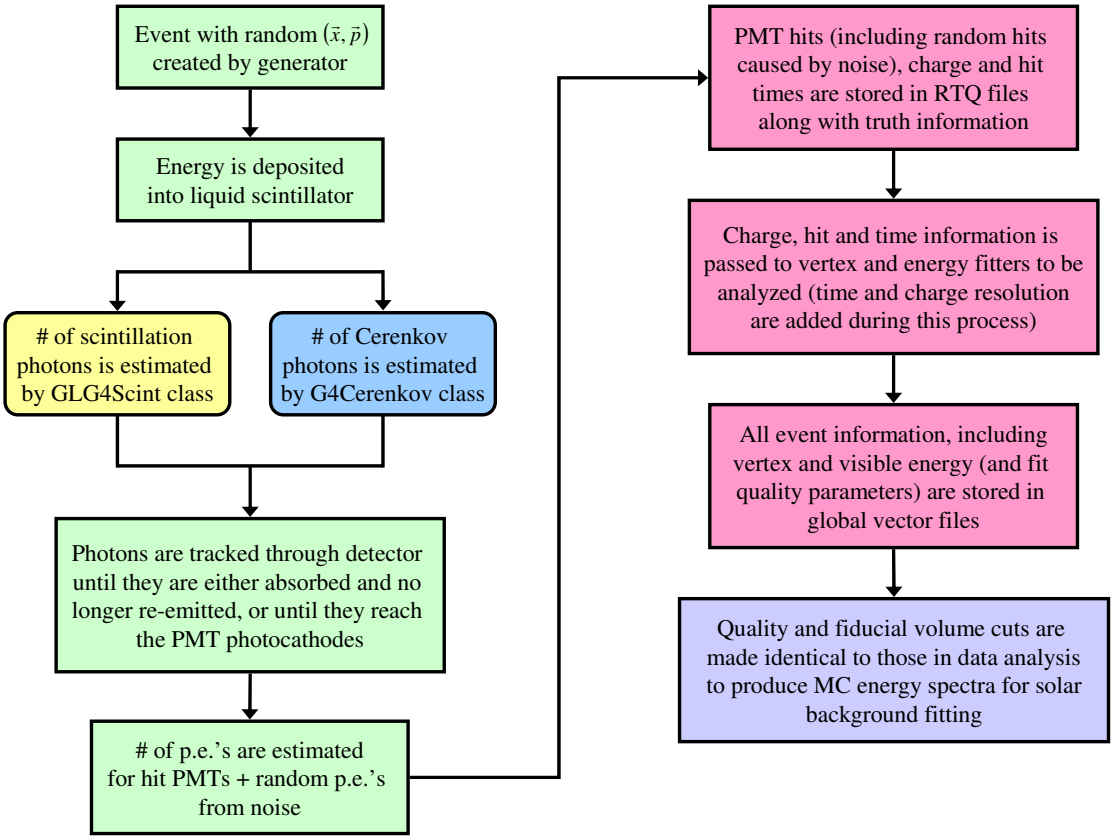

Figure 8.5: A flow diagram outlining the initialization, simulation and reconstruction of a physics events in KLG4sim. The reconstruction processes, in pink, and the quality cuts, in violet, are identical to what is used in the real KamLAND data reconstruction.

stored in global vector files. The global vector files store the reconstructed event information which go through a series of fiducial volume and quality cuts, also identical to what is used in the real data. A flow diagram outlining the steps in the simulation and reconstruction processes is shown in Fig. 8.5.

8.3 Simulating the KamLAND Detector Response

In order to simulate the detector response, four different tunable parameters were utilized to account for the impact of the scintillator purification: light yield, attenuation length, dark noise of the PMTs, and Birks constant. The tuning was performed on a trial and error basis to match the effects seen in KLG4sim output with real KamLAND data mostly collected with calibration sources. This section describes the tuning of each of the parameters using the calibration source data after purification ended, along with the ^{210}Po peak. A quantitative analysis of the deviation of the reconstructed KLG4sim output from the KamLAND data and an estimate of the energy scale uncertainty derived from it are presented in Sec. 8.3.4.

8.3.1 Light Attenuation and Light Yield

The attenuation of light is driven by both scattering and absorption, which are dependent on the wavelength of the propagating light. These parameters are manipulated in KLG4sim by tabulated data input at the beginning of the simulation. A before and after tuning comparison of the changes made to the input data is shown in Fig. 8.6. The fraction of light that undergoes scattering decreased in the 350 - 400 nm wavelength region, where the quantum efficiency of KamLAND PMTs is highest. Overall, the absorption length in the same region decreased slightly, but was increased in the 420 - 600 nm region.

The bulk attenuation was compared between KLG4sim and KamLAND data using a ^{137}Cs calibration source deployment at +5.0 meters z-position in the detector. The charge seen by the PMTs (after subtraction of the estimated charge produced from noise) was plotted as a function of PMT distance. A PMT dependent correction to the charge was made for the solid angle it subtends relative to the source location and for the balloon shadowing, the resulting variable is called the *effective charge*. The

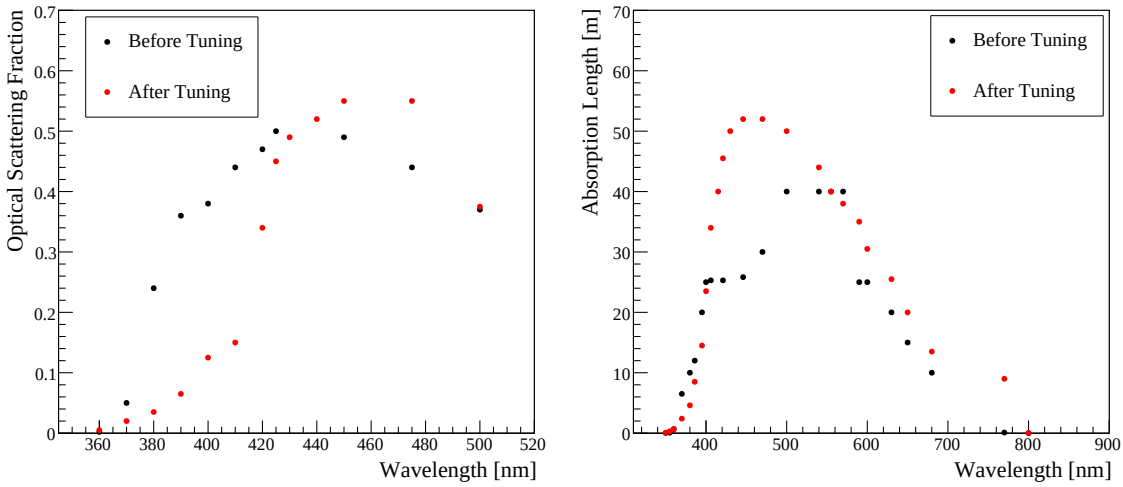

(a) (b)

Figure 8.6: Comparison of the optical scattering fraction, (a), and the absorption length, (b), before and after tuning KLG4sim done to match the data. The changes which had the most impact on the attenuation of light in the scintillator occur between 350 - 400 nm. This is the region where KamLAND PMTs have the highest quantum efficiency.

comparison of simulation (after tuning) and data can be seen in Fig. 8.7, where both the KLG4sim output and the data are fit with a sum of exponentials of the following form:

$$f(x) = A\, e^{-x/\lambda_1} + B\, e^{-x/\lambda_2} \tag{8.4}$$

where x is the distance between the PMT and the source, and λ_1 and λ_2 are attenuation lengths. This function allows for the existence of both a short decay and a long decay in the spirit of a Beer-Lambert absorption law. The attenuation lengths for both KLG4sim and the data are the same within their 1σ error intervals. A uniform offset of about 2% remained between KLG4sim and the data.

After tuning the attenuation length, the light yield was adjusted to compensate for the differences in peak positions of the calibration sources positioned at the center of the detector. The light yield of the scintillator is input at the beginning of the

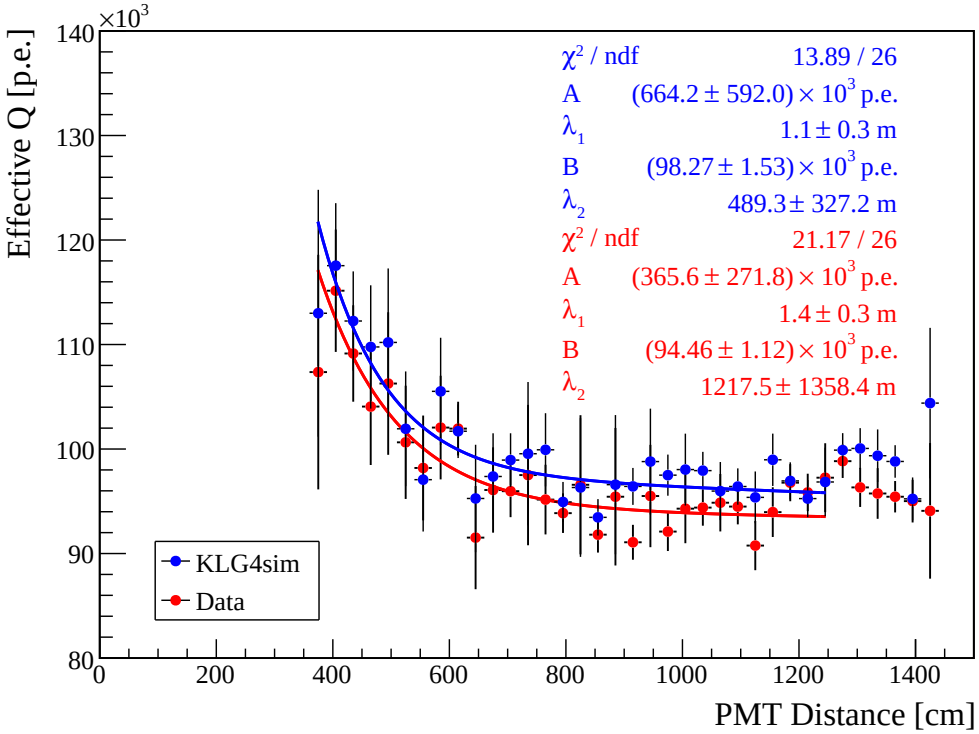

Figure 8.7: Comparison of the bulk light attenuation between KLG4sim and the data. The KLG4sim output is seen to have a uniform 2% offset from the data. The fitted attenuation lengths, λ_1 and λ_2, are the same within 1σ error intervals.

simulation as a single scale factor in units of photons per energy deposit in MeV. Earlier studies with KLG4sim found relatively good agreement with pre-purification data using a light yield of 9,030 photons/MeV, but this factor was acquired using a very simple model for the PMTs that absorbed all of the photons reaching the photcathodes [78]. Using a detailed simulation of the PMT optical properties, a light yield of 7,404 photons/MeV was found to provide a much better agreement between KLG4sim and KamLAND data. A comparison of the visible energies of the full absorption peaks for the calibration sources between KLG4sim and the data can be seen in Fig. 8.8. The amplitudes of the KLG4sim spectra, shown in the figures, are normalized and fit to the data for the ^{203}Hg, ^{85}Sr and ^{137}Cs sources. The shapes of the spectra in the high-energy tail regions are in relatively good agreement, but

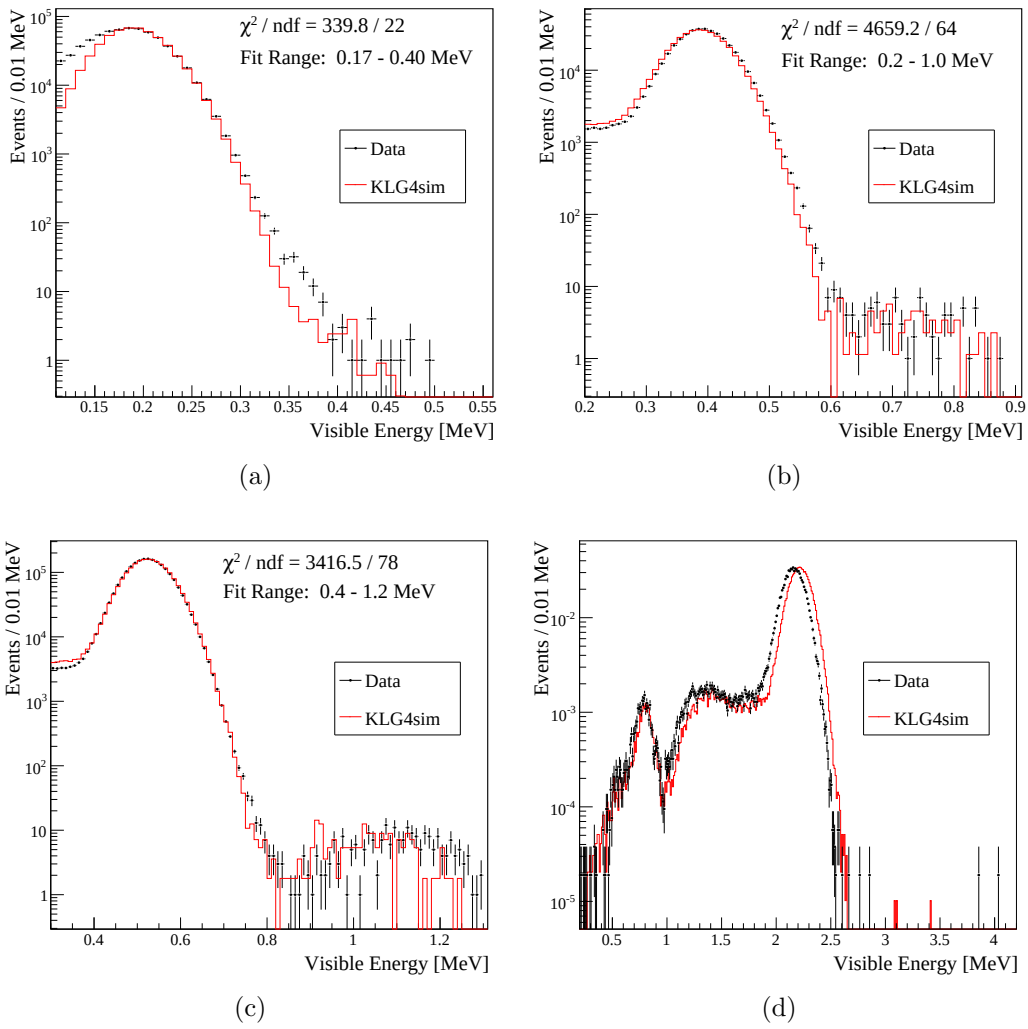

Figure 8.8: Comparison of the energy distributions for the ^{203}Hg, ^{85}Sr, and ^{137}Cs sources ((a), (b), and (c), respectively). The amplitudes are fit with the simulated spectra, while the data in the ^{60}Co^{68}Ge source plot in (d) is normalized and overlaid with the simulated spectrum.

the χ^2 values are rather poor due to deviations in the mean position of the peaks. The ^{60}Co^{68}Ge data has the KLG4sim spectrum overlaid. There is a noticeable excess of events above the KLG4sim spectrum in the 0.3 - 0.4 MeV region of the ^{203}Hg calibration data which doesn't appear in the other source comparisons. The exact cause of the excess is unknown.

8.3.2 Birks Constant and Quenching

In order to adjust the quenching model, a user-defined Birks constant is input into the simulation. The tuning of Birks' constant was performed using the ^{210}Po alpha line, which dominates the background at energies below 0.4 MeV. A series of ^{210}Po alpha simulations were performed scanning a range of Birks constants. It is important to note that the vertices and momenta of events in KLG4sim are produced independently by external event generators, uniform and isotropic distributions were chosen. The simulated spectra were passed through the same fiducial volume cuts used for the solar data analysis, which are detailed in Chap. 9. Each spectrum was fit to the ^{210}Po alpha peak in the data. The best fit of Birks' constant was found to be 0.127 mm/MeV. The result of this optimization is shown in Fig. 8.9. The fit was performed within the 0.24 - 0.30 MeV energy region, where the effects from other backgrounds, such as ^{14}C, ^{85}Kr and ^{210}Bi, are less than a few percent of the total events.

Earlier tuning studies performed by the author also tried to utilize the alphas from ^{214}Po and ^{212}Po, which have visible energies in the KamLAND data of 0.62 and 0.51 MeV, respectively. Attempts to find a Birks constant consistent with all three alphas failed, since the ^{214}Po and ^{212}Po alphas require a Birks constant value which is about 8.5% lower than the best fit value for ^{210}Po. A comparison of the quenching for all three alphas using two different Birks constants is shown in Fig. 8.10. The KLG4sim alphas with a best fit Birks' constant of 0.127 mm/MeV is shown in red and the KLG4sim alphas with a Birks constant of 0.116 mm/MeV are shown in blue. One explanation for this inconsistency is that the 1st order Birks model used in KLG4sim is inadequate for the simulation of alpha quenching, and requires a second order term:

$$dE_Q = \frac{dE}{1 + k_B\ dE/dx + k_C\ (dE/dx)^2} \tag{8.5}$$

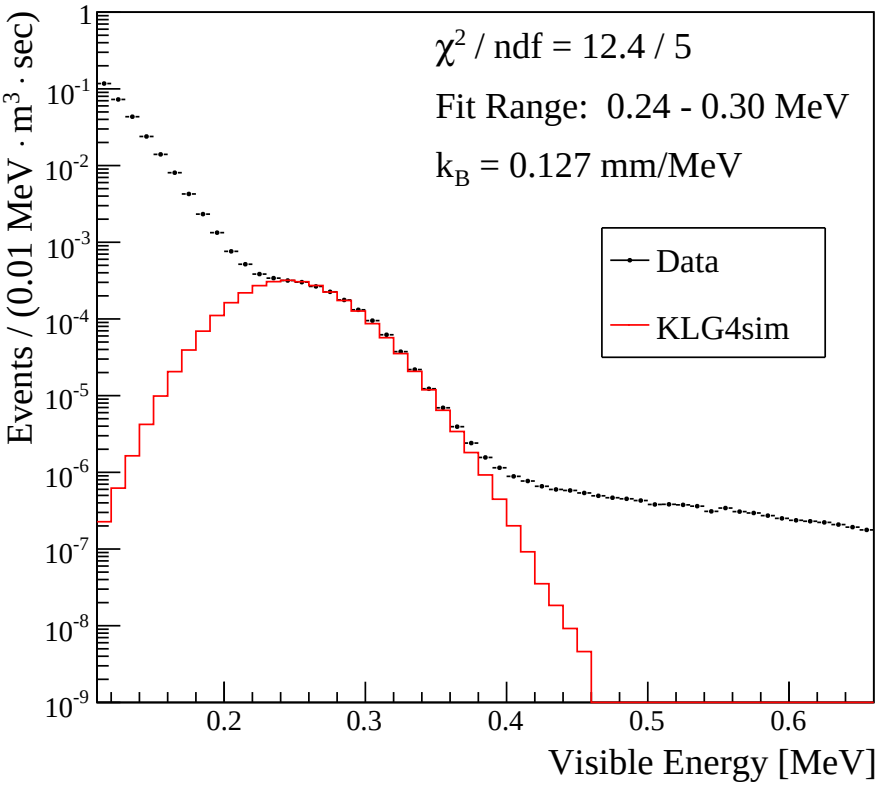

Figure 8.9: Determined best fit of the simulated ^{210}Po alpha peak to the KamLAND data using a Birks constant of 0.127 mm/MeV.

where k_B and k_C are the 1st and 2nd order constants [79]. This would allow greater freedom in the quenching model and possibly resolve the inconsistency between the visible energy of alphas in KLG4sim and KamLAND data. In terms of solar data analysis, the only background spectrum that strongly depends on Birks constant is the ^{210}Po alpha, because the rest of the backgrounds are made up of betas and gammas. Therefore, the best fit Birks constant of 0.127 mm/MeV was used during the simulation of the background spectra.

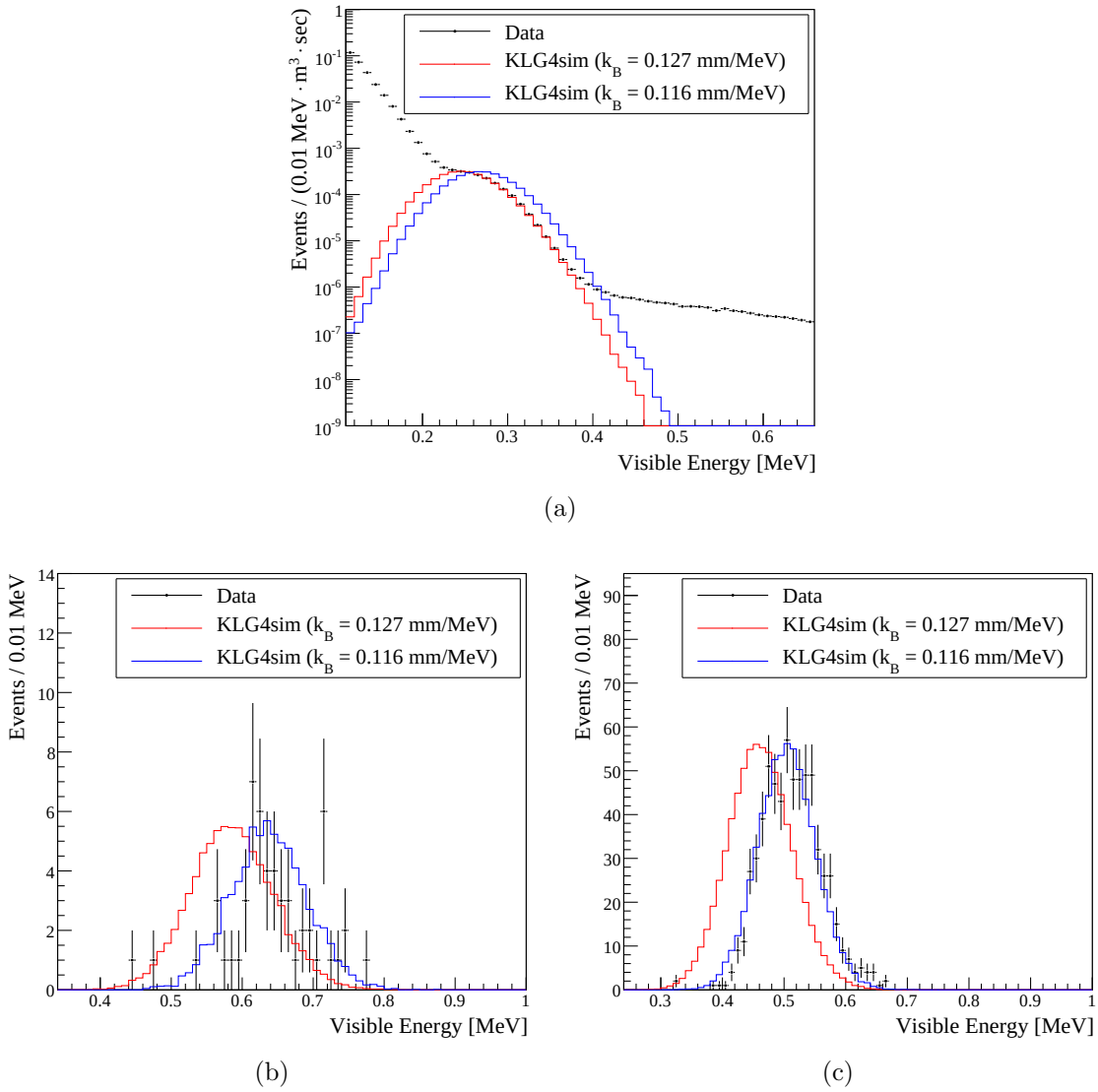

Figure 8.10: Effect of using different Birks constants in KLG4sim when simulating alphas. The ^{210}Po alpha, shown in (a), agrees with the data for a Birks constant of 0.127 mm/MeV plotted in red. However, the ^{212}Po alpha shown in (b) and the ^{214}Po alpha shown in (c) have much better agreement with the data for a Birks constant of 0.116 mm/MeV plotted in blue. The data shown in (b) for ^{212}Po has rather poor statistics due to the very low ^{220}Rn activity in the LS after purification.

8.3.3 Reproduction of Beta Spectra

Almost all of the relevant background spectra in the solar data analysis are beta induced. Therefore, it is essential to have verification that the energy shape of beta spectra simulated in KLG4sim are accurate.

A beta spectrum that can be isolated in the data with adequate statistics comes from the decay of ^{214}Bi, it contains a variety of gamma decays. As mentioned in Chap. 6.1.2, these decays are tagged using the fast coincidence with the ^{214}Po alpha decay. The decays of ^{214}Bi were simulated using the optical parameters determined with the radioactive calibration sources and the ^{210}Po alpha peak, and were passed through the solar fiducial volume cuts. A fit of the simulated ^{214}Bi spectrum to the KamLAND data can be seen in Fig. 8.11. Based on the quality of the fit which spans from 0.4 - 3.2 MeV, the ^{214}Bi beta spectrum was reproduced rather well in KLG4sim. The KLG4sim tuning was performed using point sources, and thus, localized energy deposits, while the ^{214}Bi events are spread all over the detector. The good agreement of KLG4sim with data shows that KLG4sim averages well over the entire detector.

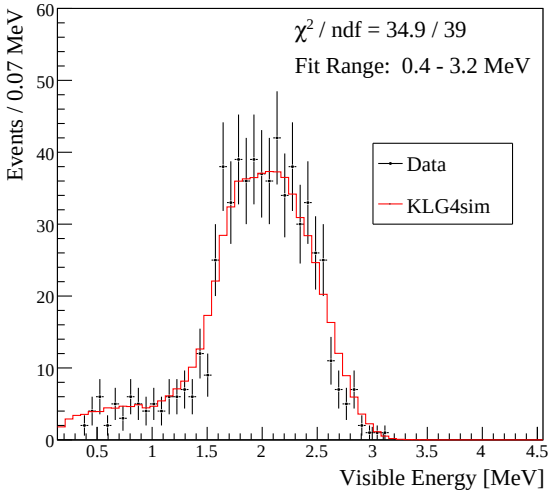

Figure 8.11: Fit of the simulated KLG4sim ^{214}Bi beta spectrum to the coincidence-tagged ^{214}Bi events in the KamLAND data.

8.3.4 Reconstruction Uncertainties

After completing the tuning of the light model of KLG4sim, possible biases and systematic uncertainty of the energy scale was quantified. Inadequacies in the energy calculation of KLG4sim will cause deviations in the shape of the spectra from expectation. When used in the solar neutrino analysis, the energy uncertainty will impact the solar neutrino flux determination. This is evaluated in Chap. 9.

Vertex reconstruction biases when comparing source data and corresponding KLG4sim calculations. To allow such comparison, the calibration sources were deployed in 1 meter increments from Z = -5 meters to Z = +5 meters and then compared to the corresponding simulation. The bias in the Z-coordinate, ΔZ, is defined as:

$$\Delta Z = Z_{\mathrm{Data}} - Z_{\mathrm{MC}} \tag{8.6}$$

where Z_{Data} is the mean reconstructed event Z-position determined for the KamLAND data and Z_{MC} is the mean Z-position determined with KLG4sim. A summary of the vertex bias along the Z-axis is shown for all the sources in Fig. 8.12. Typical fiducial volume cuts in solar data analysis use events between Z = -4.0 meters and Z = +1.0 meters. For these locations a typical vertex bias of -5.0 cm $< \Delta Z <$ +5.0 cm was found for energies below 1 MeV.

To estimate the bias and uncertainty in the energy scale, the percent differences between the reconstructed mean visible energy of the calibration sources for KLG4sim and KamLAND data were used. Defining E_{Data} as the mean reconstructed energy of the data and E_{MC} as the mean reconstructed energy of KLG4sim, the energy uncertainty, ΔE, is given as:

$$\Delta E = \frac{E_{\mathrm{Data}} - E_{\mathrm{MC}}}{E_{\mathrm{Data}}}. \tag{8.7}$$

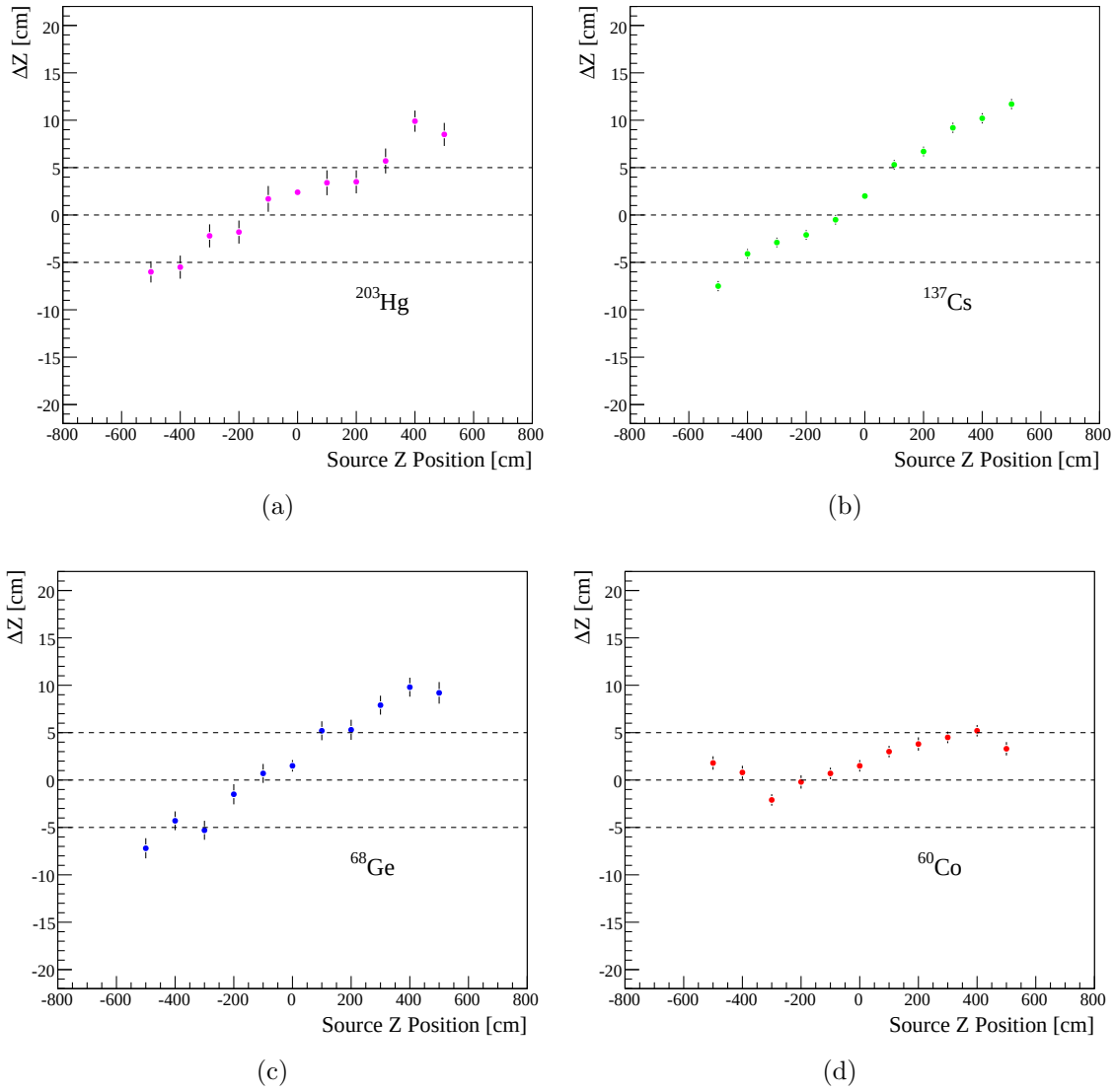

Figure 8.12: Reconstruction bias between KLG4sim and KamLAND data for the calibration sources. Typical fiducial volume cuts for the solar data analysis use events between Z = -4.0 meters and Z = +1.0 meters, where the bias is approximately -5.0 cm $< \Delta Z <$ +5.0 cm.

The energy bias is plotted in Fig. 8.13 as a function of the KLG4sim mean visible energy. The error bars shown in Fig. 8.13 are a combination of the statistical and systematic errors summed in quadrature. The energy bias increases exponentially at lower energies. This is probably due to the inconsitency of the light model in KLG4sim discussed above. The uncertainty in the energy scale is identified as the error of the fit. The correlations of the fit parameters are discussed in Chap. 9.4.1. The spectral fits used in the final solar neutrino analysis have a lower bound of 0.4 MeV, where the energy bias is approximately 1%.

The bias in the resolution between the KamLAND data and KLG4sim was also characterized in a similar way. The percent deviation between peak resolution in the data and KLG4sim was calculated for the calibration sources in the following way:

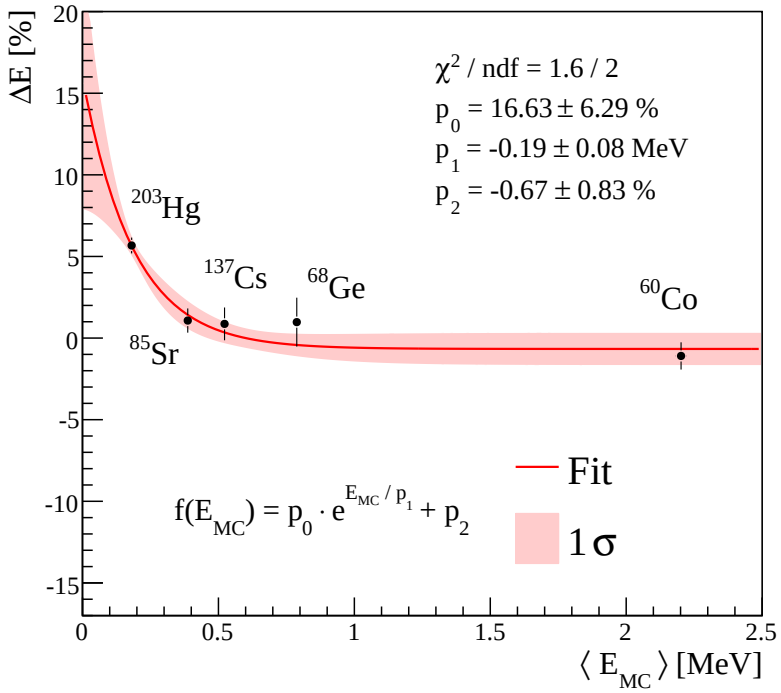

Figure 8.13: Energy bias with the 1σ uncertainty region plotted as a function of the KLG4sim mean visible energy.

$$\Delta\sigma = \frac{\sigma(E_{\mathrm{Data}})/E_{\mathrm{Data}} - \sigma(E_{\mathrm{MC}})/E_{\mathrm{MC}}}{\sigma(E_{\mathrm{Data}})/E_{\mathrm{Data}}}. \tag{8.8}$$

where $\sigma(E_{\mathrm{Data}})$ is the resolution of the data and $\sigma(E_{\mathrm{MC}})$ is the resolution of KLGsim. The energy resolution bias is plotted as a function of KLG4sim mean visible energy in Fig. 8.14. The errors include statistical and systematic uncertainties summed in quadrature. A large error is seen for the ^{68}Ge point due to the low statistics of the data. The points are centered around zero with a positive 2.16% offset as shown from fitting a constant to the data. The uncertainty of the detector model is also defined as the error of the fit.

It is important to note that the energy biases presented here are relevant for gammas and betas. A separate bias was calculated for the ^{210}Po alphas, because the

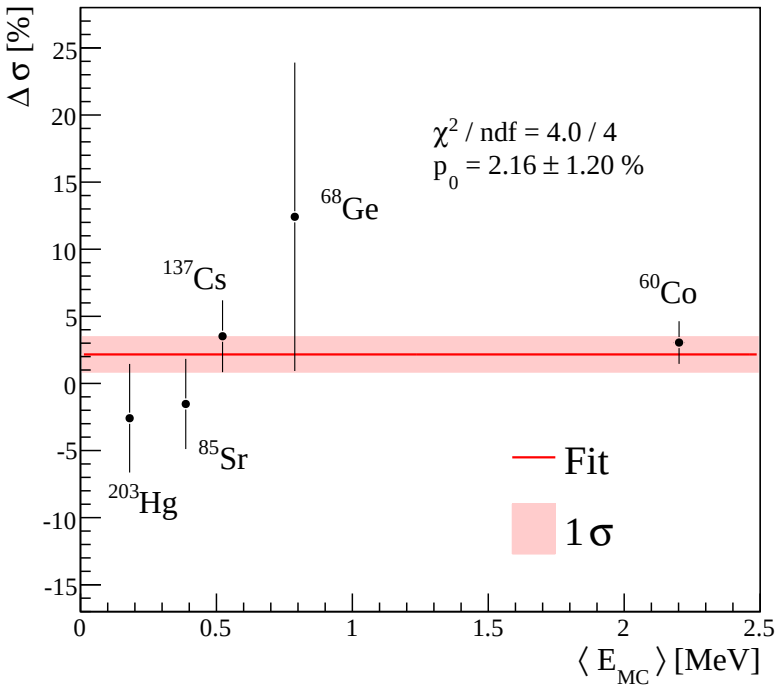

Figure 8.14: Energy resolution bias with the 1σ uncertainty region plotted as a function of the KLG4sim mean visible energy.

detector resolution and quenching is much different for heavy, ionizing particles. In order to independently estimate the energy uncertainty for the ^{210}Po peak, Gaussian fits to both the data and KLG4sim were compared, where the energy fit region was limited to 0.24 - 0.36 MeV for both cases. The energy uncertainty and resolution uncertainty are defined the same way as before, using Eqs. 8.7 and 8.8, respectively. For the ^{210}Po alpha peak, $\Delta E = -0.9 \pm 0.3\%$ and $\Delta\sigma = 5.2 \pm 0.5\%$.

Finally, the initial argument for using KLG4sim to reproduce the backgrounds for solar data was that the shape of calibration source peaks at low energies were non-Gaussian. A Gaussian fit to the KLG4sim ^{210}Po peak in Fig. 8.15 shows clear evidence of a deviation at higher energies. Due to background, the non-Gaussian shape of the ^{210}Po peak in the data cannot be unambiguously observed. However, given the calibration source peak shape comparisons in Fig. 8.8, this effect is also expected to be present in the data. In KLG4sim, the deviation of the ^{210}Po peak from a Gaussian is about 2.6% in the 0.25 - 0.45 MeV region.

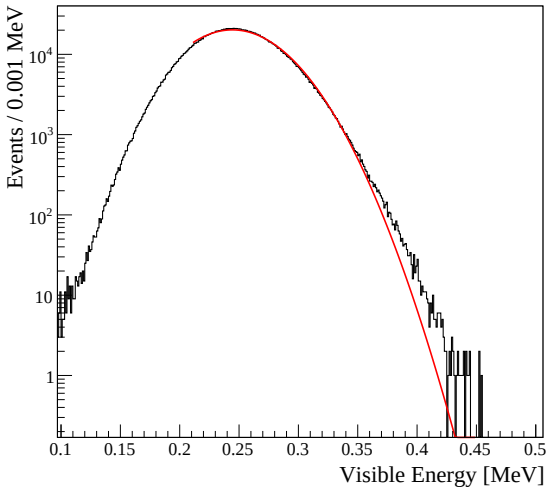

Figure 8.15: A Gaussian fit (in red) to the ^{210}Po peak in KLG4sim showing a 2.6% deviation in the 0.25 - 0.45 MeV region.

8.4 Optimization for ^{7}Be Solar Neutrino Analysis

Fiducial volume cuts are necessary in solar neutrino analysis to reduce the background contribution of external gamma-rays and to select the regions of the detector which have the lowest concentration of radio-imputirites. When running simulations of internal backgrounds in KLG4sim, events were uniformly distributed over the LS volume and the fiducial volume cuts were applied after the data had been reconstructed. This is an inefficient use of CPU time, since a majority of the simulated events will be thrown away after fiducial volume cuts are made. In order to reduce the number of events thrown away, the author constructed an additional fiducial volume within the LS.

To create a volume in GEANT4, the user has to specify a shape using the G4VSolid class, which defines the dimensions of the volume. The geometry of G4VSolid is inherited by G4LogicalVolume, which gives the shape certain material properties. The G4LogicalVolume is then copied to a G4PhysicalVolume in order to position the volume with respect to the world volume in the simulation. The fiducial volume in KLG4sim is a sphere composed of liquid scintillator and is positioned such that the center of the sphere is the center of the detector. The objects in KLG4sim that accomplish this are called *solidFiducial*, *logiFiducial*, and *physFiducial*. All of these objects are located in the KL_ConstructKamLAND class. The user has the ability to input the radius of the fiducial volume by modifying a data file input at the beginning of the simulation that contains all the detector component dimensions.

During the simulation of backgrounds, the fiducial volume in KLG4sim was defined to be 0.5 meters larger in radius than the fiducial volume cuts made during the data analysis. Since the events are given momenta that are isotropic, the extra radial dimension will help model feeding and loss of events within the fiducial volume cut region. The impact of this procedure is immediately evident when comparing the

fraction of events lost for a 4 meter fiducial volume cut on the data. This corresponds to a fractional loss of 0.767 with no KLG4sim fiducial volume and 0.298 with a 4.5 meter KLG4sim fiducial volume. This cuts down the simulation time of a single internal background by a factor of 2.5 from an average simulation time of $\sim$20 hours to $\sim$8 hours and makes such computation feasible in terms of its CPU time consumption.

In addition to the KLG4sim fiducial volume, a procedure taking into account bad PMT channels was implemented for added realism of the model. In the solar data analysis, bad PMT channels are ignored during the reconstruction as explained in Chap. 5.2. Bad PMT channels are determined on a run-by-run basis and are stored in data files so that they can be accessed by the reconstruction algorithm. During any given data-taking run, there are approximately 40 bad PMT channels (out of 1879 total channels). To correctly ignore the same bad channels during reconstruction of backgrounds simulated in KLG4sim, the following steps are taken:

1. The total number of simulated events, N, is passed to the reconstruction algorithm.

2. A table containing all the solar data run numbers, i, and the live times of each run, T_i, are accessed by the reconstruction algorithm.

3. The total number of simulated events is divided into subgroups based on the fraction of live time of each run. Each subgroup contains $n_i = N(T_i/T)$ events, where T is the total live time of the solar data and n_i is the number of events in a subgroup corresponding run number i.

4. Each subgroup of n_i events is assigned the corresponding run number, which allows the reconstruction algorithm to ignore bad channels for the specified run.

This procedure correctly weighs the overall effect of ignoring specified bad channels

for the duration of each data taking run on simulated events. The effect of ignoring bad channels during simulated event reconstruction is not expected to be very large.

8.5 Internal Background Simulations

The simulation of the backgrounds was a rather time consuming task, since most of the spectra required on the order of 10^6 events to accurately estimate the energy shape over several orders of magnitude in amplitude. All of the internal backgrounds were simulated separately with the exception of the ^{210}Po alpha, which was simulated together with ^{14}C to properly model event pile-up. The light model in KLG4sim was fixed using the parameters obtained from tuning which are listed in Table 8.1.

After the simulations finished, the output is sent to the reconstruction process and the final data is stored in ROOT files after applying fiducial volume and quality cuts. The event energies are taken from the ROOT files and filled into histograms with 10 keV bins and the histograms are normalized to unity to create probability density functions. The probability per energy bin is output into text files which are accessed by the fitting algorithms during analysis. The spectral energy distributions calculated by KLG4sim are shown in Fig. 8.16 and Fig. 8.17.

Property	Input Value
Dark Rate Fraction	0.018
Light Yield Fraction	0.82
Birks Constant	0.127 mm/MeV
Cerenkov emission	ON
Re-emission	ON

Table 8.1: KLG4sim input values for the simulation of backgrounds. The dark rate value is defined as the fraction of 1,879 PMTs occupied within a 300 ns time window, and the light yield is defined as the fraction of 9,030 photons/MeV.

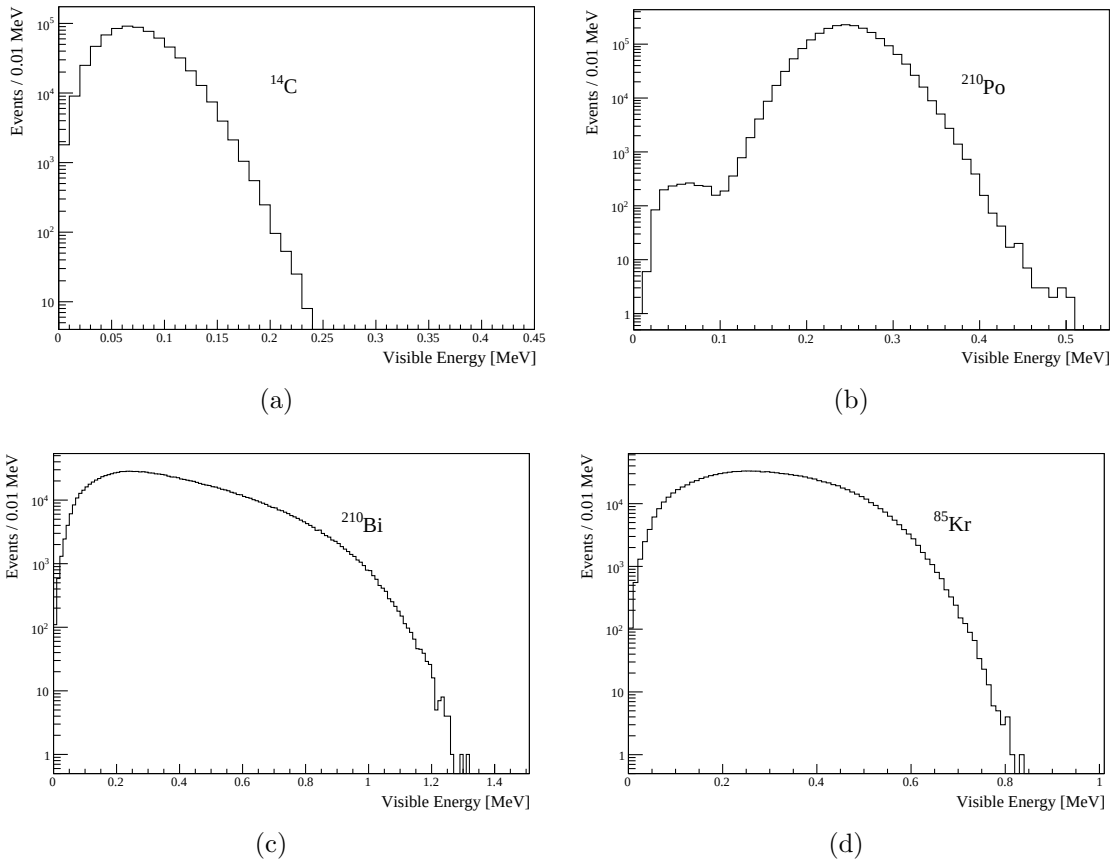

Figure 8.16: Internal backgrounds produced by KLG4sim and used in solar neutrino analysis.

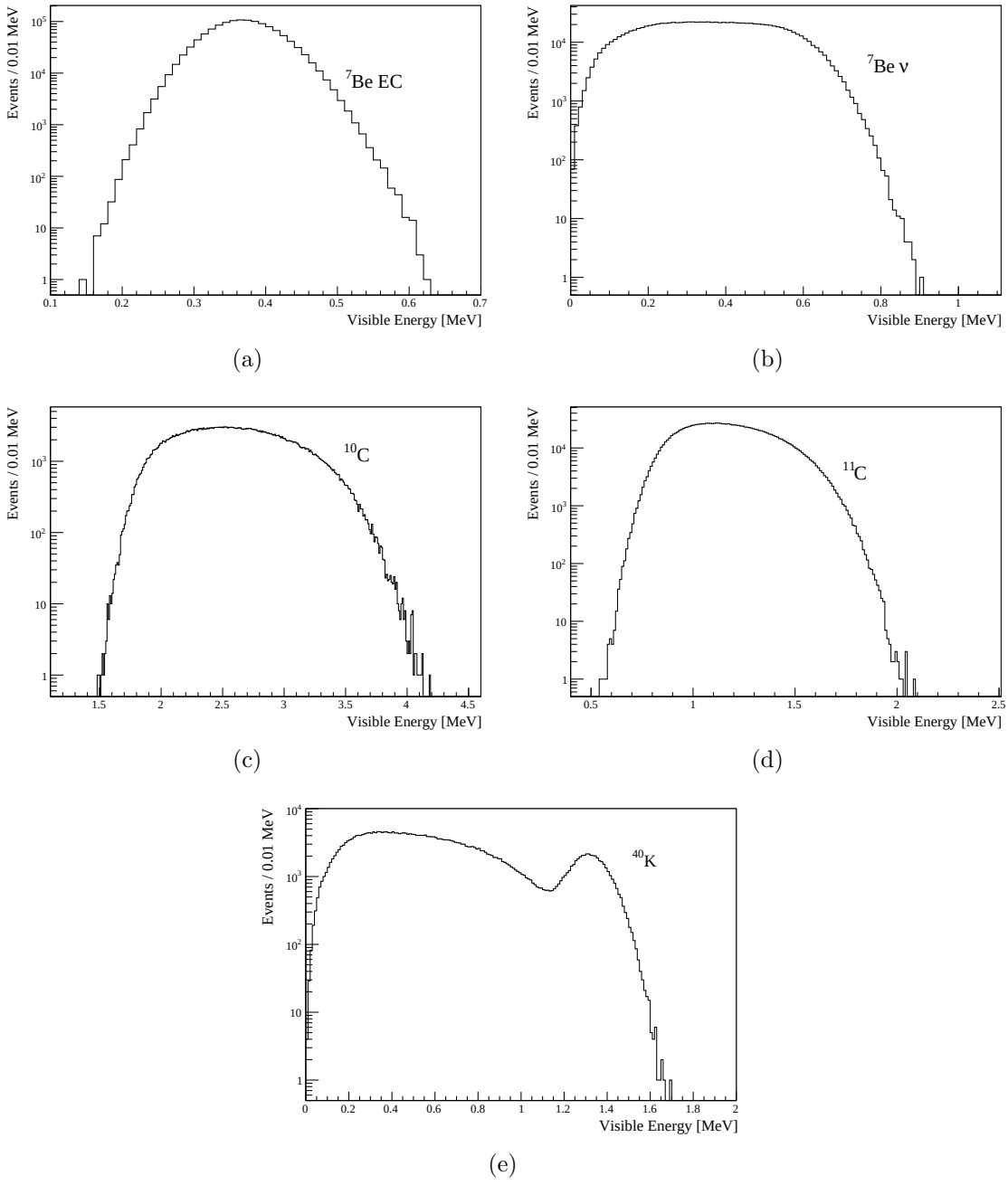

Figure 8.17: Internal backgrounds and ^{7}Be ν recoil spectrum produced by KLG4sim and used in solar neutrino analysis.

8.6 External Gamma-Ray Background Simulations

Detector simulations are a useful tool when modelling backgrounds coming from external detector components, containing trace amounts of ^{40}K, ^{238}U, and ^{232}Th. These radio-impurities emit gammas of different energies which may deposit their energy inside the fiducial volume. The limiting factor in this type of study is the amount of computation time required to track gammas through the detector components and then accurately simulate the detector response for energy deposits in the scintillator. The author has simulated the external backgrounds from several components: the LS balloon, the kevlar supporting ropes, and the PMTs.

Most of the materials used in the construction of KamLAND have been radioassayed in detail via Ge detector counting, neutron activation analysis, and inductively coupled plasma mass spectroscopy [80]. These purity measurements, along with estimates of the component mass, provide total activity inputs into the simulation. The activity inputs for the simulated components are summarized in Table 8.2, where the estimated masses of the components are taken from [81].

In order to compare the number of simulated decays to the external backgrounds rates in KamLAND, a scale factor is needed to constrain the activity measurements by the data. The scale factor, S, is the fraction of decays simulated compared to the number of decays accumulated over the 306.46 days of solar data. The scale factor can be calculated for ^{40}K using the 1.461 MeV gamma peak and for ^{232}Th by using the 2.615 MeV gamma peak from ^{208}Tl. Both of these peaks are visible in the data when looking at the regions of LS near the balloon. Calculating the scale factor for ^{238}U is difficult, since the gamma decays are not intense enough to produce any unique features.

The total live time of the solar neutrino analysis is 306.46 days and is discussed in Chap. 9. A total of $(1.84 \pm 0.02) \times 10^5$ ^{40}K events were observed near the balloon

Component	Mass [kg]	Isotope	Total Activity [Bq]	Decays Simulated
Balloon Film	100	^{40}K	25	4×10^6
		^{232}Th	0.0057	2×10^5
		^{238}U	0.022	6×10^5
Balloon Ropes	80	^{40}K	20	7×10^6
		^{232}Th	0.26	7×10^6
		^{238}U	0.4	11×10^6
PMTs	7200	^{40}K	80	7×10^6
		^{232}Th	470	7×10^6

Table 8.2: KLG4sim inputs for the simulation of external backgrounds on the balloon, ropes and PMTs.

during 1.61 days of KamLAND data, and a total of $(5.66 \pm 0.08) \times 10^4$ ^{208}Tl events near the balloon during 2.57 days of KamLAND data. Out of 11×10^6 simulated ^{40}K decays, $(2.15 \pm 0.01) \times 10^5$ were found in the same region of the balloon used to observe ^{40}K events in the data. Taking the ratio of events near the balloon and multiplying by the ratio of the ^{40}K data live time and the solar neutrino analysis live time gives:

$$S = \frac{N_{KLG4sim}}{N_{Data}} \cdot \frac{1.61 \text{ days}}{306.46 \text{ days}} = 0.0062 \tag{8.9}$$

where $N_{KLG4sim}$ is the number of events near the balloon in KLG4sim, N_{Data} is the number of events near the balloon in the data, and S is the scale factor. The same calculation can be performed for the 14.2×10^6 simulated ^{232}Th decays (using the ^{208}Tl events) and was calculated to be 0.0013. This means that the simulated ^{40}K and ^{232}Th decays sample roughly 0.62% and 0.13% of the total live time for solar neutrino analysis.

All of the simulated decays in Table 8.2 were analyzed using the exact same

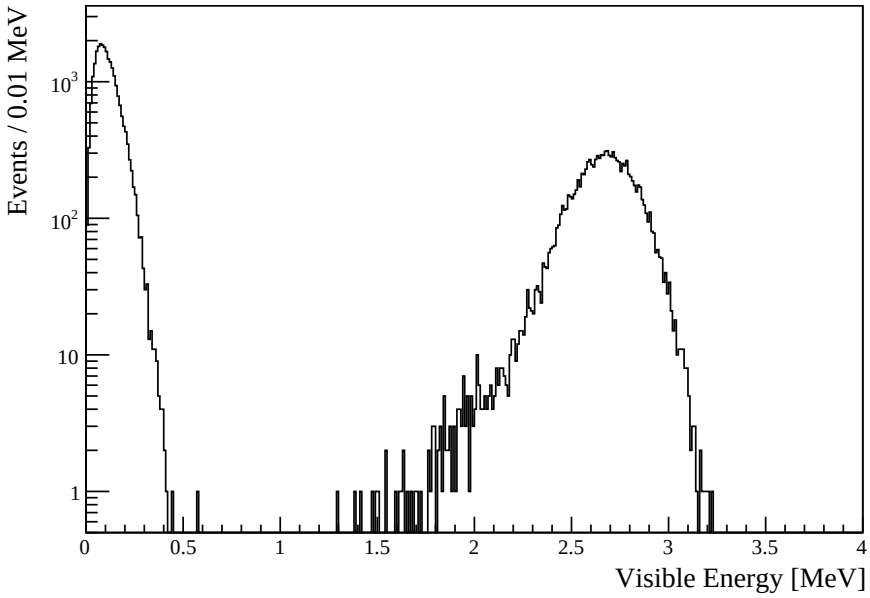

Figure 8.18: Visible energy spectrum inside the solar fiducial volume (4.5 meter radius) from all the simulated decays listed in Table 8.2.

fiducial volume (with a 4.5 meter radius) and event selection cuts discussed in Chap. 9. The visible energy spectrum from the sum of all these decays is shown in Fig. 8.18. For reasons that are explained in Chap. 9.3, the lower bound of the fit region for the energy spectrum in ^{7}Be solar neutrino analysis is 0.4 MeV. The contribution from the external gammas inside a 0.4 - 0.8 MeV window is 5 events, with 3 events coming from ^{40}K and 2 events coming from ^{238}U. Even though a scale factor cannot be calculated for ^{238}U it is still possible to estimate the number of expected decays for a given live time using measurements of ^{238}U activity from the detector components. With the assumption that the only contributions of ^{238}U come from the balloon and ropes, a contribution of 2.3 events from ^{238}U and 438.9 events from ^{40}K are expected during 306.46 days of data taking. These contributions combined make up 0.94% of the 4.72×10^4 the total event contribution within the 0.4 - 0.8 MeV window and are not included in the ^{7}Be solar neutrino analysis.

Chapter 9

^{7}Be Solar Neutrino Analysis

The purification campaign which spanned over two years concluded on February 6, 2009, and the detector began to collect solar data with a highly improved senstivity to ^{7}Be neutrinos inside the 0.2 - 1.0 MeV energy region.

This chapter is devoted to the derivation of the ^{7}Be solar neutrino signal from the data. This work is performed by using calculated KLG4sim spectra discussed in Chap. 8, and is the first-ever KamLAND data analysis using full-detector Monte Carlo simulations tuned below 2 MeV. The fiducial volume cuts used to select the portions of the detector with the highest purity will be presented in detail, and the quality cuts used to select events with accurate energy and vertex reconstruction are also summarized. The leading systematic uncertainties are identified and calculated, and their overall effect on a ^{7}Be solar neutrino measurement is discussed in Sec. 9.4. A summary of the reduction seen in the backgrounds and the implications of this analysis on the SSM prediction is given at the end.

9.1 Fiducial Volume Selection

The procedure for selecting the fiducial volume was determined by the spatial and temporal non-uniformity of the purified LS inside the balloon. Along with the non-uniform purity content, the LS volume was not static due to changes in the temperature gradient of the inner detector over time. These changes caused mixing to occur and strongly impacted the location and size of the volume containing the cleanest regions of the detector useful for the determination of the solar neutrino flux.

The dynamic evolution of the fiducial volume is best observed by mapping the concentrations of both ^{210}Po and ^{210}Bi event rates in the detector over time. These event rates were determined by simply integrating the event energy distribution within 0.21 - 0.35 MeV for ^{210}Po and 0.5 - 1.0 MeV for ^{210}Bi. These energy cuts effectively selected ^{210}Po and ^{210}Bi events because they were the dominant contributors to the event rate in the low energy region. The concentrations of ^{210}Po and ^{210}Bi decays as a function of vertical position (referred to as Z) inside a 4-meter radius are shown over time in Fig. 9.1. The cleanest portions of the detector were located near the center between Z values of -2 meters and +1 meters. These regions of high purity shrunk as short periods of LS mixing occured during solar data taking. Also visible are short periods of poor data quality indicated by the vertical streaks lacking events. These periods were caused by occasional problems with the data taking electronics (accounting for roughly 14% of the available live time) and are not used in the data analyis.

A region of especially high ^{210}Po and ^{210}Bi concentrations can be seen rising from the bottom of the detector towards the end of the time covered in Fig. 9.1. It was during that time in which the temperature gradient changed drastically due to a water pump failure resulting in the disappearance of high purity LS. This mixing episode effectively ended the solar neutrino data taking.

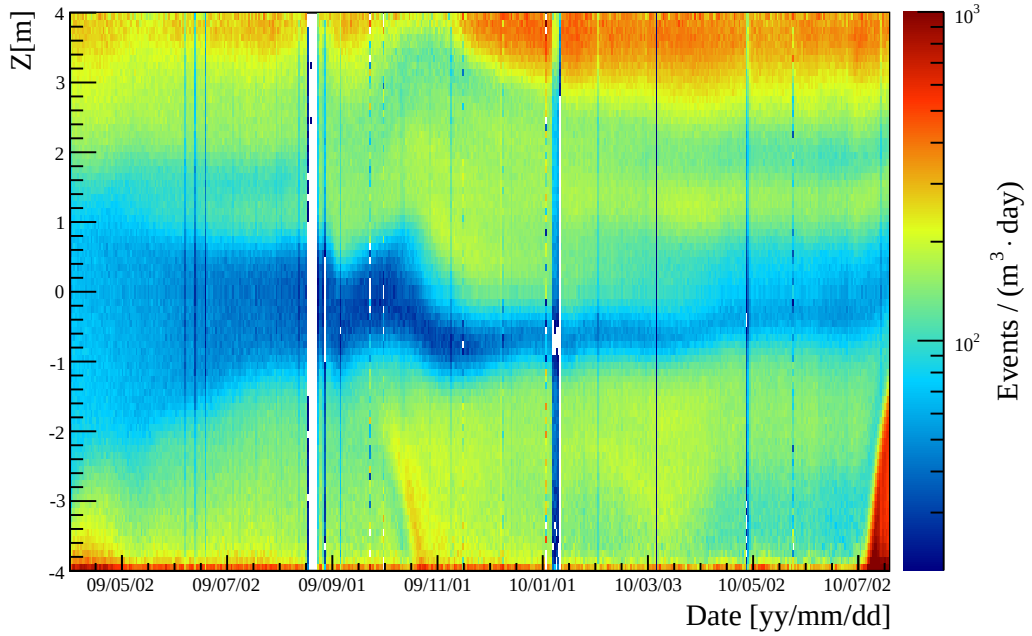

(a)

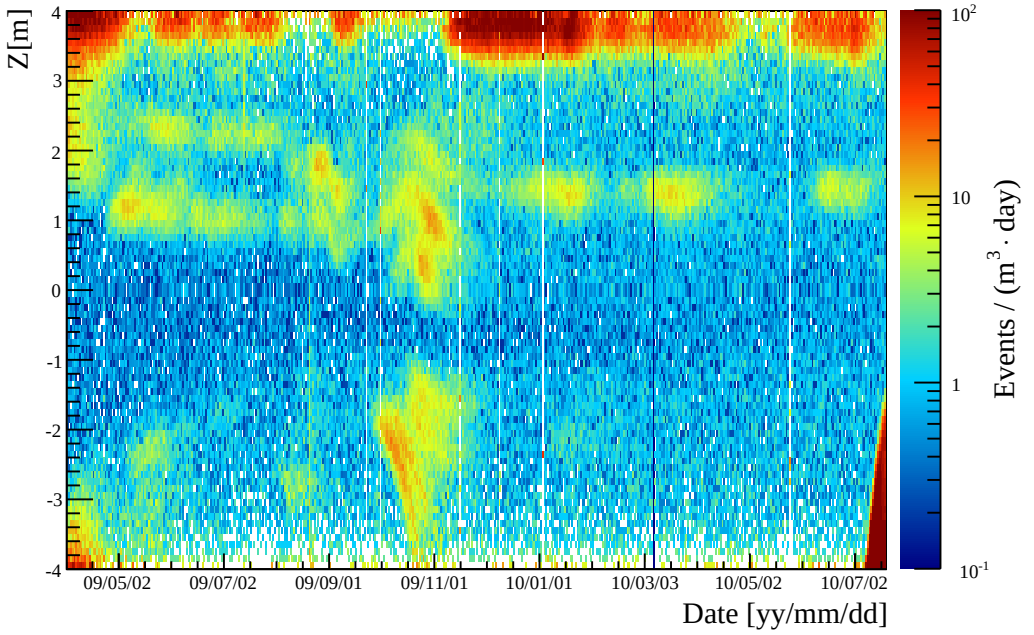

(b)

Figure 9.1: Concentrations of ^{210}Po (a) and ^{210}Bi (b) inside a 4-meter fiducial volume, plotted as a function of Z over time.

The cleanest LS regions were chosen with a more quantitative approach that involved fitting the specific activities of ^{210}Po and ^{210}Bi over time. The procedure for performing the spectral fits was identical to what was done to calculate the backgrounds in Chap. 6. The fits were performed for data that had been divided into 0.5 meter intervals along the vertical axis inside a 4.5 meter radius. The fitted specific activites for ^{210}Po and ^{210}Bi are plotted as a function of time in Figs. 9.2 and 9.3.

The fiducial volume criteria were chosen on a run-by-run basis such that the specific activities for ^{210}Po and ^{210}Bi were less than 3.5 mBq/m^3 and 30 μBq/m^3, respectively. During some data taking periods, volumes were selected using cylindrical cuts in addition to the vertical cuts in order to increase the total exposure. A complete summary of the fiducial volume cuts used in this analysis and the corresponding live time periods are shown in Table 9.1. These selection criteria were applied to two different analyses, one using a spherical volume of radius 4.0 meters and another using a spherical volume of radius of 4.5 meters. The total live time of the data analyzed here is 306.46 days. This is equivalent to a total exposure of 28.12 kton·days for the 4.0 meter radius analysis and 32.91 kton·days for the 4.5 meter radius analysis. The analysis using the 4.5 meter fiducial radius has higher statistics than the analysis using 4.0 meter radius, but also has a larger contribution from external backgrounds appearing at higher energies. These two analyses are compared in Sec. 9.3. Estimates of the systematic uncertainty associated with the fiducial volume selections are discussed in Sec. 9.4.

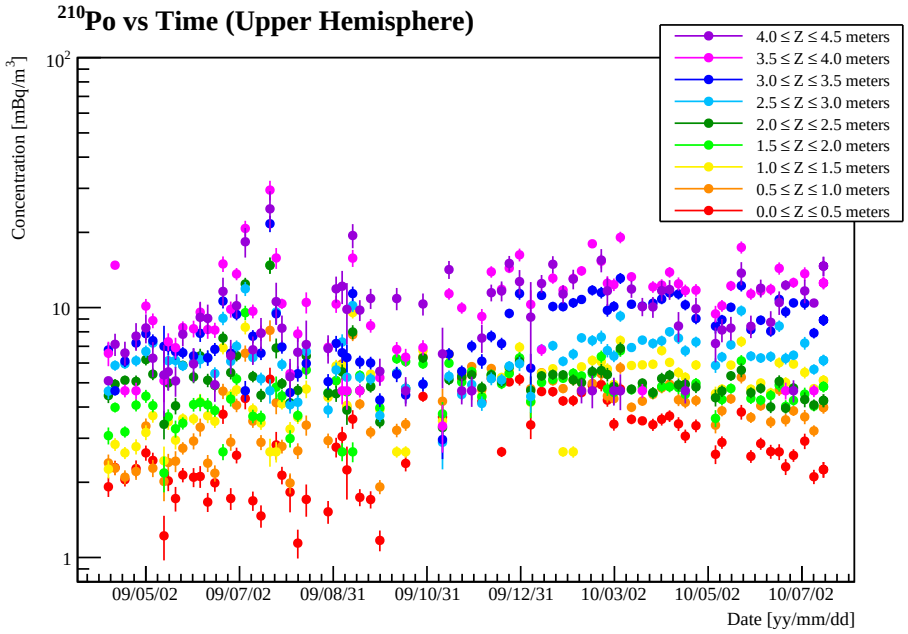

(a)

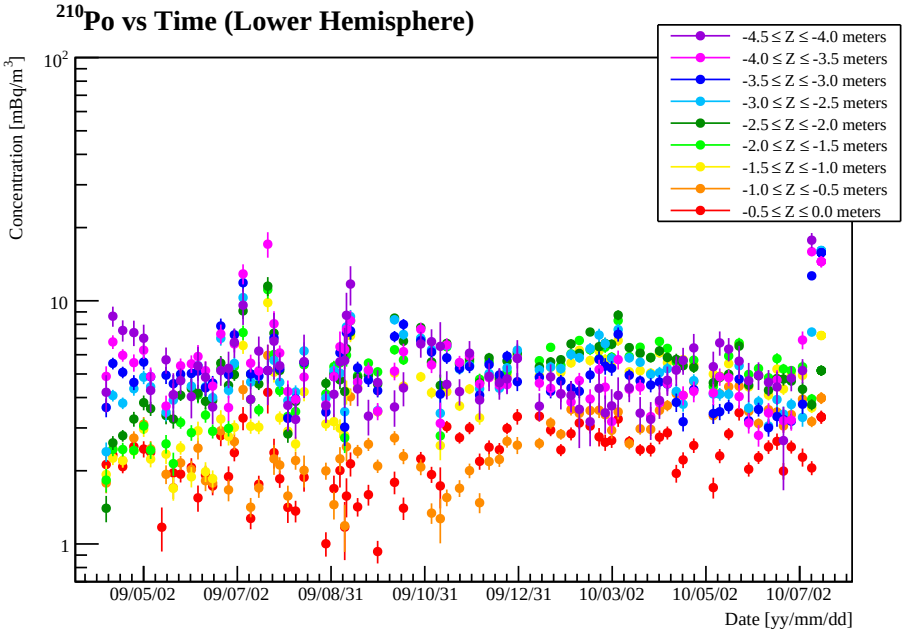

(b)

Figure 9.2: Fits to the ^{210}Po activity per ΔZ over time in the upper region of the detector, shown in (a), and the lower region of the detector, shown in (b).

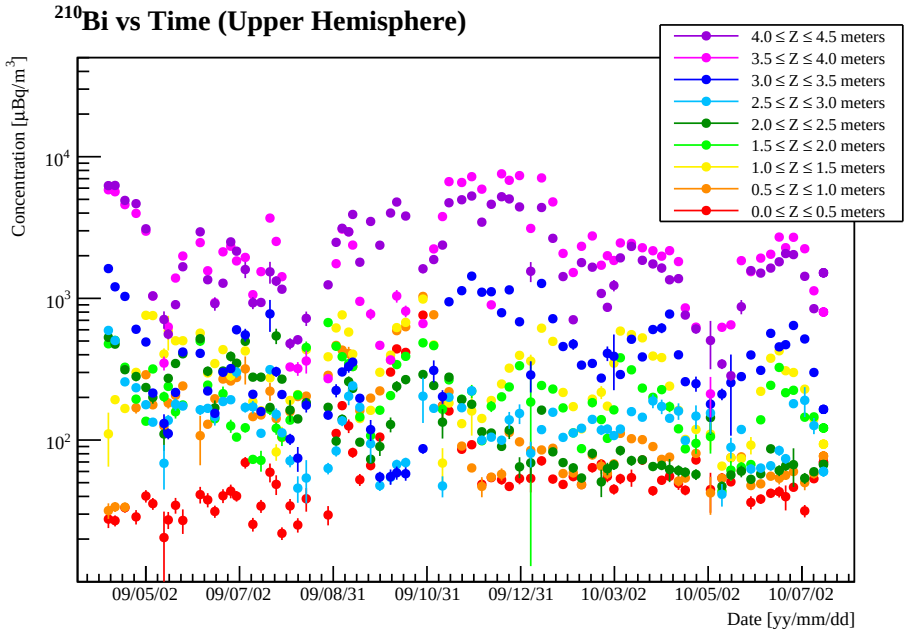

(a)

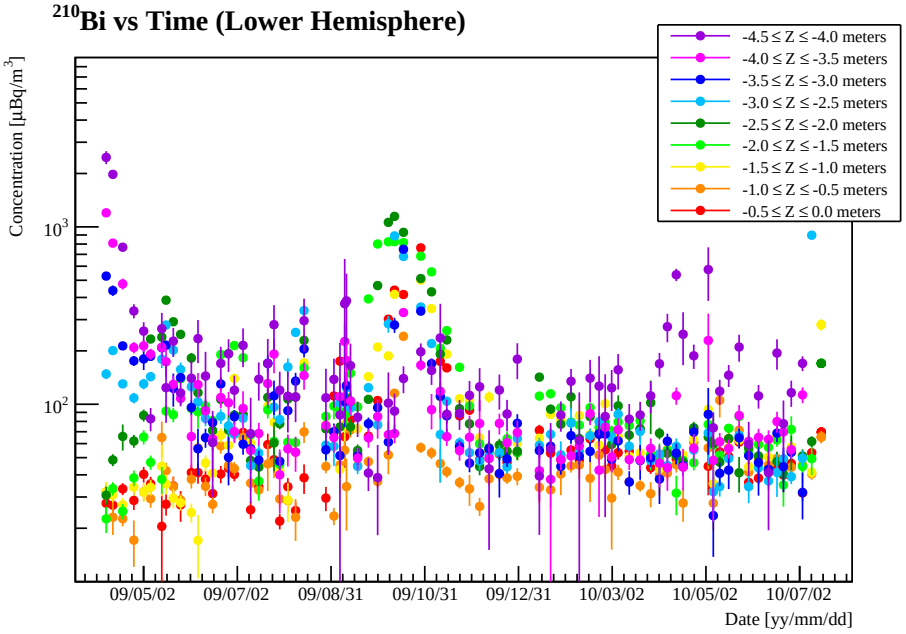

(b)

Figure 9.3: Fits to the ^{210}Bi activity per ΔZ over time in the upper region of the detector, shown in (a), and the lower region of the detector, shown in (b).

Date Range	Live Time [days]	Volume Selection
4/4/2009 - 4/18/2009	9.647	-2.0 m < Z < +1.0 m
4/18/2009 - 6/1/2009	33.721	-1.5 m < Z < +0.5 m
6/1/2009 - 8/3/2009	42.941	-1.5 m < Z < +0.4 m
		(-3.5 m < Z < -1.5 m) & ρ^2 < 7.0 m^2
8/3/2009 - 8/17/2009	8.097	-1.5 m < Z < +0.4 m
9/1/2009 - 10/2/2009	23.554	-1.0 m < Z < 0.0 m
		(-3.5 m < Z < -1.0 m) & ρ^2 < 7.0 m^2
12/5/2009 - 12/21/2009	10.284	-1.0 m < Z < 0.0 m
		(-3.0 m < Z < -1.0 m) & ρ^2 < 6.0 m^2
12/21/2009 - 4/12/2010	96.370	-1.0 m < Z < +0.5 m
		(-3.5 m < Z < -1.0 m) & ρ^2 < 7.0 m^2
4/12/2010 - 7/8/2010	81.115	-1.0 m < Z < +0.5 m
		(-3.5 m < Z < -1.0 m) & ρ^2 < 10.0 m^2

Table 9.1: Fiducial volume cuts for ^{7}Be solar neutrino analysis. The vertical axis position is referred to as Z, while the cylindrical radius is denoted as ρ. These cuts were made for two separate analyses using additional spherical radial constraints of 4.0 meters and 4.5 meters, respectively.

9.2 Event Selection

Additional event selection criteria are imposed to remove any events or time intervals which exhibit characteristics corresponding to various forms of noise or disturbances from cosmic rays. A list of criteria for removal are given below:

- Large amounts of charge of more than 2,500 p.e. collected only by a small subset of PMTs in a localized region of the detector (termed Flasher Events)
- Events satisfying the muon selection criteria discussed in Chap. 5.5.1 and any events occuring within 2 ms of a muon
- Events with missing waveforms due to intervals of high event rate (called Missing

Waveform Events)

- Noise which occurs in a time window of 32 - 35 μs after a 1pps trigger

The removal of events, 2 ms after muons, and noise from the 1pps trigger remove roughly 0.2% effect of the live time of the data and are included into the live time calculation. The uncertainty of the live time calculation was estimated for a similar analysis to be 0.003% in Ref. [61]. The inefficiency of the removal of Flasher Events and Missing Waveform Events are estimated to be less than 0.001% and 0.01%, respectively. These quantities are calculated from calibration source data by taking the ratio of the number of events removed from the data using these cuts and the total number of events, as described in Ref. [61].

The remaining events are evaluated for their energy and vertex reconstruction quality. The vertex and energy fitting algorithms return reduced chi-square values for time and charge information, referred to as χ^2_T and χ^2_Q. These values indicate the goodness of fit. Values of $\sim$1 are indications that the energy and vertex fitters were able to accurately reconstruct a physics event in the detector. The χ^2_T and χ^2_Q values grow exponentially at low energies, so an energy dependent quality cut was constructed based on these parameters. Events are removed from the solar data set if they satisfy the following:

$$\chi^2_Q + \chi^2_T > 150.0 \cdot e^{-16.0[\mathrm{MeV}^{-1}]\cdot E_{vis}[\mathrm{MeV}]} + 1.7 \cdot e^{-0.8[\mathrm{MeV}^{-1}]\cdot E_{vis}[\mathrm{MeV}]} + 4.3 \qquad (9.1)$$

This quality cut as applied to calibration data obtained from sources deployed between Z = -4.5 and 4.5 meters along the vertical axis can be seen in Fig. 9.4. The inefficiency of this quality cut is estimated from the calibration source data using the ratio of the number of events removed with the cut and the total number of events, and is calculated to be 0.003%.

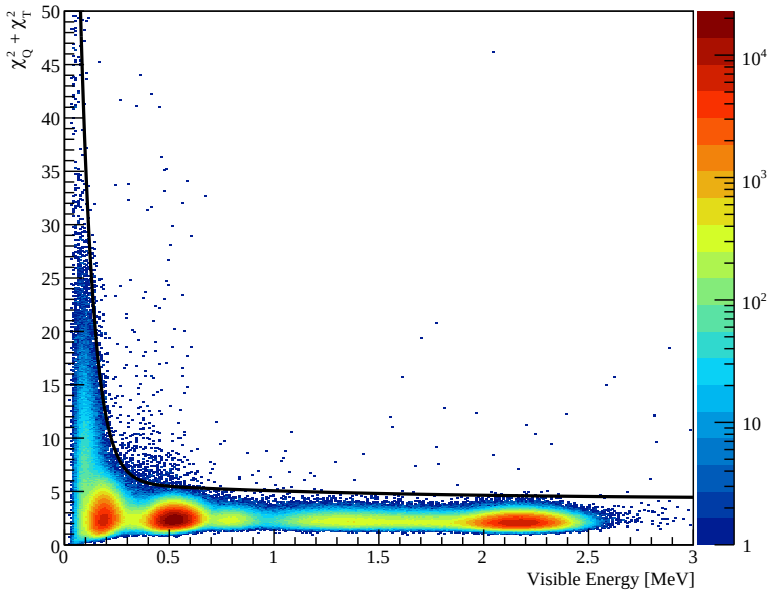

Figure 9.4: Energy dependence of the $\chi^2_Q + \chi^2_T$ cut applied to calibration data taken for radioactive source positions of Z = -4.5 to +4.5 meters along the vertical axis. Events falling above the black line, calculated from Eqn. 9.1, are removed from the data set resulting in an event reconstruction inefficiency of 0.003%.

9.3 Spectral Analysis

The presence of a quantifiable ^{7}Be solar neutrino signal is tested by means of spectral analysis using two different data sets corresponding to fiducial radii of 4.0 meters and 4.5 meters, respectively. The procedure for fitting the spectra calculated using KLG4sim to the KamLAND data is almost identical to what was described in Chap. 6. The amplitude for each spectrum is allowed to float freely, the energy scale is fixed during the minimization of the fit. The Pearson's chi-square without the energy scale shift parameter is:

$$\chi^2 = \sum_j^N \frac{[B(E, a_i) - x_j]^2}{(\Delta x_j)^2} \tag{9.2}$$

where the variables are defined in Chap. 6. The low energy data is fit over an energy interval of 0.24 - 2.0 MeV for events encompassed by a 4.0 meter radius and within

an energy interval of 0.24 - 1.4 MeV for events inside a 4.5 meter radius. ^{14}C is not included in any of the fits due to the lack of simulated events near the endpoint at 0.24 MeV. The ^{14}C spectrum falls off dramtically, thus, having no impact on the fit. To demonstrate this point the ^{14}C spectrum is overlaid onto the fit spectra with an approximately correct but fixed amplitude.

The spectral fits for events within the 4.0 meter radius are shown in Fig. 9.5 and the fits for events inside the 4.5 meter radius are shown in Fig. 9.6. The data are shown by the black points with statistical error bars, while the sum of all the fit spectra is indicated by the red line. It is clear that the backgrounds are quite a bit higher than the ^{7}Be solar neutrino signal, shown in orange, making its unique signature difficult to visually identify in the data. The signal-to-background ratios in the 0.24 to 0.80 MeV region are 0.0006 for the 4.0 meter radius analysis and 0.0008 for the 4.5 meter radius analysis. The background subtracted data with the ^{7}Be signal overlaid and the χ^2 contribution of the fit as a function of energy are also included in Fig. 9.5 and Fig. 9.6. The background subtracted plots provide better visualization of the presence of a quantifiable solar neutrino signal in the data. The large χ^2 contributions at lower energies are attributed to the increasing energy bias between the data and MC, and can only be improved by a better understanding of the ^{210}Po spectral shape.

Given the poor signal-to-background ratios and the large χ^2 values at lower energies, the lower bounds of the fit regions were moved to higher energies where the signal-to-background ratio is more advantageous. In order to define an optimized energy fit region, spectral fits were performed while increasing the lower bound on the fit in 0.01 MeV increments. During this procedure, the ^{210}Po spectrum was constrained by adding a penalty term, χ^2_p, to the Pearson's chi-square:

$$\chi^2 = \sum_{j}^{N} \frac{[B(E, a_i) - x_j]^2}{(\Delta x_j)^2} + \chi^2_p. \tag{9.3}$$

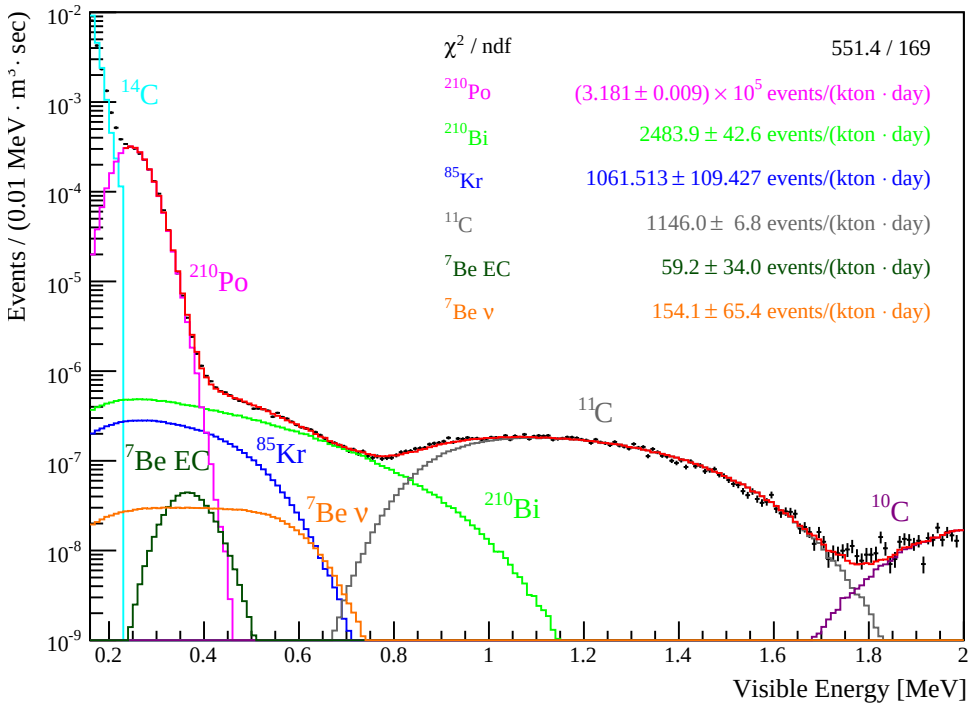

(a)

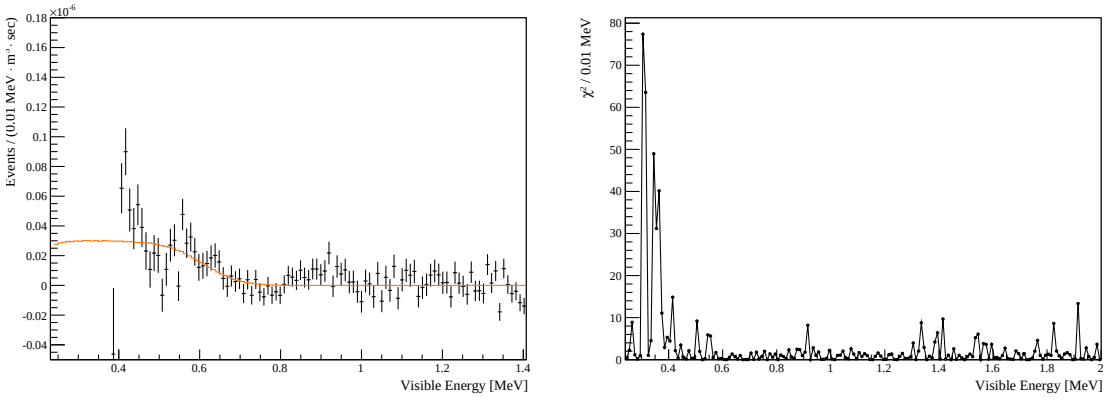

(b) (c)

Figure 9.5: Low energy fits for events inside a 4.0 meter fiducial radius are shown in (a). The resulting ^{7}Be solar neutrino signal is overlaid on the data with the fit backgrounds subtracted in (b) and the χ^2 contributions from the fit as a function of energy is shown in (c).

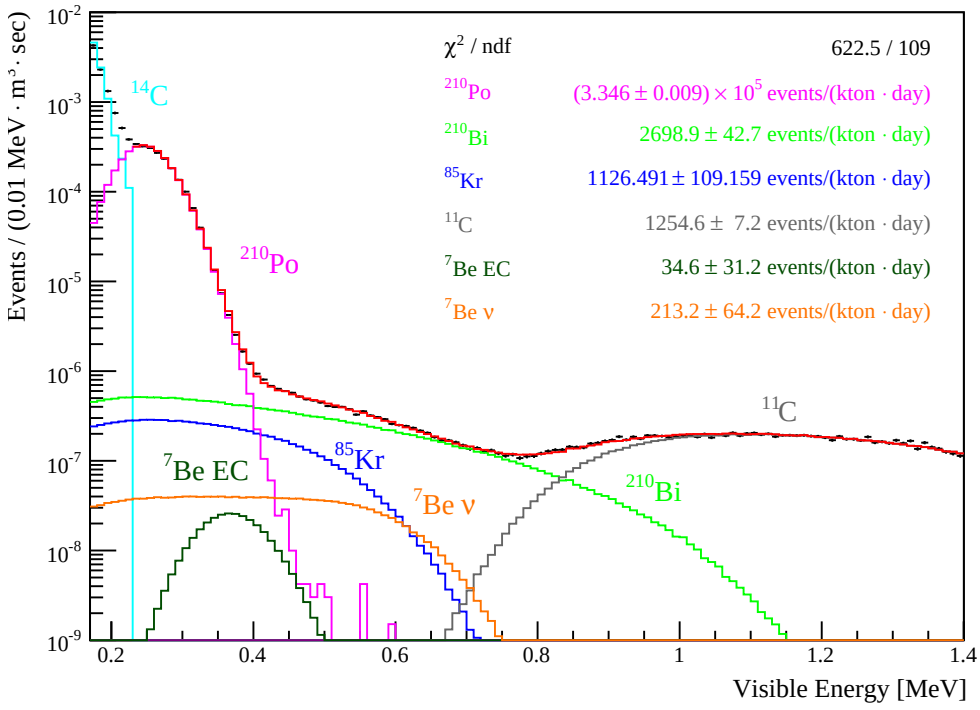

(a)

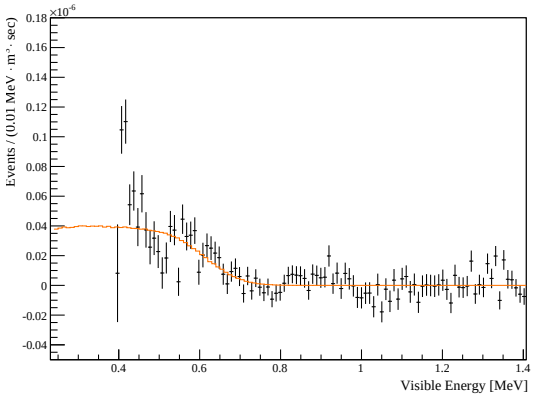

(b)

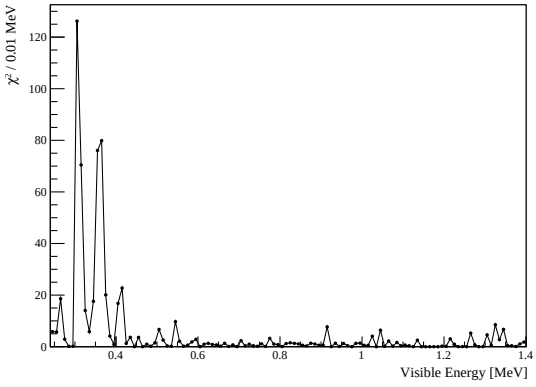

(c)

Figure 9.6: Low energy fits for events inside a 4.5 meter fiducial radius are shown in (a). The resulting ^{7}Be solar neutrino signal is overlaid on the data with the fit backgrounds subtracted in (b) and the χ^2 contributions from the fit as a function of energy is shown in (c).

The penalty term forces the minization algorithm to constrain the ^{210}Po background to the previously measured value while taking into account deviations from the measured value in the calculation of the χ^2. The penalty term for ^{210}Po is:

$$\chi^2_p = \frac{[B_{\mathrm{Po}}(E, a_i) - X_{meas}]^2}{(\Delta X_{meas})^2} \tag{9.4}$$

where $B_{\mathrm{Po}}(E, a_i)$ is the background spectrum due to ^{210}Po, X_{meas} is the measured ^{210}Po event rate in the full fit region, and ΔX_{meas} is the 1σ error on the measured ^{210}Po event rate.

The fit value of ^{7}Be solar neutrino events rate as a function of the lower energy bound of the fit region is shown for both fiducial volumes in Fig. 9.7. The trend is identical in both plots, where a step can be seen near 0.4 MeV. Increasing the lower bound of the fit only increased the statistical uncertainty of the fit signal but leaves the central value approximately constant. As a result, a cutoff of 0.4 MeV was chosen as the best lower bound. The spectral analyses utilizing this lower bound provide the best signal-to-background ratios while minimizing statistical uncertainty.

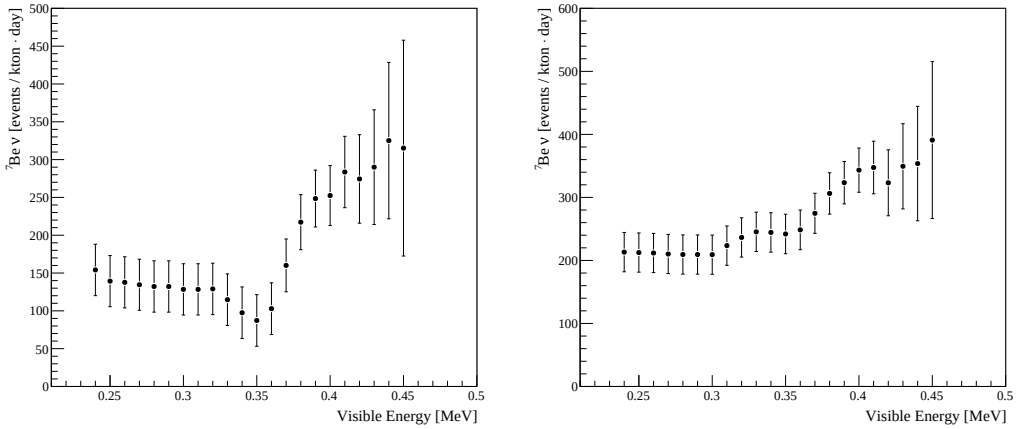

(a) (b)

Figure 9.7: Fit values for the ^{7}Be solar neutrino rate as a function of lower fit bound for the 4.0 meter radius analysis in (a) and the 4.5 meter radius analysis in (b).

The results of fits performed inside the energy regions with a lower bound of 0.4 MeV for the 4.0 meter fiducial radius and the 4.5 meter fiducial radius are shown in Fig. 9.8 and Fig. 9.9, respectively. Fits performed under the null hypothesis (^{7}Be solar neutrino rate assumed to be zero) are also shown in these figures as a comparison. The difference in the χ^2 values between the null hypothesis and the ^{7}Be solar neutrino hypothesis is 15.4 for the 4.0 meter fiducial radius analysis and 27.9 for the 4.5 meter fiducial radius analysis. The improvement of the χ^2 provides strong statistical evidence for the presence of a ^{7}Be solar neutrino signal in the data.

The solar neutrino recoil spectrum, obtained after background subtraction is shown in Fig. 9.9(c). Although this analysis had to cope with substantial backgrounds it is evident from Fig. 9.9(c) that the excess events have a spectral shape characteric of neutrino recoil. Furthermore, the energy of the resulting recoil edge is at a value expected from the known decay energy of ^{7}Be. This observation leads to the conclusion that solar neutrino recoil has indeed been measured and a solar neutrino flux can be determined from the low energy KamLAND data.

A summary of the results for the four different analyses presented in this chapter are shown in Table 9.2. Of these, a 4.5 meter fiducial radius with fitting performed inside the 0.4 - 1.4 MeV energy region provides the largest signal-to-background ratio and has the largest exposure. Hence, this analysis was chosen as the "cornerstone" of this work. Improved sensitivity to ^{7}Be solar neutrinos is not to be expected because of the rather poor signal-to-background ratio. This point is supported by the existence of correlations of the ^{7}Be solar neutrino signal with the ^{85}Kr and ^{210}Bi backgrounds, as shown in Fig. 9.10. Overall, the reduction factors for ^{210}Bi and ^{85}Kr after the purification campaign were 1.5×10^3 and 6.5×10^4, respectively.

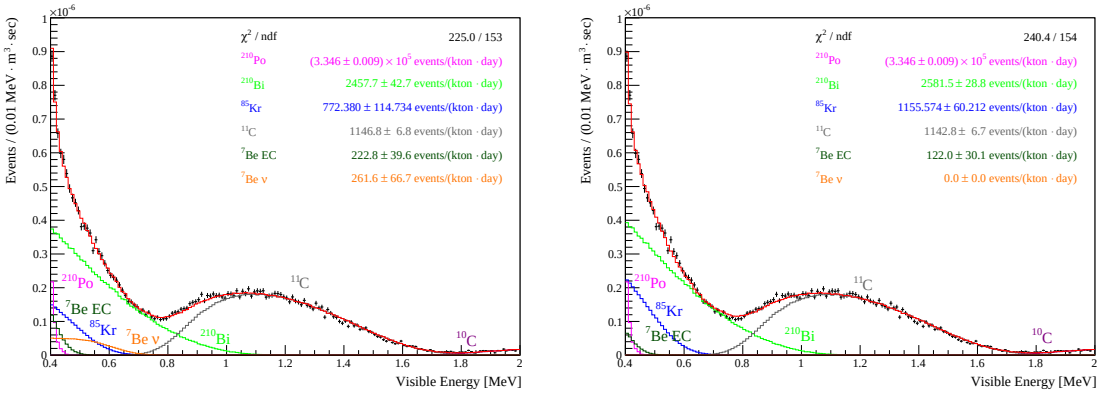

(a) (b)

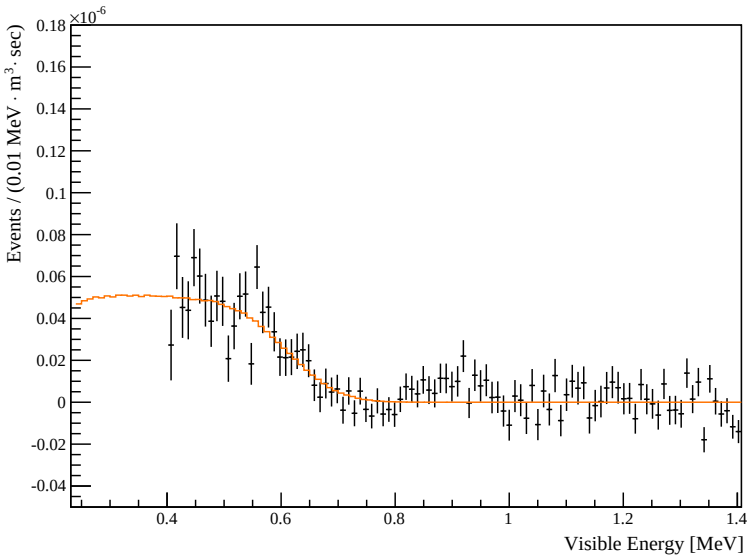

(c)

Figure 9.8: Low energy fits for events inside a 4.0 meter fiducial radius are shown in (a). A fit with the assumption of no ^{7}Be solar neutrino signal is shown as a comparison in (b). The resulting ^{7}Be solar neutrino signal is overlaid on the data with the fit backgrounds subtracted in (c).

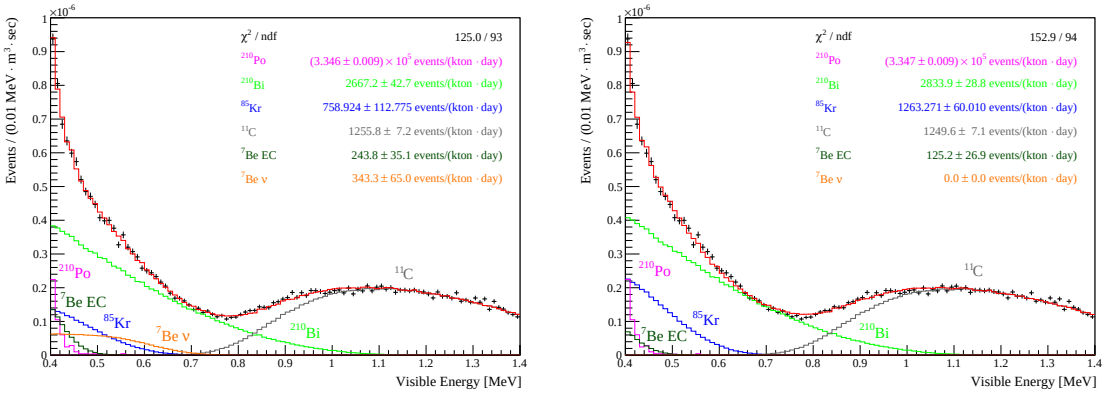

(a) (b)

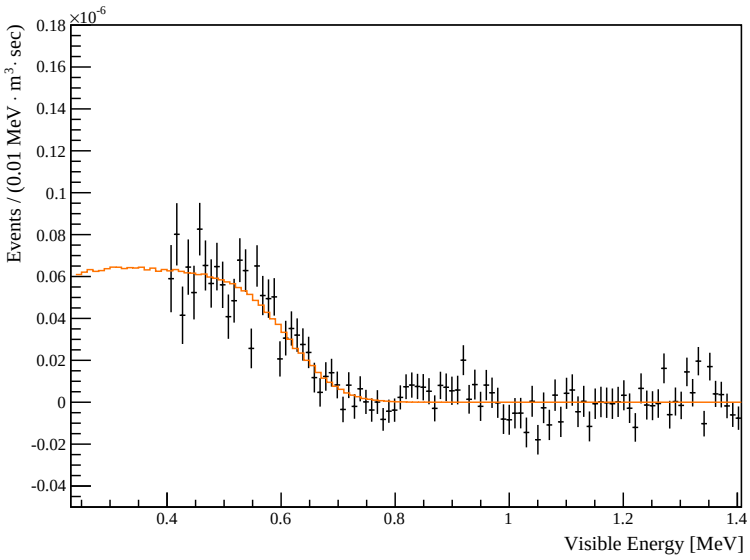

(c)

Figure 9.9: Low energy fits for events inside a 4.5 meter fiducial radius are shown in (a). A fit with the assumption of no ^{7}Be solar neutrino signal is shown as a comparison in (b). The resulting ^{7}Be solar neutrino signal is overlaid on the data with the fit backgrounds subtracted in (c).

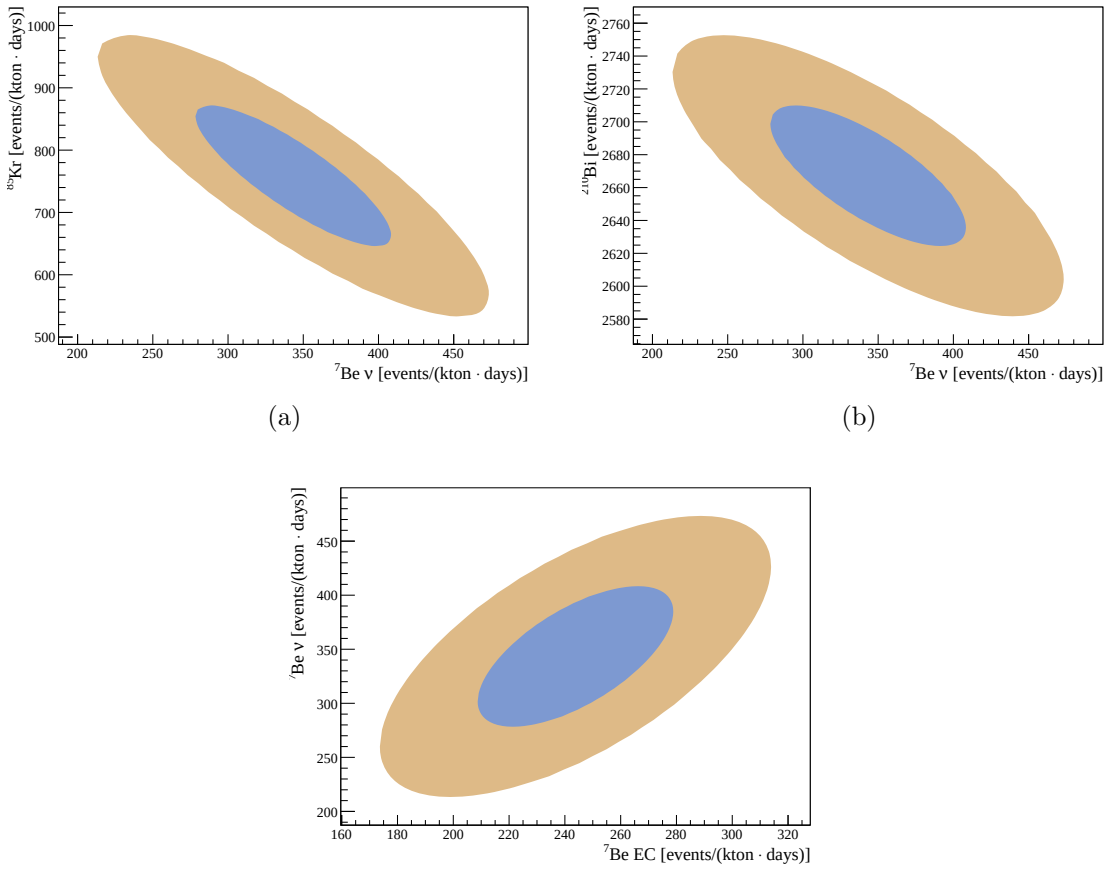

Figure 9.10: Contours of the most significant parameter correlations as obtained from spectral fitting.

Data Set	^{7}Be ν Rate [events/(kton·day)]	S/B
R $<$ 4.0 meters, 0.24 - 2.0 MeV	154.1 $\pm$ 65.4	0.0006
R $<$ 4.0 meters, 0.40 - 2.0 MeV	261.6 $\pm$ 66.7	0.0919
R $<$ 4.5 meters, 0.24 - 1.4 MeV	213.2 $\pm$ 64.2	0.0008
R $<$ 4.5 meters, 0.40 - 1.4 MeV*	343.3 $\pm$ 65.0	0.1131

* This analysis was chosen as the cornerstone result.

Table 9.2: Summary of the ^{7}Be solar neutrino rate results of the four spectral fits described in the text. The last column reports the signal-to-background ratios calculated from the lower bound of the fit regions up to 0.8 MeV.

9.4 Systematic Uncertainties

The systematic uncertainty of the measured ^{7}Be solar neutrino rate is dominated by the uncertainty of the visible energy, but also has contributions from the uncertaintis of the fiducial volume cuts, the number of electron targets, and the calculation of the neutrino-electron scattering cross-section. The latter uncertainties are calculated in detail and summarized in Sec. 9.4.4.

9.4.1 Energy Scale Uncertainty

The differences between the average visible energy determined using KLG4sim for various calibration source runs and KamLAND data was parameterized by an exponential function with constant offset:

$$f(E) = p_0 \cdot e^{E/p_1} + p_2 \tag{9.5}$$

where the result of the fit is shown in Fig. 8.13. This fit to the energy bias of the calibration data has uncertainty, expressed in the form of errors of the fit parameters and the covariance matrix. The fit uncertainty is taken to be the overall uncertainty of the energy scale of the ^{7}Be solar neutrino analysis.

In order to calculate the impact the energy scale uncertainty has on the fitted solar neutrino event rate, the error region of the fit was sampled by randomly generating the fit parameters (p_0, p_1 and p_2) while taking account their errors and correlations. For each modified energy scale the solar fit was then repeated. This random generation was based on a three-dimensional Gauss function taking on the following form [82]:

$$G(p_0, p_1, p_2) = \frac{1}{(2\pi)^{3/2}|\mathbf{\Sigma}|^{1/2}} \cdot \exp\left(-\frac{1}{2}(\mathbf{p}-\boldsymbol{\mu})^T\mathbf{\Sigma}^{-1}(\mathbf{p}-\boldsymbol{\mu})\right) \tag{9.6}$$

where $\mathbf{p} = (p_0, p_1, p_2)$ is the parameter vector, $\boldsymbol{\mu} = (\mu_{p_0}, \mu_{p_1}, \mu_{p_2})$ is the vector containing the best-fit values, and $\boldsymbol{\Sigma}$ is the covariance matrix of the fit parameters. The covariance matrix can be written as a function of the standard deviations and correlations:

$$\boldsymbol{\Sigma} = \begin{pmatrix} \sigma_{p_0}^2 & \rho_{p_0p_1}\sigma_{p_0}\sigma_{p_1} & \rho_{p_0p_2}\sigma_{p_0}\sigma_{p_2} \\ \rho_{p_0p_1}\sigma_{p_0}\sigma_{p_1} & \sigma_{p_1}^2 & \rho_{p_1p_2}\sigma_{p_1}\sigma_{p_2} \\ \rho_{p_0p_2}\sigma_{p_0}\sigma_{p_2} & \rho_{p_1p_2}\sigma_{p_1}\sigma_{p_2} & \sigma_{p_2}^2 \end{pmatrix} \tag{9.7}$$

The inputs to the three-dimensional Gauss function were obtained from the output of the fitting results by MINUIT:

$$\begin{aligned} &\mu_{p_0} = 16.63\%, \quad \mu_{p_1} = -0.19 \text{ MeV}, \quad \mu_{p_2} = -0.67\% \\ &\sigma_{p_0} = 6.29\%, \qquad \sigma_{p_1} = 0.08 \text{ MeV}, \qquad \sigma_{p_2} = 0.83\% \\ &\rho_{p_0p_1} = 0.946, \qquad \rho_{p_0p_2} = 0.532, \qquad \rho_{p_1p_2} = 0.745 \end{aligned} \tag{9.8}$$

The results from the random generation of parameter values within the error region is shown in Fig. 9.11. The blue lines are the randomly generated functions using Eq. 9.5 and the red line is the best-fit from Fig. 8.13. Plots of the correlations between the generated parameters are also shown.

Each of the randomly generated functions in Fig. 9.11(a) are used to calculate an energy-dependent perturbation scale factor:

$$\delta^i(E) = 1 - [f_{Best}(E) - f^i_{Rndm}(E)]/100 \tag{9.9}$$

where f^i_{Rndm} is the i^{th} randomly generated function and f_{Best} is the best-fit function. In order to estimate the impact of the energy scale uncertainty on the ^{7}Be solar neutrino rate, the energy spectra generated in KLG4sim are multiplied with $\delta^i(E)$ and

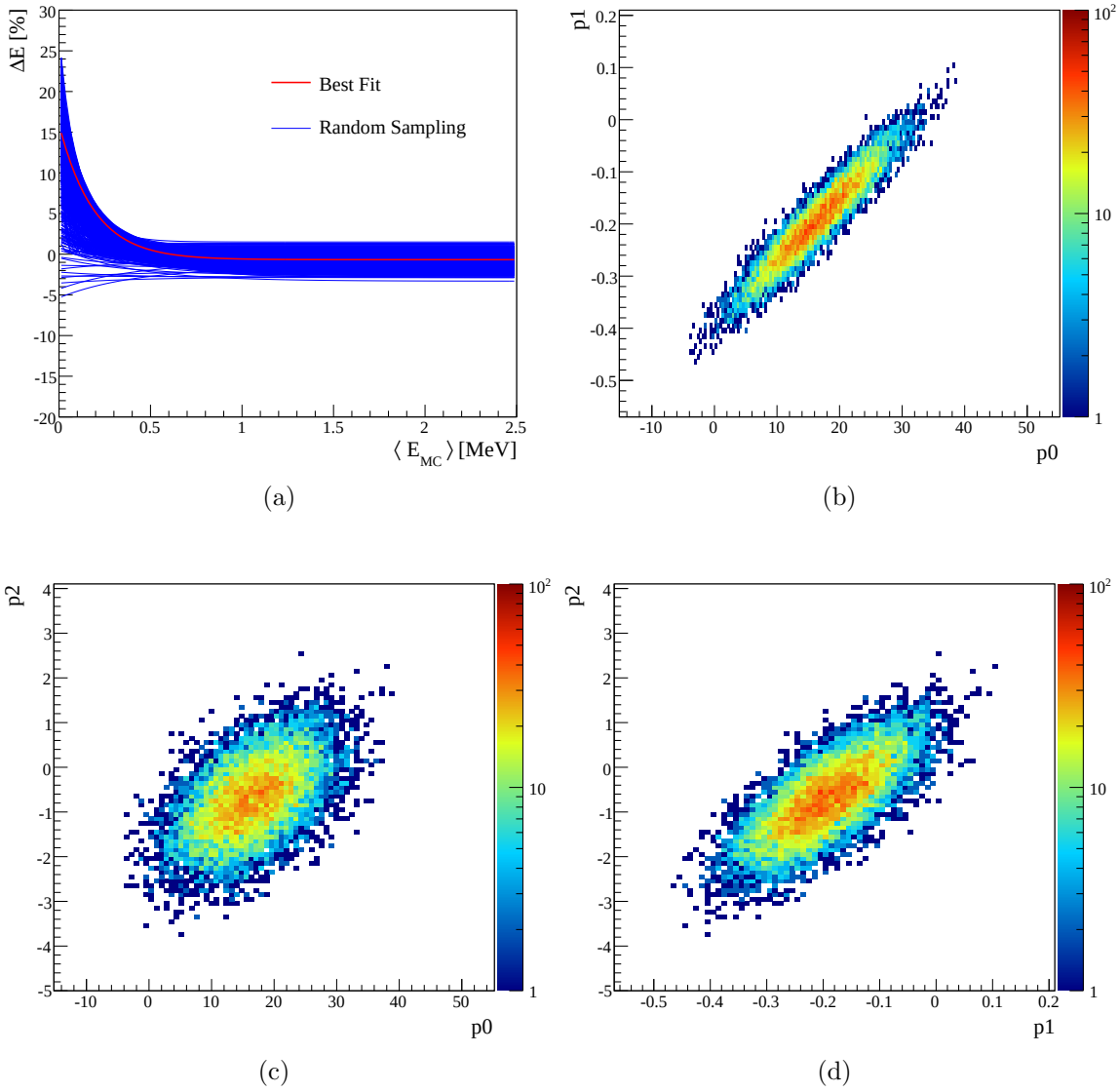

Figure 9.11: Results from the random sampling of the energy uncertainty are shown in (a) and the correlations of the generated parameters are shown in (b), (c) and (d).

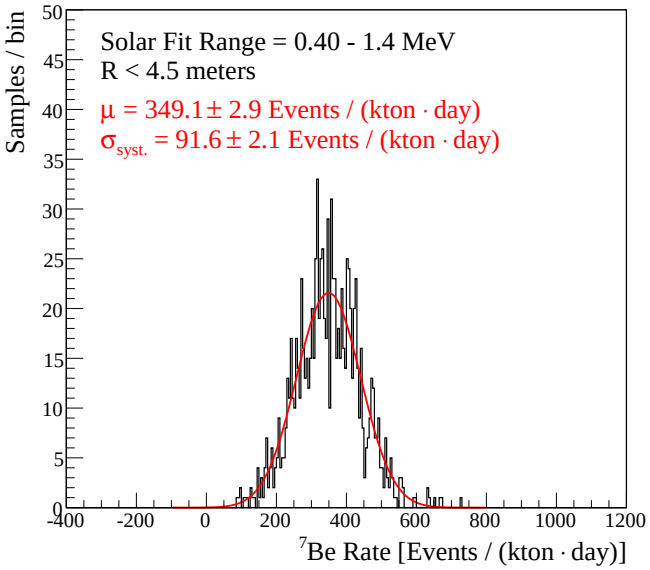

Figure 9.12: ^{7}Be solar neutrino rate results from repeated fitting of perturbed KLG4sim energy spectra. The systematic uncertainty on the rate is calculated to be 91.6 events/(kton·day) for the 4.5 meter fiducial radius analysis inside the 0.4 - 1.4 MeV fit region.

the spectral fits are performed again. This process of convoluting the spectra with randomly generated scale factors and re-fitting is performed 1000 times. The effect of these perturbations on the ^{7}Be solar neutrino rate is shown for the 4.5-meter fiducial radius analysis in Fig. 9.12. The systematic uncertainty on the measured rate due to the energy scale uncertainty is defined as the standard deviation of the distribution of rates obtained after repeated fits and is equal to 91.6 events/(kton·day). Given the measured rate of R = 343.3 events/(kton·day) this is equivalent to a 26.7% uncertainty. The large effect of the energy scale uncertainty on the measured rate is due to the small signal-to-background ratio. It should be noted that the ^{210}Po energy spectrum in KLG4sim was varied independently of the other spectra during the re-fitting process using randomly generated variations based on the energy bias of -0.9 ± 0.3% calculated in Chap. 8.3.4.

9.4.2 Fiducial Volume Uncertainty

The fiducial volume uncertainty can be calculated using some properly chosen uniform event distribution inside the detector. Ideally this test distribution should be free of background and should have comparable energy as the solar neutrino signal to properly explore this uncertainty. As such distribution does not exist neutrons produced through cosmic-ray muon-spallation were chosen. Spallation neutrons in KamLAND capture with 99.5% probability on ^{1}H. The mean capture time is 207.5 $\pm$ 2.8 μs [68]. Neutron captures on ^{1}H result in the emission of 2.225 MeV gammas (corresponding to roughly 2.1 MeV visible energy). These events were selected using an energy cut of $1.9 < E < 2.3$ MeV after identifying a muon in the detector using the criteria in Chap. 5.5.1. The distribution of neutron capture time differences relative to their parent muons is shown in Fig. 9.13(a), where the fit function is of the following form:

$$f(t) = N_0 \cdot e^{-t/\tau} + B. \tag{9.10}$$

where N_0 is the number of neutron captures at time of muon impact, τ is the mean capture time and B is the background. The neutron capture events can be seen within the first 1000 μs. In order to acquire a clean data set, an additional time cut of $400 < t < 1000$ μs relative to parent muons was applied to select these events. The random background due to neutrons entering from the outside and clustering near the balloon was subtracted statistically by using events identified with the help of an off-time window of $2400 < t < 3000$ μs. The distribution of event density is shown in Fig. 9.13(b) after background subtraction.

The spallation neutron events were used to calculate the ratio of the number neutron events inside a given fiducial volume, N_{fid}, relative to the number of neutron events inside the entire detector, N_{full}:

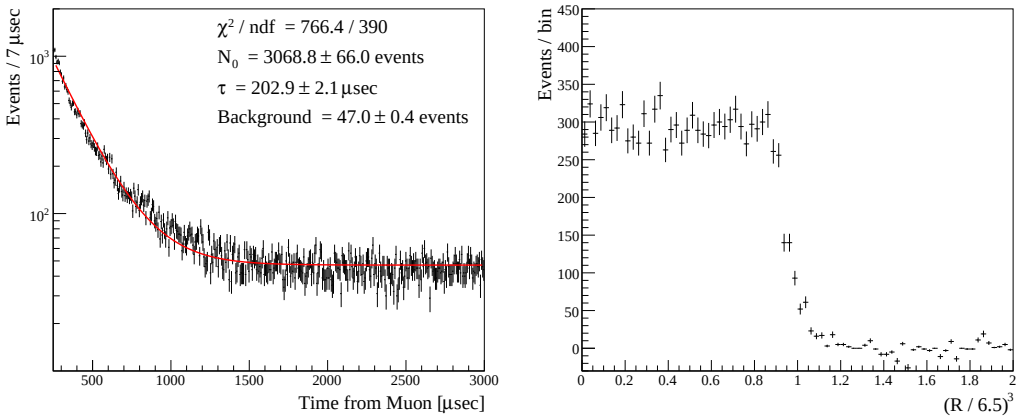

(a) (b)

Figure 9.13: Neutron capture time differences from muons are shown in (a) and the background-subtracted distribution of spallation neutrons as a function of R^3 is shown in (b).

$$R_{event} = \frac{\sum_i N_{fid,i}}{\sum_i N_{full,i}} \tag{9.11}$$

where the sum is performed over each of the volumes utilized in the solar neutrino analysis and listed in Table 9.1. This ratio can be multiplied by the total volume of LS (V_{full}) measured with flow meters during KamLAND's initial filling to obtain an estimate of the fiducial volume:

$$V_{fid} = R_{event} \cdot V_{full}. \tag{9.12}$$

In this calculation, $R_{event} = 0.1316 \pm 0.0143$ and the measured LS volume was $V_{full} = 1171.12 \pm 25.00$ m^3 [83] resulting in $V_{fid} = 154.12 \pm 17.12$ m^3. A purely geometrical calculation of the average fiducial volume from the cuts in Table 9.1 gives a value of 140.42 m^3, which is consistent within 1σ to the value obtained by the event ratio approach. The systematic uncertainty in the fiducial volume was obtained from propagation of the errors on the event ratio and the LS volume, and was calculated to be 11.1%.

9.4.3 Cross Section and Target Number Uncertainty

The uncertainty of the neutrino-electron scattering cross section was estimated by comparing electron recoil spectra from ^{7}Be neutrinos with, and without, the effects of radiative corrections in Ref. [39]. The net change over the entire recoil energy range was $\lesssim 1\%$. This difference is taken to be a measure of the systematic uncertainty.

The largest contributions to the uncertainty in the number of electron targets in the LS comes from the uncertainty of the LS density. The uncertainty in the LS density is driven by the temperature gradient from the top to the bottom of the detector and the fact that the LS chemical formulation was modified during the purification campaign. The temperature gradient was determined in Ref. [84] where the volume weighted average of the density change due to the temperature changes along the central axis was calculated to be 0.1%. The uncertainty of the LS density introduced by its purification was estimated from periodic measurements of the density over time. This uncertainty was found to be 0.025% [61]. From these two results, the total uncertainty for the number of target electrons is estimated to be about 0.0103%.

9.4.4 Summary of Uncertainties

The various contributions to the systematic uncertainty of a ^{7}Be solar neutrino measurement are summarized in Table 9.3. The largest contribution comes from the energy scale uncertainty, the second largest from the fiducial volume uncertainty. Compared to these two all other sources of systematic uncertainty are negligible. The total systematic uncertainty taken to be the quadratic sum (thus assuming that all errors are independent) of all entries into Table 9.3 is 28.9%. The measured ^{7}Be solar neutrino rate in KamLAND is $R = 343.3 \pm 65.0(\text{stat}) \pm 99.2(\text{syst})$ events/(kton·day).

Source	Uncertainty
Energy Scale	26.7%
Fiducial Volume	11.1%
Cross Section	1.0%
Number of Targets	0.0103%
Missing Waveforms	0.01%
Live Time	0.003%
Flasher Events	0.001%
Total	28.9%

Table 9.3: Summary of the systematic uncertainties of the ^{7}Be solar neutrino measurement.

9.5 Comparison of the Results

There were two previous independent analyses of the ^{7}Be solar neutrino event rate in KamLAND. These analyses utilized analytical background and signal functions folded with estimates of the detector response to model the spectra used for fitting. The first analysis utilized 5.448 kton·days exposure, resulting in a ^{7}Be solar neutrino rate of $R = 663.3 \pm 267.6$(stat) events/(kton·day) [62]. The second analysis, based on 17.8 kton·days exposure, resulted in a ^{7}Be solar neutrino rate of $R = 482 \pm 86$(stat) $\pm$ 73(syst) events/(kton·day) [61]. The ^{7}Be solar neutrino interaction rate measurement reported in this work of $R = 343.3 \pm 65.0$(stat) $\pm$ 99.2(syst) events/(kton·day) had the full event set of 32.91 kton·days available and agrees within 1σ with these previous results.

The corresponding ^{7}Be solar neutrino flux, Φ, can be determined from the measured rate, R, using the following equation:

$$\Phi = \frac{R \times [1 \text{ day}/86400 \text{ seconds}]}{N_e \cdot 0.8948 \cdot \{P(e \rightarrow e) \cdot \sigma_{\nu_e} + [1 - P(e \rightarrow e)] \cdot \sigma_{\nu_{\mu/\tau}}\}} \tag{9.13}$$

where $N_e = 3.4316 \times 10^{32}$ electron targets, $P(e \rightarrow e)$ is the electron neutrino survival

probability defined in Eq. 3.35, $\sigma_{\nu_e} = 5.942 \times 10^{-45}$ cm^2 is the total cross-section for $\nu_e - e$ scattering, $\sigma_{\nu_{\mu/\tau}} = 1.252 \times 10^{-45}$ cm^2 is the total cross-section for $\nu_{\mu/\tau} - e$ scattering, and the factor of 0.8948 is the branching fraction for ^{7}Be neutrino emission of 0.862 MeV. Using the most recent neutrino oscillation parameters reported in Ref. [85] of $\Delta m^2_{21} = 7.50^{+0.19}_{-0.20} \times 10^{-5}$ eV^2 and $\tan^2\theta_{12} = 0.444^{+0.036}_{-0.030}$, the survival probability is $P(e \to e) = 0.546^{+0.010}_{-0.011}$. The calculated ^{7}Be solar neutrino flux from a rate of $R = 343.3 \pm 65.0(\text{stat}) \pm 99.2(\text{syst})$ events/(kton·day) is $\Phi = (3.41 \pm 1.18) \times 10^9$ cm^{-2}s^{-1}. This result comes within 1σ agreement of both the SSM(AGSS09) prediction of $\Phi = (4.64 \pm 0.06) \times 10^9$ cm^{-2}s^{-1} and the measured flux by Borexino of $\Phi = (4.84 \pm 0.24) \times 10^9$ cm^{-2}s^{-1} [21].

Radiochemical experiments, such as Homestake, GALLEX/GNO, and SAGE, have measured integral fluxes of solar neutrinos having contributions from ^{7}Be. However, these experiments do not have the ability to directly measure the individual ^{7}Be solar neutrino flux. The KamLAND sensitivity to ^{7}Be solar neutrinos has been validated by strong statistical evidence, and the reported ^{7}Be solar neutrino flux is only the second real-time measurement in the world. This result provides important validation of the Borexino measurement. Additionally, the agreement of the reported flux with standard solar model predictions confirms our understanding of the fusion reaction processes happening inside the Sun.

Chapter 10

Conclusion

This work describes the efforts to reduce the ^{7}Be solar neutrino backgrounds caused by radioactivity in the liquid scintillator. A total of 5.4 ktons of scintillator was circulated through the purification system over the course of two campaigns from May of 2007 to February of 2009. The reduction factors observed for ^{210}Bi and ^{85}Kr after purification were 1.5×10^{3} and 6.5×10^{4}, respectively.

The tuning of the light model in the KamLAND Monte Carlo simulation (KLG4sim) was performed using radioactive calibration source and ^{210}Po alpha-decay data. The reconstructed energy of simulation was shown to have good agreement with the data for uniformly distributed ^{214}Bi events inside the detector. As a result of the tuning, the reconstructed energy of the simulation is taken to be accurate to within 2% of the data for energies above 0.4 MeV. The internal backgrounds for the ^{7}Be solar neutrino analysis and estimates of the contribution to the background from external radioactivity on the detector components were both simulated using the KLG4sim software.

The results of the first low energy data analysis based on the newly tuned detector simulations were presented. A measurement of the ^{7}Be solar neutrino interaction rate in KamLAND yield $R = 343.3 \pm 65.0(\text{stat}) \pm 99.2(\text{syst})$ events/(kton·day) and is

consistent with two previous KamLAND analyses. The interaction rate obtained here is equivalent to a total neutrino flux of $\Phi = (3.41 \pm 1.18) \times 10^9$ cm^{-2}s^{-1}, a result in 1σ agreement with the Borexino measurement of $\Phi = (4.84 \pm 0.24) \times 10^9$ cm^{-2}s-1 and the standard solar model (AGSS09) prediction of $\Phi = (4.64 \pm 0.06) \times 10^9$ cm^{-2}s^{-1}. The reported ^{7}Be solar neutrino flux is only the second real-time measurement worldwide. This result provides validation of the Borexino measurement, and confirms our understanding of solar fusion reaction processes.

Bibliography

[1] A. H. Becquerel. Sur les radiations émises par phosphorescence. *Comptes Rendus*, 122:420–421, 1896.

[2] J. Chadwick. Intensitätsvertielung im magnetischen Spektren der β-Strahlen von Radium B + C. *Verh. d. D. Phys. Ges.*, 16:383–391, 1914.

[3] J. Chadwick. The Existence of a Neutron. *Proceeddings of the Royal Society, Series A*, 136:692–708, 1932.

[4] Dan Cooper. *Enrico Fermi: and the Revolutions of Modern Physics*. Oxford University Press, New York, NY, 1999.

[5] F.B. Harrison A.D. McGuire F. Reines, C.L. Cowan and H.W. Kruse. Detection of the free anti-neutrino. *Phys. Rev.*, 117(1):159–173.

[6] D. S. Harmer R. Davis Jr. and K. C. Hoffman. Search for neutrinos from the Sun. *Phys. Rev. Lett.*, 20:1205–1209, 1968.

[7] J. N. Bahcall and R. Davis Jr. Solar neutrinos: a scientific puzzle. *Science*, 1:264–267, 1976.

[8] K. S. Hirata et al. Results from one thousand days of real-time, directional solar-neutrino data. *Phys. Rev. Lett.*, 65(11):1297–1300, 1990.

[9] J. Hosaka et al. Solar neutrino measurements in Super-Kamiokande-I. *Phys. Rev. D*, 73(112001), 2006.

[10] M. Altmann et al. Complete results for five years of GNO solar neutrino observations. *Phys. Lett. B*, 616:174–190, 2005.

[11] J. N. Abdurashitov et al. Solar neutrino flux measurements by the Soviet-American Gallium Experiment (SAGE) for half the 22-year solar cycle. *J. Exp. Theor. Phys.*, 95(2):181–193, 2002.

[12] Q. R. Ahmad et al. Direct evidence for neutrino flavor transformation from neutral-current interactions in the Sudbury Neutrino Observatory. *Phys. Rev. Lett.*, 89(1), 2002.

[13] B. Aharmim et al. Electron energy spectra, fluxes, and day-night asymmetries of ^{8}B solar neutrinos from measurements with NaCl dissolved in the heavy-water detector at the Sudbury Neutrino Observatory. *Phys. Rev. C*, 72(055502), 2005.

[14] B. Aharmim et al. Independent Measurement of the Total Active ^{8}B Solar Neutrino Flux Using an Array of ^{3}He Proportional Counters at the Sudbury Neutrino Observatory. *Phys. Rev. Lett.*, 101(111301), 2008.

[15] B. Pontecorvo. Neutrino Experiments and the Problem of Conservation of Leptonic Charge. *Sov. Phys. JETP*, 26:984–988, 1968.

[16] L. Wolfenstein. Neutrino Oscillations in Matter. *Phys. Rev. D*, 17:2369–2374, 1978.

[17] S. P. Rosen and J. M. Gelb. Mikheyev-Smirnov-Wolfenstein Enhancement of Oscillations as a Possible Solution to the Solar-Neutrino Problem. *Phys. Rev. D*, 34:969–979, 1986.

[18] S. Abe et al. Precision measurement of neutrino oscillation parameters with KamLAND. *Phys. Rev. Lett.*, 100:221803, 2008.

[19] A. Gando et al. Partial radiogenic heat model for Earth revealed by geoneutrino measurements. *Nature Geoscience*, 4:647–651, 2011.

[20] T. Araki et al. Experimental investigation of geologically produced antineutrinos with KamLAND. *Nature*, 436:499–503, 2005.

[21] G. Bellini et al. Precision measurement of the ^{7}Be solar neutrino interaction rate in Borexino. *Phys. Rev. Lett.*, 107:141302, 2011.

[22] S. Basu and H. M. Antia. Helioseismology and Solar Abundances. *Phys. Rept.*, 457:217–283, 2008.

[23] J. N. Bahcall. *Neutrino Astrophysics*. Cambridge University Press, New York, NY, 1989.

[24] R.Q. Huang and K.N. Yu. *Stellar Astrophysics*. Springer, Singapore, 1998.

[25] S.D. Kawaler C.J. Hansen and V. Trimble. *Stellar Interiors: Physical Principles, Structure and Evolution*. Springer, New York, NY, 2004.

[26] The Opacity Project. `http://cdsweb.u-strasbg.fr/topbase/TheOP.html`.

[27] A. M. Serenelli J. N. Bahcall and S. Basu. 10,000 Standard Solar Models: a Monte Carlo Simulation. *Astrophys. J. Suppl.*, 165:400–431, 2006.

[28] J. W. Ferguson A. M. Serenelli, S. Basu and M. Asplund. New solar composition: The problem with solar models revisited. *The Astrophysical Journal*, 705:123–127, 2009.

[29] H. A. Bethe. Energy production in stars. *Phys. Rev.*, 55:103, 1939.

[30] H. A. Bethe. Energy production in stars. *Phys. Rev.*, 55:400–431, 1939.

[31] M. Fukugita and T. Yanagida. *Physics of Neutrinos and Applications to Astrophysics*. Springer-Verlag, Berlin, Germany, 2003.

[32] C. Giunti and C. W. Kim. *Fundamentals of Neutrino Physics and Astrophysics*. Oxford University Press, New York, NY, 2007.

[33] N. Grevesse and A.J. Sauval. Standard solar composition. *Space Sci. Rev.*, 85:161–174, 1998.

[34] N. Grevesse M. Asplund and J. Sauval. The solar chemical composition. *Nucl. Phys. A*, 777:1–4.

[35] J. Bahcall. Software and Data for Solar Neutrino Research. `http://www.sns.ias.edu/~jnb/SNdata/sndata.html`.

[36] W. T. Winter et al. The ^{8}B neutrino spectrum. *Phys. Rev. C*, 73:025503, 2006.

[37] J. Bahcall. ^{7}Be solar neutrino line: A reflection of the central temperature distribution of the sun. *Phys. Rev. D*, 49(8):3923–3945, 1994.

[38] C. Quigg. *Gauge Theories of the Strong, Weak, and Electromagnetic Interactions*. Westview Press, Boulder, CO, 1997.

[39] M. Kamionkowski J. Bahcall and Alberto Sirlin. Solar neutrinos: Radiative corrections in neutrino-electron scattering experiments. *Phys. Rev. D*, 51(11):6146–6158, 1995.

[40] P. Vogel and J. Engel. Neutrino electromagnetic form factors. *Phys. Rev. D*, 39(11):3378–3383, 1989.

[41] C. Arpesella et al. Direct measurement of the ^{7}Be solar neutrino flux with 192 days of Borexino data. *Phys. Rev. Lett.*, 101:091302, 2008.

[42] F. Simkovic M. Gozdz, W. Kaminski and A. Faessler. Transition magnetic moments of Majorana neutrinos in supersymmetry without R-parity in light of neutrino oscillations. *Phys. Rev. D*, 74:055007, 2006.

[43] B. Pontecorvo. Mesonium and anti-mesonium. *Sov. Phys. JTEP*, 6(429), 1957.

[44] M. Nakagawa Z. Maki and S. Sakata. Remarks on the Unified Model of Elementary Particles. *Progress of Theoretical Physics*, 28(5):870–880, 1962.

[45] R.D. McKeown and P. Vogel. Neutrino masses and oscillations: Triumphs and challenges. *Phys. Rep.*, 394:315.

[46] Y. Abe et al. Indication for the disappearance of reactor electron antineutrinos in the Double Chooz experiment. *arXiv:hep-ex/1112.6353v1*, 2011.

[47] T. K. Kuo and J. Pantaleone. Neutrino oscillations in matter. *Rev. Mod. Phys.*, 61(4):937–979.

[48] S. P. Mikheev and A. Y. Smirnov. Resonance enhancement of oscillations in matter and solar neutrinio spectroscopy. *Sov. J. Nucl. Phys.*, 42(6):913–917.

[49] S. J. Parke. Nonadiabatic level crossing in resonant neutrino oscillations. *Phys. Rev. Lett.*, 57(10):1275–1278.

[50] S. J. Parke and T. P. Walker. Resonant-solar-neutrino-oscillation experiments. *Phys. Rev. Lett.*, 57(18):2322–2325.

[51] C. Zener. Nonadiabatic level crossing of energy levels. *Proc. Roy. Soc. A*, 137(833):696–702.

[52] D. R. Lide, editor. *CRC Handbook of Chemistry and Physics*. CRC Press, Boca Raton, FL, 87th edition, 2006.

[53] R. M. Stephenson. *Flash Points of Organic and Organometallic Compounds*. Elsevier Science Publishing Co., Inc., New York, NY, 1987.

[54] Hamamatsu Photonics. `http://www.hamamatsu.com/`.

[55] O. Tajima. Development of Liquid Scintillator for a Large Size Neutrino Detector. Master's thesis, Tohoku University - Sendai, JAPAN, 2000.

[56] B. E. Berger et al. The KamLAND Full-Volume Calibration System. *JINST*, 4, 2009.

[57] S. Enomoto. *Neutrino Geophysics and Observation of Geo-neutrinos at KamLAND*. PhD thesis, Tohoku University - Sendai, JAPAN, 2005.

[58] M. Batygov. *Combined Study of Reactor and Terrestrial Antineutrinos with KamLAND*. PhD thesis, The University of Tennessee - Knoxville, TN, 2006.

[59] K. Ichimura. *Presicion Measurement of Neutrino Oscillation Parameters with KamLAND*. PhD thesis, Tohoku University - Sendai, JAPAN, 2008.

[60] I. Shimizu. *An Evidence for Spectral Distortion of Reactor Anti-Neutrinos and A Study of Three Flavor Neutrino Oscillation*. PhD thesis, Tohoku University - Sendai, JAPAN, 2004.

[61] K. Nakajima. *First Results from ^{7}Be Solar Neutrino Observation with KamLAND*. PhD thesis, Tohoku University - Sendai, JAPAN, 2009.

[62] G. Keefer. *First Observation of ^{7}Be Solar Neutrinos with KamLAND*. PhD thesis, University of Alabama - Tuscaloosa, AL, 2009.

[63] E.J. Konopinski. *The Theory of Beta Radioactivity*. Oxford University Press, New York, NY, 1966.

[64] K. Eguchi et al. First results from KamLAND: Evidence for reactor antineutrino disappearance. *Phys. Rev. Lett.*, 90(2):021802, 2003.

[65] MINUIT - Function Minimization and Error Analysis. `http://wwwasdoc.web.cern.ch/wwwasdoc/minuit/minmain.html`.

[66] ROOT: An Object-Oriented Data Analysis Framework. `http://root.cern.ch/root/`.

[67] T. Hagner. Muon-induced production of radioactive isotopes in scintillation detectors. *Astroparticle Physics*, 14:33–47, 2000.

[68] S. Abe et al. Production of radioactive isotopes through cosmic muon spallation in KamLAND. *Phys. Rev. C*, 81:025807, 2010.

[69] K. Nakajima. High sensitivity Radon detector using a concentration method. Master's thesis, Tohoku University - Sendai, JAPAN, 2007.

[70] C. Zhang. *Precision Measurement of Neutrino Oscillation Parameters and Investigation of Nuclear Georeactor Hypothesis with KamLAND*. PhD thesis, California Institute of Technology - Pasadena, CA, 2011.

[71] Y. Konno. Development of Radon Detector for Liquid Scintillator. Master's thesis, Tohoku University - Sendai, JAPAN, 2007.

[72] H. Takahashi. Light Yield Measurement During 2^{nd} Phase Purification. KamLAND Collaboration Meeting (Internal Report), March 2009.

[73] C. Grant. Light Attenuation After 2^{nd} Phase of Purification. KamLAND Collaboration Meeting (Internal Report), March 2009.

[74] K. Nakajima. Long Term Variation of KamLAND PMT Gain. KamLAND Collaboration Meeting (Internal Report), March 2008.

[75] C. Grant. Spallation Neutron Monitoring During 2nd Phase Purification. KamLAND Collaboration Meeting (Internal Report), March 2009.

[76] S. Agostinelli et al. GEANT4 - a simulation toolkit. *Nucl. Instr. Meth. A*, 506(3):250–303, 2003.

[77] J. B. Birks. Scintillations from organic crystals: Specific fluorenscence and relative response to different radiations. *Proc. Phys. Soc.*, A64.

[78] L. Hsu. Internal KamLAND report. May 2006.

[79] J. B. Birks. *Theory and Practice of Scintillation Counting*. Permagon Press LTD., Oxford, England, 1964.

[80] F. Suekane. Collection of Radioactivity Measurements. Internal KamLAND Report, October 2000.

[81] R. McKeown B. Tipton L. Hoffman, A. Piepke and P. Vogel. Background Estimates for KamLAND from Natural Radioactivity of the Detector. Internal KamLAND Report, October 2001.

[82] Richard A. Johnson and Dean W. Wichern. *Applied Multivariate Statistical Analysis*. Pearson Education, Inc., Upper Saddle River, NJ, 2007.

[83] T. Iwamoto. *Measurement of Reactor Anti-Neutrino Disappearance in KamLAND*. PhD thesis, Tohoku University - Sendai, JAPAN, 2003.

[84] L. Winslow. *First Solar Neutrinos from KamLAND: A Measurement of the ^8B Solar Neutrino Flux*. PhD thesis, University of California, Berkeley - Berkeley, CA, 2009.

[85] A. Gando et al. Constraints on θ_{13} from a three-flavor oscillation analysis of reactor antineutrinos at KamLAND. *Nature Geoscience*, 4:647–651, 2011.

[86] LBNL Isotopes Project LUNDS Universitet. The lund/lbnl nuclear data search. `http://nucleardata.nuclear.lu.se/nucleardata/toi/`.

Appendix A

^{232}Th and ^{238}U Decay Series

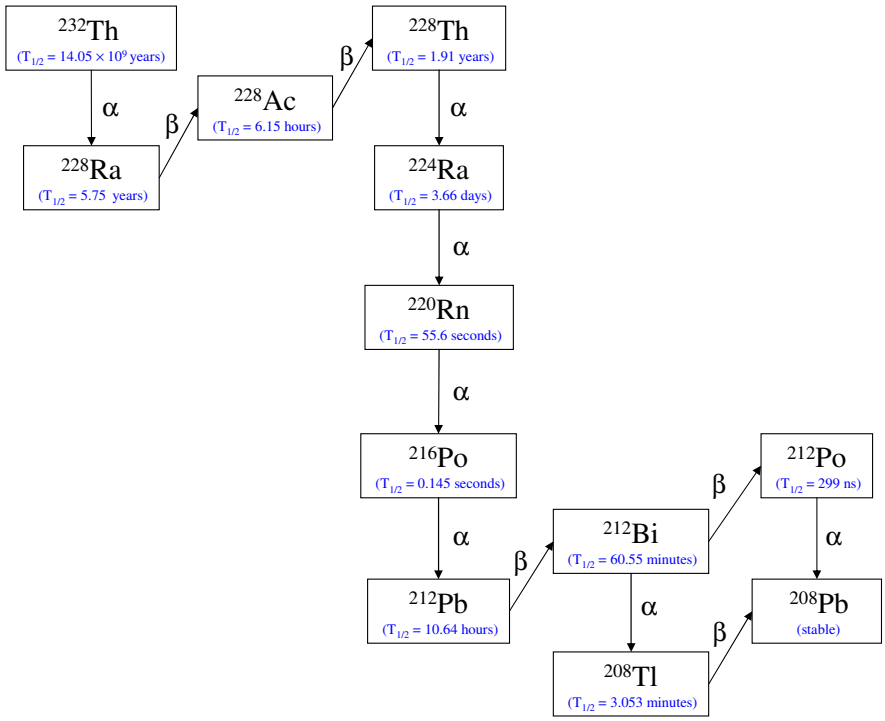

Figure A.1: A diagram of the ^{232}Th decay series. The decay information is taken from [86].

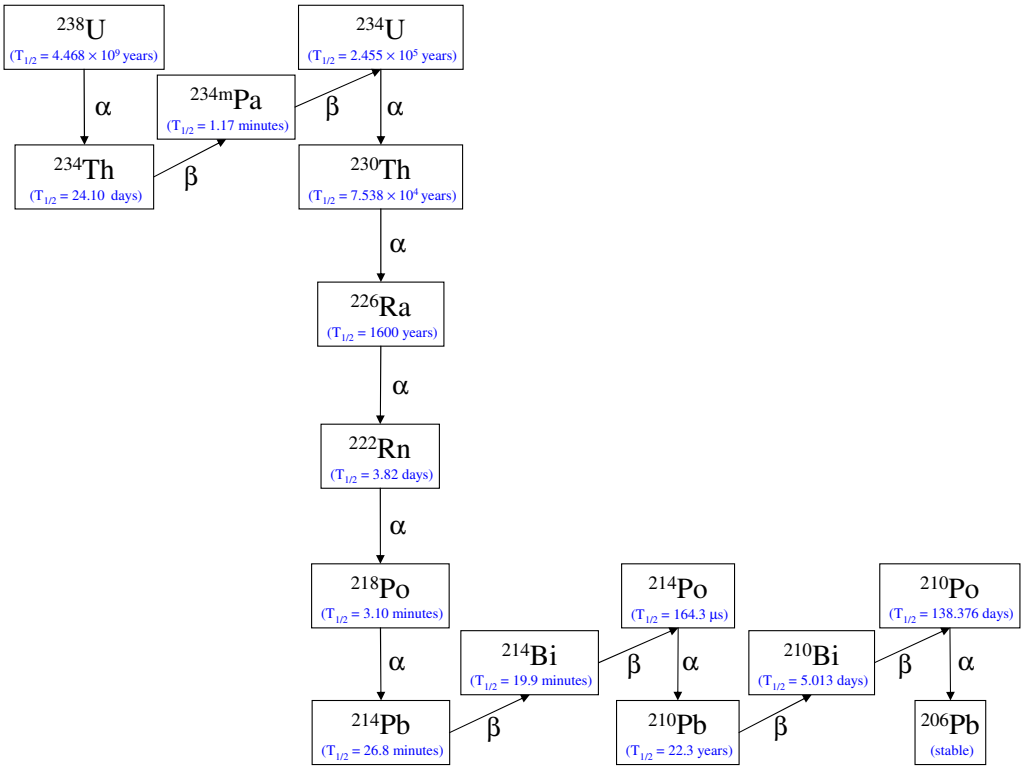

Figure A.2: A diagram of the ^{238}U decay series. The decay information is taken from [86].